September 2001 • NREL/SR-520-30922

Subcontractor Report

Optimization of Processing and Modeling Issues for Thin Film Solar Cell Devices Including Concepts for the Development of Polycrystalline Multijunctions

Annual Subcontract Report
24 August 1999–23 August 2000

R.W. Birkmire, J.E. Phillips, W.N. Shafarman, E. Eser, S.S. Hegedus, and B.E. McCandless
University of Delaware
Newark, Delaware

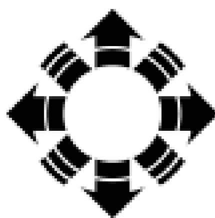

National Renewable Energy Laboratory

1617 Cole Boulevard
Golden, Colorado 80401-3393

NREL is a U.S. Department of Energy Laboratory
Operated by Midwest Research Institute • Battelle • Bechtel

Contract No. DE-AC36-99-GO10337

September 2001 • NREL/SR-520-30922

Optimization of Processing and Modeling Issues for Thin Film Solar Cell Devices Including Concepts for the Development of Polycrystalline Multijunctions

Annual Subcontract Report 24 August 1999 – 23 August 2000

R.W. Birkmire, J.E. Phillips, W.N. Shafarman, E. Eser, S.S. Hegedus, and B.E. McCandless
University of Delaware
Newark, Delaware

NREL Technical Monitor: B. von Roedern

Prepared under Subcontract No. ZAK-8-17619-33

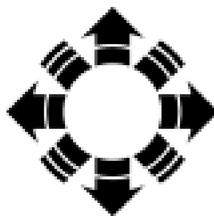

National Renewable Energy Laboratory

1617 Cole Boulevard
Golden, Colorado 80401-3393

NREL is a U.S. Department of Energy Laboratory
Operated by Midwest Research Institute • Battelle • Bechtel

Contract No. DE-AC36-99-GO10337

NOTICE

This report was prepared as an account of work sponsored by an agency of the United States government. Neither the United States government nor any agency thereof, nor any of their employees, makes any warranty, express or implied, or assumes any legal liability or responsibility for the accuracy, completeness, or usefulness of any information, apparatus, product, or process disclosed, or represents that its use would not infringe privately owned rights. Reference herein to any specific commercial product, process, or service by trade name, trademark, manufacturer, or otherwise does not necessarily constitute or imply its endorsement, recommendation, or favoring by the United States government or any agency thereof. The views and opinions of authors expressed herein do not necessarily state or reflect those of the United States government or any agency thereof.

Available electronically at http://www.osti.gov/bridge

Available for a processing fee to U.S. Department of Energy
and its contractors, in paper, from:
U.S. Department of Energy
Office of Scientific and Technical Information
P.O. Box 62
Oak Ridge, TN 37831-0062
phone: 865.576.8401
fax: 865.576.5728
email: reports@adonis.osti.gov

Available for sale to the public, in paper, from:
U.S. Department of Commerce
National Technical Information Service
5285 Port Royal Road
Springfield, VA 22161
phone: 800.553.6847
fax: 703.605.6900
email: orders@ntis.fedworld.gov
online ordering: http://www.ntis.gov/ordering.htm

Printed on paper containing at least 50% wastepaper, including 20% postconsumer waste

SUMMARY

The overall mission of the Institute of Energy Conversion (IEC) is the development of thin film photovoltaic cells, modules, and related manufacturing technology and the education of students and professionals in photovoltaic technology. The objectives of this 12 month NREL subcontract are to advance the state of the art and the acceptance of thin film PV solar cells in the areas of improved technology for thin film depositions, device fabrication, and material and device characterization and modeling, relating to solar cells based on CuInSe2 and its alloys, on doped and intrinsic microcrystalline Si films, and on CdTe.

$CuInSe_2$-BASED SOLAR CELLS

In-line Evaporation of $Cu(InGa)Se_2$

In-line evaporation is a potentially effective means to achieve the high rate uniform deposition necessary for commercial-scale manufacture of $Cu(InGa)Se_2$ modules. In this process, the substrate is linearly translated over thermal sources from which the elemental materials are evaporated.

An in-line evaporation system for the deposition of $Cu(InGa)Se_2$ films has been put into operation at IEC. The system's performance in terms of uniform deposition over large areas at relatively high rates and in terms of device performance and reproducibility has been successfully demonstrated. The compositional uniformity across the 6-inch wide deposition zone is within the uncertainty limits of EDS measurements. A set of depositions with translation speeds ranging from 1 to 2.5 inches/min produced films with thicknesses from 2.1 to 0.9 μm. Devices from these runs had efficiencies from 13.2-14.5 %, for thickness > 1 μm, demonstrating the run-to-run reproducibility of the system. The best cell produced with $Cu(InGa)Se_2$ from this in-line system had 14.9% efficiency.

Effect of Deposition Temperature on $Cu(InGa)Se_2$ Films and Devices

One means to reduce manufacturing costs for thin film $Cu(InGa)Se_2$ is by reducing the substrate temperature at which the $Cu(InGa)Se_2$ layer is deposited. The effect of substrate temperature on the film grain size, morphology, and compositional uniformity and device performance of $Cu(InGa)Se_2$ deposited at 480°C was characterized and compared to previous results at 400°C and 550°C. At 480°C, the soda lime glass substrate is below the strain point of the glass, reducing handling problems.

$Cu(InGa)Se_2$ films were deposited by multisource elemental evaporation with different deposition sequences to determine the effect of a Cu-rich growth step, i.e., deposition with the Cu molar flux greater than the sum of the In and Ga fluxes. The grain size was determined from atomic force microscopy images. The films deposited at 480°C have comparable grain size and morphology to those deposited at 550°C. However, V_{oc}, FF, and efficiency of devices with films deposited at 550°C were greater. A Cu-rich growth step during the deposition does not affect the measured grain size or device performance at these temperatures. The films deposited at 400°C

have smaller grains and poorer device performance. At this lower temperature the Cu-rich growth improves device efficiency.

Formation and Analysis of Graded $CuIn(SeS)_2$ and $CuGa(SeS)_2$ Films

The incorporation of sulfur into $CuInSe_2$ thin films was quantitatively investigated to establish a scientific and engineering basis for the fabrication of homogeneous and compositionally graded $CuIn(SeS)_2$ thin films.

$CuInSe_2$ and $CuInS_2$ form a continuous solid solution in which the optical bandgap varies from 1.0 to 1.55 eV. By reacting stoichiometric or slightly Cu-rich $CuInSe_2$ films in a flowing H_2S/Ar atmosphere, the films can be completely converted to $CuInS_2$ or converted to a graded $CuIn(Se_{1-y}S_y)_2$ film, depending on processing conditions. A phenomenological model of the reaction/diffusion process was developed wherein H_2S reacts with $CuInSe_2$ at the surface to form $CuInS_2$, releasing Se. The $CuInS_2$ and $CuInSe_2$ layers interdiffuse, resulting in a S/Se gradient in the structure. X-ray diffraction (112) line profiles of graded films are compositionally broadened due to continuously changing lattice parameters. The 3-dimensional sulfur distribution was calculated for measured grain size distribution using generated diffraction line profiles. These were fit to measured line profiles using bulk and grain boundary diffusion coefficients as fitting parameters, yielding diffusion coefficients and activation energies for bulk and grain boundary diffusion processes.

The incorporation of sulfur into $CuInSe_2$ and $CuGaSe_2$ and into Cu-rich and Cu-deficient films has also been studied. The S incorporation into films reacted in flowing H_2S/Ar was characterized by EDS and x-ray diffraction line profiles. Under fixed reaction conditions, including time, temperature, and gas concentration, less S is incorporated into $CuGaSe_2$ than $CuInSe_2$. In addition, the incorporation of S into Cu-deficient films, with Cu/In or $Cu/Ga < 1$, is less than films with Cu/In or $Cu/Ga \geq 1$. Glancing incidence x-ray diffraction measurements of Cu-deficient $CuIn(SeS)_2$ films formed by the S reaction of $CuInSe_2$ indicate that there is a $CuInS_2$ surface layer but little incorporation of the S into the bulk film.

$CuInSe_2$ Team Participation and Collaborations

IEC is an active member of the following four sub-teams under the National CIS Team for the NREL Thin Film Partnership program:

- Global Solar Energy. This team is focusing on helping GSE develop a low temperature process for the roll-to-roll deposition of $Cu(InGa)Se_2$. IEC is providing direct support through materials characterization and device fabrication and characterization.

- ISET. IEC is assisting in the development of improved performance of ISET's CIS-based materials by investigating the use of sulfur incorporation to increase the voltages in the devices and modules.

- Siemens Solar Industries. This sub-team is addressing reliability and transient effects in SSI's cells and modules. IEC is providing device fabrication and characterization for other team members and supplying $Cu(InGa)Se_2$ films and devices for characterization.

- UNISUN. IEC is providing detailed materials characterization, device fabrication and characterization to support UNISUN's development of particle-based processes for deposition of Cu(InGa)Se_2.

In addition to these activities in support of the national CIS Teams, IEC has provided direct support to several other groups within the Thin Film Partnership. Some specific activities have included:

- Florida Solar Energy Center. IEC has done detailed J-V and QE measurements and analysis of FSEC's CuIn(SeS) devices.

- University of Illinois. IEC has developed a process to fabricate solar cells on Cu(InGa)Se_2 epilayers grown on GaAs substrates at U. Illinois. This process includes a Pt back contact and takes advantage of the conductivity of the GaAs. The best cell to date on the epilayers had efficiency > 7%.

- Washington State University. IEC has continued to fabricate and characterize devices using alternate window layers being developed at WSU.

- University of Oregon. IEC has provided Cu(InGa)Se_2 device samples with different Ga content and grain size for device analysis.

Si-BASED SOLAR CELLS

Micro-crystalline p-layers

This research focused on deposition of more conductive µc-Si:O:H based p-layers using CO_2 in the discharge. We investigated the CO_2 based films because last year's effort, which focused on µc-Si:C:H layers using CH_4 in the discharge, concluded that C inhibited the crystallinity. The µc-Si:O:H p-layers were deposited by RF CVD. The effect of H_2, SiH_4, B_2H_6 and CO_2 flow rates, and RF power on microcrystallinity and conductivity was studied. This work is motivated by the need for a wide bandgap highly conductive p-layer material to simultaneously increase V_{oc} and blue response of superstrate p-i-n solar cells. The goal here was to obtain two phase films of crystalline Si imbedded in a matrix of a–Si:O:H:C. The idea is that such films incorporated in p-i-n type devices could give high currents due to the transparency of the amorphous phase and high voltages due to the highly conductive crystalline phase with a smaller junction surface. Also, the presence of CO_2 in the glow discharge plasma would tend to decrease the reducing effects of the plasma on the thin conductive oxide used as the front contact in superstrate devices.

The p-layers were deposited on 7059 glass and on SnO_2 substrates, and their crystallinity was determined by Raman spectroscopy. In-plane conductivity and activation energy measurements were also performed on most of the films deposited on glass substrates.

The main experimental variables were the hydrogen dilution and CO_2 content in the feed gases. The secondary parameters were discharge power density and doping gas (B_2H_6) level. Increasing hydrogen dilution reduces the deposition rate even though silane partial pressure and

gas residence time stay the same. This observation supports hydrogen etching of the film during growth. The observed increase in deposition rate with diborane concentration is related to the known ability of diborane in cracking silane molecules. Results also show that while the CO_2 level in the discharge does not seem to have an effect on the c-Si content in the case of glass substrates, it does, however, control crystallinity of the films deposited on SnO_2 substrates.

The only crystalline phase identified was silicon. Volume fraction of the crystalline phase was found to depend on hydrogen dilution but not on the discharge power. High silane partial pressures resulting in high deposition rates suppress the formation of the crystalline phase. High levels of crystallinity were obtained at very low power densities. Crystallinity in the films was found to decrease with increasing amounts of CO_2 in the discharge. The amount of crystalline phase in the films deposited on SnO_2 was consistently lower than in the films deposited on glass substrates. Raman spectra showed the existence of a two-phase mixture consisting of c-Si and amorphous silicon phases. Also, the film deposited on glass seems to have a higher amount of c-Si phase.

SIMS depth profiles indicate that the composition of the films are independent of the substrate, and the oxygen and carbon content in the films are, respectively, 10^{22} and $7x10^{20}$. Since the films have a c-Si and an amorphous phase, the latter must contain almost all the hydrogen, carbon and oxygen observed in the SIMS analysis. Thus it can be concluded that the amorphous phase is essentially hydrogenated silicon oxide containing small amounts of carbon and boron.

It is found that the fraction of c-Si increases with increasing hydrogen dilution and decreases with increasing diborane level. However, this observation is complicated by the dependence on the film deposition rates. This is because bonding rearrangement on the surface of the growing film that favors c-Si formation will be more extensive for low deposition rates. Consequently, dependence of crystallinity on hydrogen dilution is only clear in the regions where deposition rates do not change appreciably. The deposition rate argument can also explain the difference in crystallinity between like substrates deposited at different diborane levels.

However, the difference in crystallinity between glass and tin oxide substrates for a given diborane level might also be controlled, in addition to deposition rate, by the possible difference in the initial nucleation rate of crystallites on glass and tin oxide surfaces. The difference in deposition rates between glass and SnO_2 substrates is most probably due to the voltage difference between substrate and the plasma. In the case of a conductive substrate, such as SnO_2, the surface is grounded and the potential difference between substrate and plasma is the plasma potential. In the case of glass substrate, the potential difference is the floating potential which, in general, is substantially smaller than the plasma potential.

Increasing hydrogen dilution reduces the deposition rate even though silane partial pressure and gas residence time stay the same. This observation supports hydrogen etching of the film during growth. Finally, the observed increase in deposition rate with gas phase diborane concentration is related to the known ability of diborane in cracking silane molecules.

Interpretation of the measured conductivities and activation energies is problematic because of the two-phase nature of these films. However, it can be pointed out that measured activation

energies of 0.07 eV are, within experimental errors, that of boron in silicon and, as such, confirm that in this respect silicon crystallites in the films behave like bulk silicon.

In order to characterize the structure of the films at thicknesses comparable to p-layer thicknesses in operational devices, we deposited 150 Å thick films and determined their crystallinity. Deposition times for these films were estimated from the deposition rates measured on thicker films on SnO_2 substrates prepared under identical conditions. Raman analysis of the films showed that on SnO_2 coated substrates the films had all amorphous character. On glass substrates, however, substantial crystalline fractions were observed. Considering the fact that deposition rates on glass substrates are generally lower than on SnO_2, the data indicate that on glass substrates c-Si phase forms at film thicknesses considerably less than 150Å. It can then be concluded that lack of crystallinity on SnO_2 coated substrates is not simply due to the small film thickness.

To substantiate this observation we deposited the same films on the same substrates but coated in-situ with a very thin (≈10 Å) SiO_x layer. Raman spectroscopic analysis of the films indicates the presence c-Si phase in all cases but with a smaller c-Si peak width than for the films deposited on glass without SiO_x. This could possibly indicate that SiO_x film thickness was thick enough to provide a base for c-Si nucleation but not thick enough to suppress totally the effect of the underlying substrate.

Microcrystalline n-layers

A limited investigation of the microcrystalline n-layers deposited from SiH_4, H_2, and CO_2 found that they contained P doped c-Si imbedded in a matrix of a-SiO_x:H:C. The c-Si volume fractions and conductivities are higher than what is observed in the B doped microcrystalline p-layers.

Characterization of the SnO_2/p and ZnO/p Contact Resistance and Junction Properties in p-i-n Solar Cells

Transparent conductive oxides (TCO) are essential to the optical and electrical performance of a-Si based solar cells. For superstrate a-Si TCO/p-i-n solar cells, minimizing the resistance between the p-layer and TCO is a critical issue for the incorporation of new TCO materials like ZnO or alloys of Zn-In-O and Zn-Sn-O and new p-layers like μc-SiC or μc-SiO into devices. However, characterization of the TCO/p interface is difficult since it is in series with the dominant p-i-n junction. We have developed a method to characterize the TCO/p contact in a functioning TCO/p-i-n device using dark JV measurements from a row of devices on a single isolated TCO strip. It is useful for understanding resistance losses in modules and for diagnosing how plasma processing affects the TCO and junction properties, since the TCO/p contact and TCO sheet resistances in a completed device structure are obtained.

The method is applied to a series of devices fabricated at BP Solar on commercial SnO_2 and ZnO-coated SnO_2 having different p-layer recipes and pre-deposition treatments. Values of the contact resistance (R_C) of 1±0.5 Ω-cm^2 were found for a wide range of TCO and p-layer processing including ZnO. The temperature dependence of R_C gave a barrier height of 40-55 meV. Analysis of devices with a thin ZnO layer on SnO_2 and with different predeposition treatments indicates lower V_{oc} and FF observed with ZnO is not due to the contact but to changes

in the p/i junction recombination. The solar cell performance is very sensitive to the ZnO surface treatment but R_C is not. No evidence was found for a blocking or high resistance ZnO/p contact. These results contradict the commonly accepted but unproven assumption that ZnO forms a blocking or high resistance contact with the a-SiC p-layer. Instead, we show that the ZnO layer is detrimental to the diode properties such as A and JO.

Hot-wire Deposited Si Films

A series of experiments were carried out to study the deposition of boron-doped polycrystalline Si films by HWCVD on glass. The resulting films exhibited a resistivity of 1-100 Ω-cm, as determined by 4-point probe measurements. The grain size in the films, however, was 10-50 nm. Because of the large number of grain boundaries accompanying such small grains, it is questionable whether these films are suitable for device development. Consequently, it became necessary to develop approaches to enhance the film grain size by either in-situ deposition techniques or post-deposition treatments. One approach being considered is Metal Induced Crystallization (MIC) with the aid of aluminum, nickel or tin layers. To this end, collaborations have been established with Bhushan Sopori at NREL and Ajeet Rohatgi at the Georgia Institute of Technology. A series of amorphous and polycrystalline, doped and un-doped Si films have been deposited on aluminum coated glass and provided to both collaborators for MIC post-treatment.

The compatibility of polycrystalline Si films with 7059 glass is also under study. For films with thickness > 5 µm, a large number of cracks and delamination is observed. This is the result of significant internal stress, which potentially arises from the difference in thermal expansion between the films and the glass. To solve this problem, two approaches are under consideration. In one, glass (Corning 1737) with thermal expansion properties closer to those of Si will be used. In the other, the surface of the glass will be roughened, thereby reducing the stress by segmenting the film.

Maintenance of the HWCVD reactor absorbed a great portion of this year's activities. Recurring problems with leaks resulting from thermal cycling have been addressed. Components, damaged by undesired silicon deposition, also required replacement. Finally, Tri-methyl-Boron was added to the system as a dopant. It is expected that this source will provide improved controllability of the dopant incorporation in the films.

a-Si Team Participation

IEC is a member of the National a-Si Team under the Thin Film Partnership Program. Steve Hegedus had been the leader of the Multijunction Device sub-team for 8 years and stepped aside this year. The work on characterization of the TCO/p contact resistance was performed as part of the Teaming activities in collaboration with BP Solarex. During this contract period, IEC collaborated with: Gautam Ganguly at Solarex by characterizing the TCO/p contact resistance on their sub-modules having different textured SnO_2; Bhushan Sopori at NREL by fabricating back reflector structures on textured TCO/a-Si substrates for analysis by PVOPTICS; and Eric Schiff at Syracuse University by providing him with special TCO/i-n device structures for electroabsorption measurements. These teaming collaborations lead to co-authoring one

publication at the Spring 2000 Materials Research Society Conference and two at the 28th IEEE Photovoltaic Specialists Conference.

CdTe/CdS-BASED SOLAR CELLS

Quantitative Analysis of CdS/CdTe Interdiffusion: Bulk and Grain Boundary Regions

Thin-film solar cells based on polycrystalline CdTe have demonstrated ~16% solar conversion efficiency using CdS films as the heterojunction partner and window layer. Cell performance is directly coupled to the CdS layer thickness since parasitic optical absorption in the CdS layer limits photoresponse at short wavelengths, necessitating CdS film thickness less than 80 nm in the device for optimal current generation. Further, discontinuities in the CdS layer result in parallel junctions between the CdTe and the transparent conductive oxide, which typically have higher reverse saturation current than CdS/CdTe, limiting the open circuit voltage. Maintaining CdS film continuity at thicknesses below 80 nm after device processing is complicated by diffusion of CdS into CdTe, which occurs during processing in the presence of $CdCl_2$ and O_2. The principal factors affecting CdS diffusion have been empirically identified as CdTe film grain size, CdS film preparation, CdS/CdTe treatment temperature, and CdS/CdTe ambient species concentration. However, a quantitative treatment of the resulting $CdTe_{1-x}S_x$ alloy distribution and the diffusion process in the thin-film couple, including the effect of grain size, has not been previously shown.

A method was developed for investigating the diffusion process of CdS into CdTe using measured x-ray diffraction line profiles, grain size distributions and grain boundary widths in CdTe/CdS couples. The approach consists of determining sulfur distribution within geometrically simplified grains, partitioning the grains into discrete volume elements, and combining their volume fractional contributions to the diffracted beam intensity. The diffusion process was modeled for simultaneous diffusion from the source into the grain and grain boundary regions as well from grain boundary into the grain. The two dimensional solution for parallel grain boundaries in a sample of finite thickness was adopted. Solutions were obtained for measured grain size distributions and initial estimates of bulk and grain boundary diffusion coefficients and were transformed into three dimensions by using a cylindrical coordinate system.

Only diffusion of CdS into CdTe, resulting in formation of a $CdTe_{1-x}S_x$ alloy, was considered. The solubility limit of this alloy at each temperature was established from measured data for CdTe/CdS heat treated with $CdCl_2$:O_2:Ar vapor and was compiled into a provisional phase diagram. $CdTe_{1-x}S_x$ alloy volume fractions, expressed as the molar composition, x, were calculated for incremental values of x within annular slabs of the model volume, or grain. The volume fractions at each discrete composition were summed and then transformed into an x-ray diffraction intensity line profile with half-width at half-maximum and shape parameter values determined from annealed CdTe powder samples. The resulting profile was corrected for primary and diffracted beam extinction in overlying slabs.

Modeled line profiles were refined by comparison with measured profiles, using only the bulk and grain boundary diffusion coefficients as fitting parameters. Measured profiles were obtained from CdS/CdTe/CuTe/Mo/glass structures, in which the grain size distribution remained constant

over the entire treatment temperature and time range explored. Verification of the bulk coefficient was obtained by Auger depth profile analysis of treated CdS/CdTe couples using single crystal CdTe substrates. The S diffusion coefficients were determined for single crystal CdTe (bulk), substrate configuration thin-films (bulk and boundary) and superstrate configuration thin-films (bulk and boundary). The effect of $CdCl_2$ and O_2 species concentration on bulk and boundary coefficients was also determined and was found to principally affect the boundary coefficient (by up to 5 orders of magnitude for a 5X increase). Pre-oxidation of CdTe/CdS films at 450ºC provides a means for limiting grain boundary diffusion during subsequent $CdCl_2$+O_2 treatments by formation of native oxides. Time-progressive diffusion of CdS into CdTe resulting from thermal treatment at 440ºC in vapor ambient consisting of 10 mTorr $CdCl_2$ and 130 Torr O_2 was modeled by bulk and grain boundary diffusion processes with coefficients 1.25 x 10^{-13} cm^2/sec and 1.5 x 10^{-8} cm^2/sec, respectively. Modeling diffraction line profiles of samples treated at other temperatures yielded activation energies for the bulk and grain boundary diffusion processes of 2.8 eV and 2.0 eV, respectively. The bulk diffusion coefficients obtained from thin-film structures were found to be comparable to those obtained by Auger depth profiling of sulfur composition in CdS/CdTe couples using CdTe single crystals.

CdS/TCO Window Layer Optimization with Thin CdS

For CdTe/CdS/ITO (or SnO_2)/glass devices, optical absorption in the CdS layer is the predominant photocurrent loss, making it necessary to minimize the CdS film thickness in the device. Maintaining junction quality in superstrate structures with d_{CdS} < 100 nm depends on maintaining a uniform interface throughout the processing to avoid formation of parallel junctions between CdTe and the TCO. X-ray diffraction and opto-electronic measurements of the interfacial region in high efficiency cells shows that the interface actually consists of $CdTe_{1-x}S_x$/$CdS_{1-y}Te_y$, where the interfacial values of x and y correspond to the solubility limits in the CdTe-CdS system at the device processing temperature. The $CdTe_{1-x}S_x$ and $CdS_{1-y}Te_y$ alloys affect photocurrent and junction behavior. Formation of the $CdS_{1-y}Te_y$ alloy on the S-rich side of the junction reduces the bandgap and increases absorption, reducing photocurrent in the 500 to 600 nm range. Formation of the $CdTe_{1-x}S_x$ alloy on the Te-rich side of the junction reduces the absorber layer bandgap, due to the optical bowing parameter of the CdTe-CdS alloy system, which can result in lower V_{oc}.

Another significant effect of this alloy formation is spatially non-uniform consumption of the CdS layer, leading to parallel junctions between $CdTe_{1-x}S_x$/ $CdS_{1-y}Te_y$ and $CdTe_{1-x}S_x$/ ITO (or SnO_2). These parallel junctions result in a net increase in J_o, which reduces V_{oc}. Penetration of S-rich species into the CdTe grain boundaries can produce a three-dimensional junction, which increases the actual junction area, also reducing V_{oc}. Processing techniques which control grain boundary properties should aid controlling film properties over the large areas required for module manufacturing.

Processing strategies have been developed for controlling junction quality as both window and absorber layer thickness is reduced in polycrystalline superstrate CdS/CdTe thin-film solar cells. High resistance In_2O_3 and SnO_2 oxide buffer layers improve coverage of chemical bath deposited CdS and device performance with PVD CdTe, resulting in efficiencies >13.5%. A new method of CdS and $Cd_{1-x}Zn_xS$ chemical bath deposition for high Cd utilization and growth rate and low occurrence of adherent particulates is presented. Alloying the CdS film with ZnS can reduce the

window thickness tolerance needed to obtain high photocurrent and good junction properties with no oxide buffer layer. CdS diffusion is reduced by annealing in air at 450°C or in argon at 580°C prior to $CdCl_2$ treatment and by reducing the $CdCl_2$ and O_2 partial pressures during treatment. Promising device results are presented for CdTe/CdS cells with 1 micron thick CdTe deposited at T < 400°C.

Analysis of CdS/CdTe Device Stability During Accelerated Stressing

CdTe/CdS modules in field testing are reported to be stable. However, no clear correlation has been found between processing parameters and either these stable existence-proof cases or those that changed in field testing. Recent work to accelerate these processes at the laboratory scale (stress testing) have shown that typically the V_{oc} and FF degrades, particularly for devices held at moderate forward or reverse bias. The back contact process is strongly implicated in the stress-induced degradation, especially with respect to the presence of Cu and its compounds, which are sensitive to small, localized fields in both electrochemical and electromigration processes.

A difficulty in evaluating changes in device behavior is sample-to-sample variability in both CdS/CdTe films and post-deposition treatment and contacting processes. Another variable in previously published stress studies is the atmosphere during stress. To minimize these variations, CdS/CdTe films from a single source were employed to fabricate devices. Three different back contact processes were studied: a wet process, including a penetrating etch leaving a ~30 nm Te layer followed by Cu/C contact; a dry process, leaving a ~10 nm Te layer followed by Cu/C contact; and the dry contact process without Cu. They were stressed at different electrical bias points in controlled atmospheres of dry air, H_2/Ar, or Ar. The JV behavior of these stress-degraded devices was analyzed. After stress, some devices had the C contact removed and were recontacting with a new C layer. Significant changes were observed.

Accelerated stressing of CdS/CdTe solar cells at elevated temperatures (60-100°C) under a range of applied bias in light and dark has identified three degradation modes. One, which occurs at forward bias, is Cu-related, field-driven, occurs in ~hours, greatly increases the recombination and is partially reversible with field. A second mechanism leads to formation of a blocking contact, which also occurs rapidly and is likely related to loss of Cu, but is not reversible with field. It is eliminated by replacing the C contact without additional Cu. The third mechanism, which occurs under reverse bias, is much slower, may not be Cu related, and changes the photoconductivity of either the CdS or CdTe. Devices with Cu-contacts degrade with a strong bias dependence. Thus, the commonly observed blocking contact is formed under forward bias. Junction degradation requires both higher temperature and forward bias. Recontacting the device after stress removes the blocking contact with no change in junction losses. Devices without Cu in the contact have much poorer initial performance but degrade nearly independent of bias.

We have shown that there are at least three degradation mechanisms operative in CdS/CdTe devices under thermal and bias stress. We propose that Cu^{++} is liberated from the Cu_2Te layer and moves along grain boundaries under forward bias. Diffusion lengths for Cu in bulk CdTe and along grain boundaries have been calculated for 1 hour at 100°C. Cu would move 0.3 µm in the bulk and 30 µm along grain boundaries. Clearly, grain boundaries are important channels for Cu motion. It is possible to relate Cu diffusion to all three degradation modes: formation of a blocking contact, increased junction recombination, and increased dark resistivity.

Team Participation

IEC has had extensive collaborations supporting the two industrial members of the Thin Film Partnership CdTe Team. We have provided BP Solar with structural and compositional analysis of their CdS/CdTe films and assisted in optimizing their post-deposition processing. Relating the grain size and chemical state of bulk and grain boundary regions to processing steps identified a path to achieve higher V_{oc}. An optical loss analysis suggested specific directions to increase J_{sc}. The guidance provided by IEC was crucial to increasing their baseline efficiency from 8 to 10%. Brian McCandless spent several days at the Fairfield plant to review their process, examine their data and present new ideas.

Our interactions with First Solar were focused on stress-related studies. They supplied us with a variety of CdS/CdTe without back contacts cut from large area modules. This was our source of material for all the stress studies reported here and at Team meetings. We use their baseline material to optimize our contacts for initial and stressed performance, and to investigate stress-related mechanisms.

IEC also interacted with Jim Sites and Jason Hiltner at Colorado State University on the subject of localized photocurrent variations in CdTe/Cds devices. IEC fabricated a special set of devices with mechanically scribed fiduciary lines in the TCO for samples with varying CdS thickness. Using their high-resolution laser scanning capability, two types of micron size regions having low output were discovered, exhibiting proportional or amplified decreasing photocurrent with decreasing illumination. No correlation has been made between the regions and physical properties.

LIST OF CONTRIBUTORS

PRINCIPAL INVESTIGATORS

Robert W. Birkmire
Erten Eser
Steven S. Hegedus
Brian E. McCandless
James E. Phillips
T.W. Fraser Russell
William N. Shafarman

RESEARCHERS

Wayne A. Buchanan
Marylin Huff

VISITING PROFESSIONALS

Ruhi Kaplan, Fulbright Scholar, University of Erciyes, Turkey
Nto Diarra, University of Lowell, Massachusetts

POST-DOCTORAL FELLOWS

Roger Aparicio
Gregory Hanket
Devassy Paulson
Udai Singh
Jie Zhu

TECHNICAL SUPPORT

Charles Debo
Ronald Dozier
Shannon Fields
Kevin Hart
Tom Hughes-Lampros

GRADUATE STUDENTS

Ozgenc Ebil
Moses Haimbodi
Toby Junker
Atul Pant
Jochen Titus

Dan Zak

STUDENTS

Jason Baxter
Sunil Earath
Tom Gillis
Timothy Miller
Alpa Modi
Chintan Mody
John Ritter
Daniel Ryan
Alexis Siery

DOCUMENT PREPARATION

Steven S. Hegedus
Linda Granger

TABLE OF CONTENTS

SUMMARY ii
LIST OF CONTRIBUTORS xii
TABLE OF CONTENTS xiv
LIST OF FIGURES xvi
LIST OF TABLES xx

1 INTRODUCTION 1

1.1 $CuInSe_2$-based Solar Cells 1

1.2 Si-based Solar Cells 1

1.3 CdTe/CdSe-based Solar Cells 2

1.4 Training and Education 3

1.5 Publications 3

1.6 Organization of the Report 3

2 $CuInSe_2$-BASED SOLAR CELLS 4

2.1 In-line Evaporation of $Cu(InGa)Se_2$ 4
2.1.1 In-line Evaporation System Description 4
2.1.2 In-line System Performance 6
2.1.3 Characterization of Compositional Profiles 7

2.2 Effect of Deposition Temperature on $Cu(InGa)Se_2$ Films and Devices 10

2.3 Formation and Analysis of Graded $CuIn(SeS)_2$ and $CuGa(SeS)_2$ Films 14
2.3.1 Sulfur Reaction Experimental Procedures 15
2.3.2 Equilibrium Thermochemistry and Diffusion Model 16
2.3.3 Sulfur Reaction Results 17
2.3.4 Sulfur Reaction Versus Film Composition 18

3 SI-BASED SOLAR CELLS 23

3.1 Microcrystalline Silicon Oxide p-layers 23
3.1.1 Introduction 23
3.1.2 Experimental Approach 23
3.1.3 Conclusion 28

3.2 Microcrystalline n-layers **29**

3.3 Characterization of the SnO_2/p and ZnO/p Contact Resistance and Junction Properties in a-Si p-i-n Solar Cells and Modules **30**

3.4 Thin Si Films by HWCVD **31**

4 CDTE-BASED SOLAR CELLS **33**

4.1 Window Layer Development **33**
4.1.1 Quantitative Model of CdTe/CdS Interdiffusion 33
4.1.2 Processing Sequences to Control CdS Consumption 56
4.1.3 CdS, CdZnS, and High Resistance Transparent Buffer Layers 59

4.2 Contact Processing and Stress-Induced Degradation in CdS/CdTe Solar Cells ... **62**
4.2.1 Effect of Stressing on Junction and Contact 62
4.2.2 Mechanisms for Degradation 70
4.2.3 Phenomenological Model and Conclusions 71

5 ABSTRACT **72**

6 REFERENCES **73**

LIST OF FIGURES

Figure 1. Process schematic for CIGS in-line deposition. 4

Figure 2. IEC $Cu(InGa)Se_2$ in-line evaporation system. 5

Figure 3. Compositional uniformity across the deposition zone. 6

Figure 4. Composition reproducibility at the center of the substrate over 6 runs with different substrate transport speed. 7

Figure 5. Variables used in effusion analysis. 8

Figure 6. Cu thickness profile across the deposition zone. 8

Figure 7. Cu thickness profile along the deposition zone length. 9

Figure 8. Predicted elemental flux profiles along deposition zone centerline in machine direction. 9

Figure 9. Predicted Cu/(Ga+In) development as the substrate moves through the deposition zone. 10

Figure 10. AES depth profile of $Cu(InGa)Se_2$ film deposited at 525ºC and 1"/min. 10

Figure 11. Schematic representation of three temporal flux profiles for $Cu(InGa)Se_2$ evaporation, as described in the text. 11

Figure 12. Grain size distributions for three growth sequences at T_{ss} = 480ºC with log-normal fit to each distribution. 12

Figure 13. Compositional ratios Cu/(In+Ga) and Ga/(In+Ga) determined from AES depth profiles for films deposited at T_{ss} = 480ºC with (a) uniform fluxes, (b) Cu-rich flux in the beginning of the deposition, and (c) Cu-rich flux in the middle of the deposition. 13

Figure 14. Atomic force micrograph of etched $CuInSe_2$ film. 16

Figure 15. Grain size distribution of etched $CuInSe_2$ film. 16

Figure 16. Measured and modeled time progressive x-ray diffraction (112) line profiles for $CuInSe_2$ films reacted in H_2S at 500ºC. 18

Figure 17. XRD profiles of the <112> peak of $CuInSe_2$ films reacted in H_2S. Measurements were done using Cr $K\alpha$ radiation. 20

Figure 18. XRD profiles of the <112> peak of $CuGaSe_2$ films reacted in H_2S. Measurements were done using Cr Kα radiation. 20

Figure 19. XRD profiles of the <112> peak of $CuInSe_2$ films, from Figure 17, with an expanded y-axis. 21

Figure 20. GIXRD scans of the <204>/<220> peak doublet for the Cu poor sample in Figure 17 and Figure 19. Measurements were done using Cu Kα radiation. 21

Figure 21. SEM (10,000 X) cross-section of a sulfurized Cu-poor sample showing a discrete surface layer. The line marker is 10μm. 22

Figure 22. Raman spectra of the films from run #4847. 24

Figure 23. SIMS depth profiles of the films from run 4847. Thinner lines are the film on glass while thicker lines are the film on SnO_2. 25

Figure 24. Volume fraction of c-Si as a function of hydrogen dilution for different levels of CO_2 in the discharge. 27

Figure 25. Raman spectra of ultra-thin films (≈ 150Å) deposited on an interlayer of ≈ 10Å SiO_x. 28

Figure 26. Raman spectra of microcrystalline n-layers deposited from CO_2 containing discharge. 29

Figure 27. SEM of as-deposited evaporated CdTe film surface. 34

Figure 28. Hexagonal representation of grains and cylindrical geometry used to model diffusion. 34

Figure 29. 2-D section through cylinder showing grain structure modeled by Gilmer and Farrell. 35

Figure 30. XRD patterns for $CdTe_{0.6}S_{0.4}$ as deposited (lower) and after treatment at 415ºC in $CdCl_2$:Ar:O_2 for 60 minutes. ITO substrate is indicated by "I". Zincblende and wurtzite phases and corresponding (hkl) are indicated by "Z" and "W", respectively. 41

Figure 31. Lattice parameter versus NRST function value for zincblende and wurtzite phases of film shown in Figure 27 for $CdTe_{0.6}S_{0.4}$ after treatment. Horizontal lines indicate the lattice parameter values for pure CdTe and CdS. 42

Figure 32. CdTe-CdS pseudobinary phase diagram with data of present work and others. Values at ~420ºC were established by Jensen, et al [46]. 43

Figure 33. Excess free energies of mixing for CdS/CdTe system. 45

Figure 34. Solubility of CdS in CdTe-rich phase. Solid line is the thermodynamic model prediction. 46

Figure 35. Solubility of CdTe in CdS-rich phase. Solid line is the thermodynamic model prediction. The values correspond to y = 1-x in Figure 32. 47

Figure 36. Grain size distribution to model diffusion of CdS into CdTe thin films. 49

Figure 37. Measured x-ray diffraction (511)/(333) line profiles for as-deposited and time-progressively heat treated substrate configuration CdTe/CdS thin film couples. Heat treatment was carried out in $CdCl_2$:O_2:Ar vapor at 440ºC for the times shown. 49

Figure 38. Modeled x-ray diffraction (511)/(333) line profiles for as-deposited and time-progressively heat treated substrate configuration CdTe/CdS thin film couples using the bulk (D) and grain boundary (D_b) diffusion coefficients and times shown. 50

Figure 39. Measured x-ray diffraction (511)/(333) line profiles for as-deposited and time-progressively heat treated substrate configuration CdTe/CdS thin film couples. Heat treatment was carried out in $CdCl_2$:O_2:Ar vapor at 420ºC for the times shown. 50

Figure 40. Modeled x-ray diffraction (511)/(333) line profiles for as-deposited and time-progressively heat treated substrate configuration CdTe/CdS thin film couples using the bulk (D) and grain boundary (D_b) diffusion coefficients and times shown. 51

Figure 41. Bulk diffusion coefficients for single crystal CdTe, substrate, and superstrate film configurations. 52

Figure 42. Grain boundary diffusion coefficients for substrate and superstrate film configurations. 53

Figure 43. 2-dimensional isocompositional contour plot of sulfur distribution after diffusion for 40 minutes with $D = 1.25 \times 10^{-13}$ cm^2/sec and $D_b = 1.5 \times 10^{-8}$ cm^2/sec for grains of a 4.5 µm thick film with grain radii of 0.25 µm and 0.5 µm. Isocontours are incremented by x in $CdTe_{1-x}S_x$ in steps of 0.01. 53

Figure 44. X-ray diffraction (511)/(333) line profiles for samples treated in varying $p(CdCl_2)$ at 430ºC for 20 minutes and fixed $p(O_2)$ = 150 Torr. The profiles are shown normalized to the same area. 54

Figure 45. Bulk and grain boundary diffusion coefficient versus $p(CdCl_2)$ for treatment at 430ºC in $CdCl_2$/O_2/Ar at $p(O_2)$ = 150 Torr. 55

Figure 46. Bulk and grain boundary diffusion coefficient versus $p(O_2)$ for treatment at 430ºC in $ClCl_2$/O_2/Ar at $p(CdCl_2)$ = 9 mTorr. 55

Figure 47. X-ray diffraction line profiles of $CdTe_{1-x}S_x$ (611/333) of CdTe/CdS films treated at 420ºC in$CdCl_2$:O_2:Ar vapor with and without argon pre-anneal (pre-HT) step. 59

Figure 48. X-ray diffraction line profiles of $CdTe_{1-x}S_x$ (511/333) of CdTe/CdS films treated at 420ºC in $CdCl_2$:O_2:Ar vapor with and without air pre-anneal (Pre-HT) step. 59

Figure 49. Tapping atomic force microscope images of CBD (top) and PCBD (lower, left and right) CdS films. The CBD and left PCBD films are on specular ITO/7059 glass. The right PCBD film is on In_2O_3/ITO/7059. 62

Figure 50. Light and dark JV curves for CdS/CdTe solar cell: initial; 6 week stress at 100ºC at OC; and following re-contacting. 64

Figure 51. Relative change in efficiency for devices with different contacts after stressing at bias shown in light for 10 days at 100ºC. 65

Figure 52. Light and dark JV curves after SC and OC stress for 10 days at 100ºC. Dark curve for SC stress is nearly horizontal. 65

Figure 53. FF and V_{oc} for devices with 0 or 6 nm Cu for stress under FB in the dark at 60ºC for 10 days. 66

Figure 54. Analysis of dark JV curve as dV/dJ for device stressed at +2V bias at different times and temperatures including after recontacting. The slope is AkT/q and the intercept is R_s, and curvature at large J indicates a blocking contact. (a) has A = 1.6, R_s = 4Ω-cm^2; (b) A = 2.2, R_s = 9Ω-cm^2. 67

Figure 55. Analysis of dark JV curve as dV/dJ for device stressed at 0V bias at different times and temperatures, including after recontacting. All curves are consistent with A = 1.6, R_s = 4Ω-cm^2. 67

Figure 56 (a) and (b). Spectral response for devices stressed at SC and OC, respectively, at 0V bias with different bias filters; unfiltered = ELH bias light; blue = ELH <600 nm; red = ELH >700 nm; neutral = ELH with 30% ND filter (~same intensity as other 2 filters). 68

Figure 57 (a) and (b). Degradation and recovery of V_{oc} at 100ºC in air or H_2/Ar on linear (8(a)) and log scale (8(b)). In each atmosphere, one cell was at SC for 580 hours, then switched to OC. The other was at OC for 20 hours, then switched to SC. Open symbols for stress in air, solid symbols for H_2/Ar. 70

LIST OF TABLES

Table 1. Device performance with increasing translation speed. 7

Table 2. Mean grain area with different substrate temperature. 12

Table 3. Device results with different substrate temperature and evaporation process. 14

Table 4. Diffusion coefficients and surface source compositions. 18

Table 5. Positions for the <112> peaks under Cu and Cr radiation. 19

Table 6. Deposition conditions and measured characteristics of films deposited at two different diborane concentrations in the plasma for a range of hydrogen dilutions. 26

Table 7. Characteristics of the microcrystalline n-layer films deposited at various CO_2 levels in the discharge for three different power densities P_w. 30

Table 8. Summary of final compositions for three treatment temperatures, and approximate time needed to reach equilibrium for fixed $CdCl_2$ andO_2 concentrations. Values of x and y correspond to $CdTe_{1-x}S_x$ and $CdS_{1-y}Te_y$, respectively. 42

Table 9. CdS/CdTe solubility limits and calculated departure from ideal behavior. 45

Table 10. Bulk and grain boundary diffusion coefficients used to model the measured x-ray diffraction line profiles of substrate configuration films at different treatment temperatures. 51

Table 11. Bulk diffusion coefficient obtained from Auger depth profiles of sulfur distribution in CdTe single crystals after treatment. 52

Table 12. Photocurrent estimates for different window layer thickness with 7059/ITO absorption and 10% panchromatic reflection loss. 60

Table 13. Dark and light (~80 mW/cm^2 ELH) conductivity of 40 nm thick CdS and $Cd_{0.95}Zn_{0.05}S$ films deposited by PCBD before and after treatment in $CdCl_2$:O_2 vapor at 400ºC for 10 minutes. 61

Table 14. AM1.5 J-V results (28ºC) for devices with 7059/ITO, 7059/ITO/50nm $Cd_{0.95}Zn_{0.05}S$, 7059/ITO/In_2O_3/CdS, and 7059/SnO_2/SnO_2/CdS window layers and evaporated CdTe. All processed with 580ºC, 5 min pre-anneal and 420ºC, 15 min $CdCl_2$:Ar:O_2 treatment. 61

1 INTRODUCTION

1.1 $CuInSe_2$-based Solar Cells

Most efforts to manufacture $Cu(InGa)Se_2$ or related thin films for commercial modules utilize formation of the $Cu(InGa)Se_2$ films by either multisource evaporation or selenization of metal precursor films in either Se or H_2Se. For either process to become a commercially viable technology, manufacturing costs must be reduced. In-line evaporation is a promising approach to reduce manufacturing costs by enabling uniform deposition over a large area with high substrate throughput and good composition control. The in-line process involves the linear translation of a heated substrate over an array of sequential evaporation sources, which are designed to give uniform deposition perpendicular to the direction of translation. However, the design and control of this process and its effect on the resulting thin films are not well documented.

Another means to reduce processing costs is by reducing the substrate temperature at which the $Cu(InGa)Se_2$ layer is deposited to make substrate handling simpler and reduce thermal stress on the entire deposition system. Soda lime glass is typically used as the substrate for high efficiency $Cu(InGa)Se_2$ solar cells, but it deforms at the temperatures used for the highest efficiency devices, 550 – 600°C. It is not well understood why the high processing temperatures are needed to process these cells. With temperature reduced to ~400°C alternative substrate materials, like a flexible polymer, could be utilized. These materials could then be incorporated into an in-line process using a roll-to-roll configuration.

$CuInSe_2$ has a bandgap of 1.0 eV and the devices typically have V_{oc} less than 0.5V. The highest efficiency cells have bandgaps of about 1.2 eV through the addition of gallium to form $Cu(InGa)Se_2$. It is desirable to further increase the bandgap to reduce module-related losses. The addition of sulfur has also been used to increase the bandgap. In addition, sulfur could be used to form a $CuIn(SeS)_2$ layer with a graded bandgap near the device interface to increase V_{oc}. A fundamental scientific and engineering basis of sulfur incorporation into $CuInSe_2$ is needed for the fabrication of homogeneous and compositionally graded $CuIn(SeS)_2$ thin films.

1.2 Si-based Solar Cells

Amorphous silicon (a-Si) PV modules were the first thin-film PV modules to be commercially produced and are presently the only thin-film technology that has an impact on the overall PV markets. However, the efficiencies of these modules have not yet reached the levels that were predicted in the 1980s. To a significant degree this is due to the intrinsic degradation of a-Si under illumination. The amount of light-induced degradation can be limited to 20% in modules operating under prevailing outdoor conditions. The use of multijunction devices (allowing the use of thinner absorber layers in the component cells) and the use of light-trapping appear to be the most powerful device design schemes to improve stabilized device performance.

The US industry currently uses two approaches to build a-Si-based modules. The substrate type devices are built on stainless steel foil. The superstrate devices are built on glass coated with

TCO. Presently, all superstrate devices use an a-SiC p-layer while substrate devices use a "μc–Si" p-layer, which is, in fact, a mixture of a-Si and μc-Si phases. Fabricating devices with p-layers having wider bandgaps and higher conductivity is expected to lead to higher V_{oc} and higher blue response, hence J_{sc}. Further, such highly conductive and transparent layers will reduce electrical and optical losses at the n/p interconnect junction of multijunction devices. Thus, improvements in p-layers would benefit both superstrate and substrate device technologies, in either single or multijunction configurations.

Another approach to low cost Si-based PV modules involves the deposition of thin films (<20 μm) of large grain (>1 μm) polycrystalline Si on low cost substrates. This requires high growth rates and the ability to form large grains either directly or in post-deposition processing.

1.3 CdTe/CdSe-based Solar Cells

Fabricating high efficiency CdTe/CdS superstrate devices when using ultra-thin CdS window layers presents a difficult technical challenge because of the coupled nature of the processing steps and of the interaction between CdS and CdTe films. We and others have shown that simply reducing CdS thickness to reduce parasitic absorption does not lead to the expected increase in performance, since the junction quality is found to progressively deteriorate (as measured by a loss in V_{oc} and FF) as final CdS thickness in the device is reduced below 100 nm. The extent of this phenomenon is: 1) process specific; 2) more serious for processes in which the CdTe layer is deposited at temperatures below 400ºC; and 3) related to consumption or even disappearance of a continuous CdS layer. In addition, reducing CdS thickness exposes the TCO/glass materials to interaction with the chemical treatment ambient, which can result in loss of adhesion or contamination. The loss of CdS due to diffusion into CdTe is dominated by the grain boundary diffusion. Incorporating S uniformly into the CdTe lattice at concentrations below the solubility limit does not have a deleterious effect on the junction quality. Improving the $CdTe_{(1-x)}S_x$/TCO junction quality for CdTe devices with ultra-thin CdS has been facilitated by use of a high resistance layer between the TCO and CdS films.

There are also serious problems to be solved at the other end of the device, namely the CdTe contact. Prior to forming a low resistance contact to CdTe, the surface must be modified to remove oxides and residues and produce a Te-enriched layer. Nearly all contacting schemes follow this step with application of a copper-containing contact or copper layer and a heat treatment. Analysis of the resulting surface reveals that low resistance contact operation is facilitated by formation of a very thin Cu_2Te layer between CdTe and the current-carrying material. In stress-degraded devices, removing the current-carrying contact, re-etching the surface, and re-applying a contact removes the leaky diode "blocking" behavior. Thus, this behavior can be attributed to the CdTe/contact interface.

This report addresses diffusion of CdS in CdTe, window layer processing, and mechanisms of device stability. A detailed model of CdS diffusion into CdTe thin films, refinement of the CdTe-CdS pseudobinary phase diagram, and processing alternatives for limiting CdS diffusion are presented. Film properties and device results are presented for physical-vapor deposited devices with ultra-thin, <80 nm CdS window layers with and without high resistance oxide buffer layers and $Cd_{1-x}Zn_xS$ window layers. An analysis of stress-induced degradation is presented and a phenomenological model for junction and contact changes is proposed.

1.4 Training and Education

During the period of this subcontract (August 24, 1999 to August 23, 2000) IEC provided training and education for the following: two visiting professionals; five post-doctoral fellows; six graduate students; and nine undergraduate students. One of our visiting professionals was a Fulbright scholar. Names are given in the list of contributors.

1.5 Publications

As a result of research performed under this subcontract, IEC published 10 papers.

1.6 Organization of the Report

This report is organized into three technical sections: $CuInSe_2$-based solar cells, Si-based solar cells, and CdTe-based solar cells. Each section describes the progress made at IEC in addressing the critical issues discussed above during the 12-month period of this subcontract.

2 $CuInSe_2$-BASED SOLAR CELLS

2.1 In-line Evaporation of $Cu(InGa)Se_2$

In-line evaporation is a promising approach to meeting the requirements of uniform deposition over a large area and high substrate throughput for the commercial manufacture of $Cu(InGa)Se_2$ photovoltaic modules. The in-line process, shown schematically in Figure 1, involves the linear translation of a heated substrate over an array of sequential Cu, Ga, In, and Se sources which are designed to give uniform deposition perpendicular to the direction of translation. This system geometry results in variable incident fluxes as the substrate moves through the deposition zone, allowing graded Ga/(Ga+In) films and the incorporation of Cu-rich and -deficient growth stages. The potential of in-line evaporation has already been demonstrated [1,2].

In this report, the operational validation of the in-line system for $Cu(InGa)Se_2$ evaporation at IEC is presented with results of a preliminary experimental characterization of the elemental deposition profiles. The operational validation included measuring deposition uniformity across the substrate width, run-to-run reproducibility, and consistency of device performance. The system reproducibly produced devices in the 13-14% range for absorber thickness ranging from 1.3-2.1 micron, with a best device of 14.9%. The thickness profile of the Cu deposition is shown both parallel and perpendicular to the direction of substrate translation. This distribution, applied to the Ga and In sources, can be used to calculate the relative Ga/(Ga+In) distribution in the film. An Auger compositional depth profile shows that the Ga and In maintain these gradients in the films but the Cu is uniformly distributed.

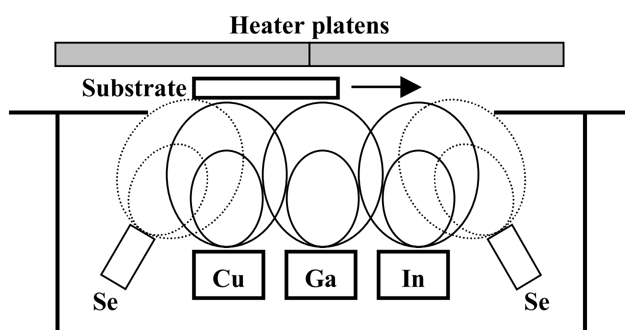

Figure 1. Process schematic for CIGS in-line deposition.

2.1.1 In-line Evaporation System Description

The IEC in-line evaporation system, shown in Figure 1, is designed to deposit over a 12" wide web at translation speeds up to 20"/min, though it is presently configured for 6" wide substrates. Each elemental effusion source has two nozzles spaced 4.6" apart. In the standard configuration, shown in Figure 2, the sources are placed 3.5" apart in the sequence Cu-Ga-In, with the Ga source at the halfway point of the deposition zone and the In source closer to the exit side of the zone. The deposition zone is 15" long and is 9.25" above the sources.

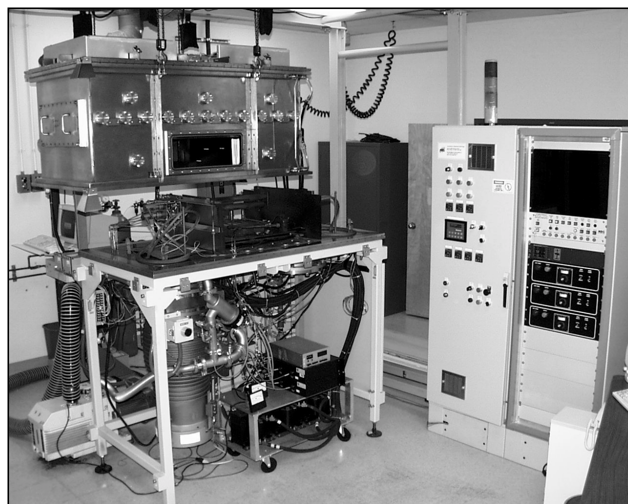

Figure 2. IEC $Cu(InGa)Se_2$ in-line evaporation system.

The substrate is heated by two independently controlled heater platens. The platens are sufficiently longer than the deposition zone so that they heat the substrate before, during, and after deposition. The heater platens are arranged sequentially in order to minimize substrate temperature deviation due to varying thermal radiation from different elemental sources. The substrate temperature is monitored using a bare-junction thermocouple cemented to the substrate surface. The process is housed in a chamber measuring 64"L x 33"W x 27"H. The base pressure is $5x10^{-8}$ T, with a typical operating pressure of $2x10^{-5}$ T.

Temperature control is used for the heater platens and selenium source. Cu, Ga, and In sources are controlled by ATOMICAS™ atomic absorption spectroscopy systems while source temperatures are monitored by thermocouples. Presently, all of the system components are being operated using independent PID control loops.

A model-based control strategy is currently being developed under a separate contract funded by a commercial manufacturer and the Delaware Research Partnership. This will integrate multiple sensor measurements and will improve measurement accuracy, reliability, and transient response. Improvement of measurement accuracy and sensor reliability can be achieved through the use of multiple sensors – for example, the use of both AAS and thermocouple measurements for an effusion source. A model-based controller can track both of these measurements, and then estimate the "true" source effusion rate based on the confidence level of each of these measurements. This is especially useful in the case of extended depositions, during which sensor drift may be expected. The use of multiple sensors also allows redundancy in the case of a sensor failure, thereby improving reliability. The transient response of the system can be improved by anticipating the effects of thermal coupling between different system components. An increase in the Cu source power may cause an increase in Ga source temperature or AAS signal. A model-based control system can anticipate the deviation in the Ga source, and appropriately decrease the gallium source power before the deviation occurs.

2.1.2 In-line System Performance

The compositional uniformity across the 6” wide substrate (in the *cross-direction*) was characterized by EDS measurement. The data, shown in Figure 3, indicate uniform Cu/(Ga+In) and Ga/(Ga+In) ratios within the uncertainty of the EDS.

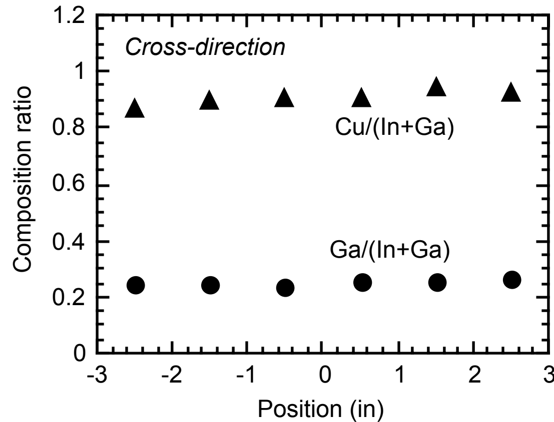

Figure 3. Compositional uniformity across the deposition zone.

In order to evaluate the system performance, a number of films were deposited at different substrate translation speeds, from 1”/min to 2.5”/min at a substrate temperature of 525ºC. The source effusion rates were held constant, so that the films would vary in thickness but retain a fixed composition. Film composition was characterized by EDS, and the film quality by the performance of solar cells fabricated from them. Figure 4 shows the film composition at the center of the substrate, and indicates good run-to-run reproducibility. The best solar cell result from each run is shown in Table 1, again indicating good system reproducibility as well as high film quality in terms of device performance over a 2.5 times range of deposition rates. It should be noted that, with respect to film thickness, the drop in performance for thickness $< 1 \mu m$ is consistent with the work of Negami et al. [3].

The best device produced in the system to date had V_{OC} = 0.606 V, J_{SC} = 33.2 mA/cm^2, FF = 74.3%, and eff. = 14.9% under 100 mW/cm^2 AM1.5 illumination as measured at NREL. The $Cu(InGa)Se_2$ for this device was 1.8 μm thick and deposited at 525ºC. EDS measurements of the absorber layer gave Cu/(In+Ga) = 0.85 and Ga/(In+Ga) = 0.35.

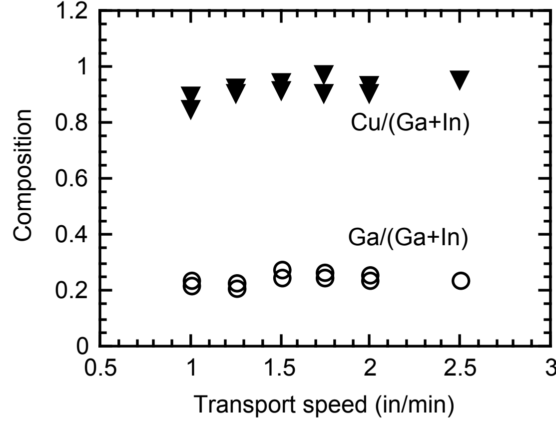

Figure 4. Composition reproducibility at the center of the substrate over 6 runs with different substrate transport speed.

Table 1. Device performance with increasing translation speed.

Speed (in/min)	Thickness (µm)	V_{OC} (V)	J_{SC} (mA/cm^2)	FF (%)	Eff (%)
1	2.1	0.594	32.1	69.4	13.2
1.25	2	0.594	32.5	71.8	13.8
1.5	1.8	0.614	33.2	71.7	14.6
1.75	1.4	0.588	33.7	70.5	14.0
2	1.3	0.590	33.6	67.8	13.5
2.5	0.9	0.570	31.9	66.3	12.2

In summary, the system is capable of reproducibly depositing uniform, device quality $Cu(InGa)Se_2$ films at relatively high deposition rates.

2.1.3 Characterization of Compositional Profiles

A quantitative description of the incident fluxes at the substrate is necessary to characterize the in-line deposition of $Cu(InGa)Se_2$ films. A model of the deposition onto a moving substrate from a multi-nozzle evaporation source was previously reported for the case of large-area CdS deposition [4]. In that case, the flux composition inherently maintained the correct stoichiometry since CdS evaporates congruently. However, characterization of $Cu(InGa)Se_2$ film growth from elemental sources requires a quantitative description of the spatial distribution of multiple elemental fluxes.

The source geometry used for the description of the flux profiles is shown in Figure 5 where the vector (ρ, θ) points from the source to a given point on the substrate. The flux profile for the effusion source can be approximated using:

$$f(\rho,\theta) = \frac{F(n+1)}{2\pi\rho^2}\cos^n\theta \quad (1)$$

where n is an empirical fitting parameter describing the distribution of the molecular beam [5]. The accumulation rate, f^{dep}, at the substrate is obtained by multiplying Eq. 1 by an additional cos θ correction to account for the angle of incidence. F is the effusion rate from the source.

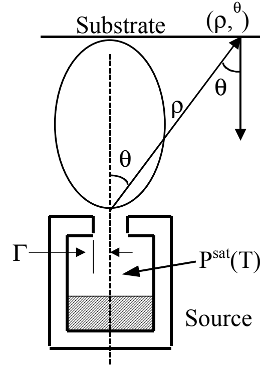

Figure 5. Variables used in effusion analysis.

The measured film thickness profiles for a Cu film deposited onto a large-area (16" x 14"), stationary substrate are shown in Figure 6 and Figure 7 for the cross-direction and the *machine-direction* (along the direction of substrate translation), respectively. The flux as represented by the thickness at the substrate edges (+3 and –3 inches) is 10-15% less than the flux at the center, giving a thickness uniformity of ±5-7%. The data were fit by using Eq. 1 for each source nozzle, with n as the fitting parameter. The best fit, shown as the solid lines in Figure 6 and Figure 7, was obtained for n = 5. Figure 7 also shows the relative error between the fit and the data. The predicted profile is within the bounds of published effusion profiles for nozzles with similar aspect ratios [6]. The flux profile measured for Cu is assumed to apply to the Ga and In sources as well.

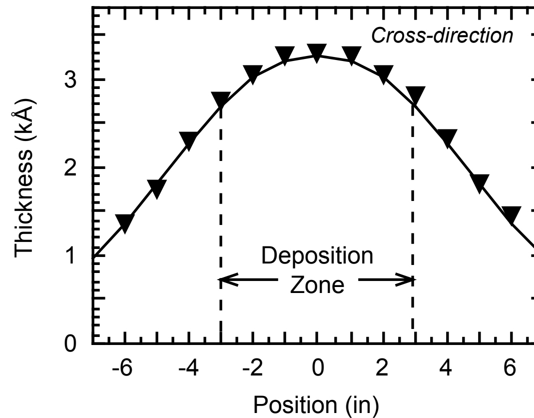

Figure 6. Cu thickness profile across the deposition zone.

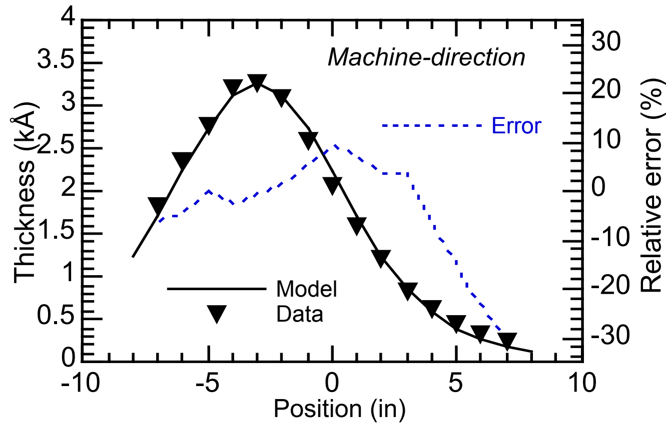

Figure 7. Cu thickness profile along the deposition zone length.

Elemental incident fluxes calculated from Eq. 1 with n = 5 are shown in Figure 8 for a typical film grown at a substrate speed of 1"/min. These profiles are used to predict the film growth rate and composition gradients in the growing film. Figure 9 demonstrates how the in-line system mimics a "two-stage" growth process (Cu-rich to Cu-poor) as the substrate moves through the deposition zone. The film is Cu-rich through nearly the whole of the deposition. The film reaches its target Cu/(Ga+In) ratio within only an inch or so of the deposition zone exit.

Figure 10 shows the Auger depth profile of a $Cu(InGa)Se_2$ film grown at 1"/min and substrate temperature of 525 °C. The data show a flat Cu profile, unlike that shown in Figure 8, indicating Cu homogenization, giving evidence for high Cu mobility. Also, the Cu/(Ga+In) ratio from the Auger data compares quite well to the endpoint value of the model-predicted Cu/(Ga+In) ratio in Figure 9. The data also show that Ga and In retain a grading consistent with their sequence of deposition – that is, Ga-rich near the Mo interface, In-rich near the surface.

A more complete model of the source fluxes in different flow regimes is being developed under a separate contract.

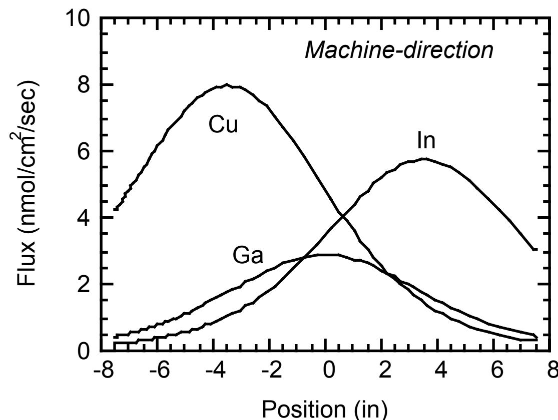

Figure 8. Predicted elemental flux profiles along deposition zone centerline in machine direction.

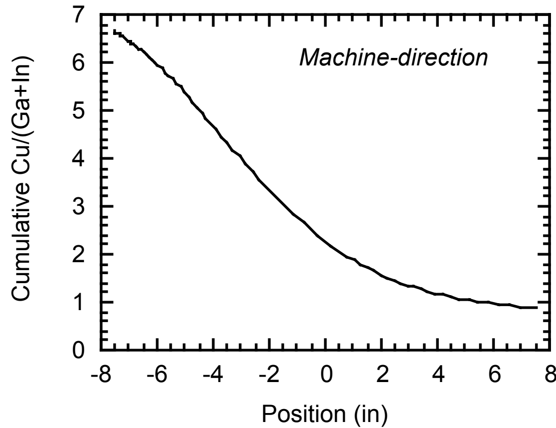

Figure 9. Predicted Cu/(Ga+In) development as the substrate moves through the deposition zone.

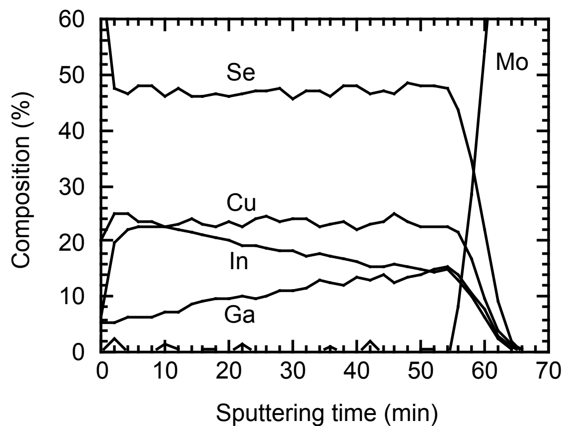

Figure 10. AES depth profile of $Cu(InGa)Se_2$ film deposited at 525ºC and 1"/min.

2.2 Effect of Deposition Temperature on $Cu(InGa)Se_2$ Films and Devices

The effect of substrate temperature (T_{ss}) on material properties of $Cu(InGa)Se_2$ thin films and devices fabricated from them has been characterized. A greater understanding of the effect of temperature is needed to enable development of a process for improved device performance with T_{ss} = 400°C. This lower temperature would enable the use of alternative substrate materials and may reduce processing costs for large area $Cu(InGa)Se_2$ deposition.

We have previously characterized films and devices with T_{ss} = 550°C and 400°C for the deposition of $Cu(InGa)Se_2$ by physical vapor deposition using multisource elemental evaporation [7]. In that work, different evaporation flux profiles were used to characterize the effect of Cu-rich film growth and T_{ss} on grain size, morphology, compositional uniformity, and device performance. In this report, films and device results for $Cu(InGa)Se_2$ films deposited at T_{ss} = 480°C are presented and compared to the previous results. The 480°C intermediate temperature puts the substrate safely below the strain point for soda lime glass, which should reduce the handling problems caused, by transporting large substrates of hot glass.

$Cu(InGa)Se_2$ films were deposited by thermal evaporation from independently controlled elemental sources for the Cu, In, Ga, and Se. Three temporal deposition flux profiles were used to give depositions with: (1) uniform fluxes so that the films composition was never Cu-rich; (2) Cu-rich flux, Cu/(In+Ga) > 1, at the beginning of the run followed by only In, Ga, and Se fluxes to give the desired Cu-deficient final composition; and (3) Cu-rich flux in the middle of the run. These are shown schematically in Figure 11. The process with the Cu-rich flux in the middle is intended to distinguish if the effects of Cu-rich growth specifically require the presence of a Cu_xSe_y phase during the initial nucleation of the film on the glass/Mo substrate.

The In, Ga, and Se fluxes were kept constant throughout each deposition, so there were no gradients in Ga content or bandgap, and were the same for each flux profile. The differences in the depositions, then, were only in the Cu fluxes. The deposition time for all films was 44 min. and the final film thicknesses were ~ 2.5 µm. All films used for morphological characterization and devices had a final composition, measured by energy dispersive x-ray spectroscopy (EDS), with Cu/(In+Ga) = 0.8 – 0.9 and Cu/(In+Ga) ≈ 0.3. This gives a bandgap of E_G = 1.2 eV.

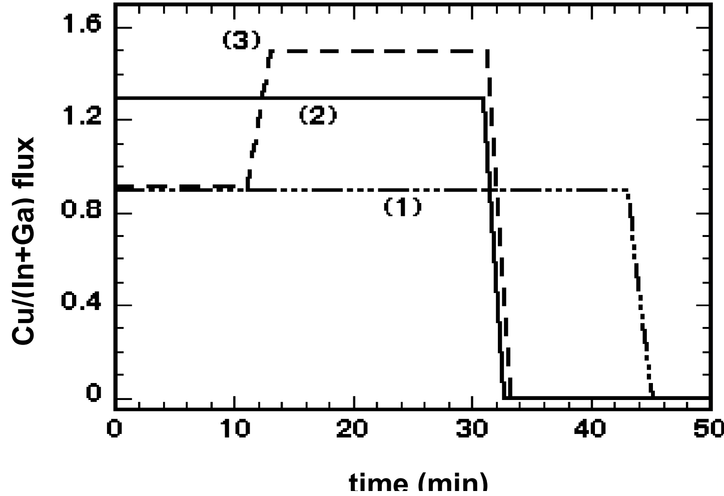

Figure 11. Schematic representation of three temporal flux profiles for $Cu(InGa)Se_2$ evaporation, as described in the text.

The grain size distribution was determined from AFM images of the top surface. Three images from each film sampling a total of 300 µm^2 were digitized to determine the grain sizes [7]. These distributions are shown in Figure 12 for the 3 different growth processes with T_{ss} = 480°C. As with films grown at 400 and 550°C, the grain areas are well described by a log-normal distribution, i.e., a normal distribution of the logarithm of *A* [8]:

$$f_n(\ln A) = \frac{1}{\sigma(\ln A)\sqrt{2\pi}} \exp\left[-\frac{(\ln A - E(\ln A))^2}{2\sigma(\ln A)^2} \right]. \qquad (2a)$$

Here E(ln*A*) is the expected value or mean of ln*A* and σ(ln*A*) is the standard deviation of this distribution. The mean grain area $\bar{A}$ is given by [8]:

$$\overline{A} = \mathrm{E}(A) = \exp\left[\mathrm{E}(\ln A) + \tfrac{1}{2}\sigma(\ln A)^2\right] \quad (2b)$$

The mean and standard deviation of ln$A$ determined by the fits shown in Figure 12 are listed in Table 2 along with the $\overline{A}$ calculated from Eq. 2b. These values are compared to those obtained by similar analysis for films deposited at T_{ss} = 400 and 550°C. The films grown at 480°C have comparable mean grain area for the three different deposition processes. The grain size is greater only for the Cu-rich growth processes at 550°C.

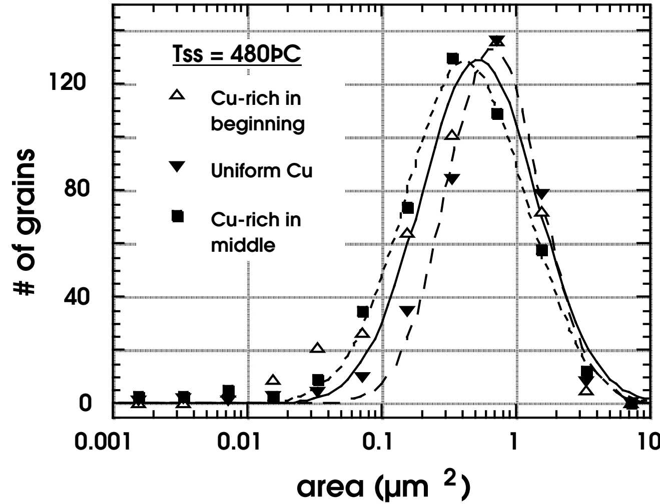

Figure 12. Grain size distributions for three growth sequences at T_{ss} = 480ºC with log-normal fit to each distribution.

Table 2. Mean grain area with different substrate temperature.

Tss (°C)		Process: Uniform	Cu-rich in beginning	Cu-rich in middle
400	E(ln$A$)	-1.9	-1.9	-1.9
	σ(ln$A$)	1.1	1.1	1.2
	$\overline{A}$ (µm²)	0.3	0.3	0.3
480	E(ln$A$)	-0.4	-0.7	-0.9
	σ(ln$A$)	0.7	1.0	1.0
	$\overline{A}$ (µm²)	0.9	0.8	0.7
550	E(ln$A$)	-1.0	-0.7	-0.6
	σ(ln$A$)	1.1	1.6	1.2
	$\overline{A}$ (µm²)	0.7	1.8	1.2

The depth profiles of the compositions through the films deposited with the different processes at 480°C were measured by Auger electron spectroscopy (AES) to determine if the differences in the fluxes lead to differences in the compositional distribution. The ratios Cu/(In+Ga) and Ga/(In+Ga) from the AES results are shown in Figure 13 for the three different deposition processes. In each case there is a drop off in Cu/(In+Ga) near the front surface as is typically

seen in $Cu(InGa)Se_2$ films but no significant difference in the profiles otherwise. The Cu, In, and Ga are all uniformly incorporated in spite of the difference in flux profiles.

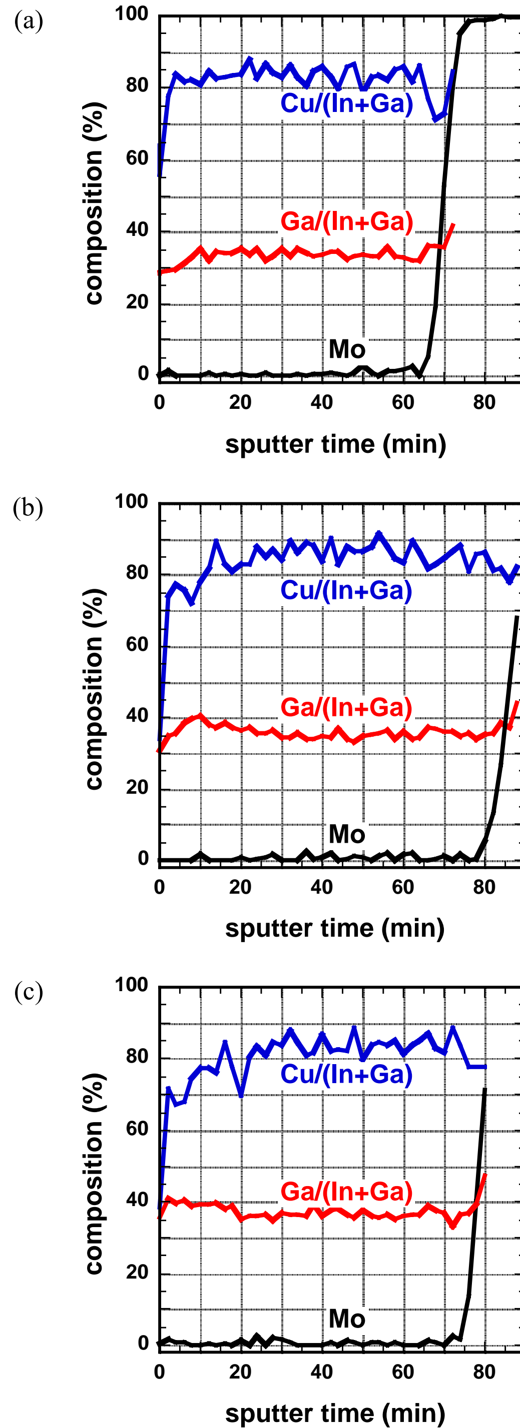

Figure 13. Compositional ratios Cu/(In+Ga) and Ga/(In+Ga) determined from AES depth profiles for films deposited at T_{ss} = 480°C with (a) uniform fluxes, (b) Cu-rich flux in the beginning of the deposition, and (c) Cu-rich flux in the middle of the deposition.

Devices were fabricated using a baseline process with structure: soda lime glass / Mo / $Cu(InGa)Se_2$ / CdS / ZnO:Al / Ni-Al grids. There is no anti-reflective layer on any of these devices. Cells are mechanically scribed with area ≈ 0.47 cm^2 and are measured on a total area basis. The results of the best cells fabricated to date for T_{ss} = 400, 480, and 550°C and the three deposition processes are listed in Table 3. Two conclusions can be drawn from these results. First, the uniform deposition process gives poorer device performance at T_{ss} = 400°C than the Cu-rich growth processes but at higher temperatures, 480°C and 550°C, there is no advantage to the Cu-rich growth. Second, there is a significant increase in V_{oc} and FF with the increase in T_{ss} from 480°C to 550°C, despite the comparable grain sizes measured in the films deposited at these temperatures.

Table 3. Device results with different substrate temperature and evaporation process.

T_{ss} (˚C)	Process	V_{oc} (V)	J_{sc} (mA/cm^2)	FF (%)	η (%)
400	Uniform flux	0.56	29	69	11.3
	Cu-rich at beginning	0.59	33	71	13.7
	Cu-rich in middle	0.60	33	71	13.8
480	Uniform flux	0.60	32	72	14.0
	Cu-rich at beginning	0.62	32	72	14.4
	Cu-rich in middle	0.63	30	71	13.4
550	Uniform flux	0.65	33	74	15.9
	Cu-rich at beginning	0.65	32	76	16.0
	Cu-rich in middle	0.65	32	75	15.5

2.3 Formation and Analysis of Graded $CuIn(SeS)_2$ and $CuGa(SeS)_2$ Films

Alloy materials based on $CuInSe_2$ are potential absorber layers for wide bandgap, E_g > 1.5 V, heterojunction solar cells. High performance, wide bandgap, solar cells could: 1) improve module performance and reduce module cost; and 2) provide the wide bandgap device needed for 'next generation' monolithic tandem devices. Graded bandgaps could be used to improve V_{oc} of present generation devices by allowing incorporation of graded bandgap structure into the junction region. The Cu-In-Ga-Se-S chalcopyrite materials system, $CuInSe_2$ ⇔ $CuInS_2$ ⇔ $CuGaSe_2$ ⇔ $CuGaS_2$, can be developed to yield bandgaps from 1.0 to 2.5 eV, since alloys of these compounds form continuous solid solutions. At present, substitution of Ga for In to form alloys has resulted in the highest performance devices, but at Ga/(Ga+In) > 0.5, with E_g > 1.3 eV, the device performance decreases [9]. Siemens Solar Industries utilizes a graded $Cu(InGa)(SeS)_2$ film structure where the junction region is alloyed with sulfur to increase V_{oc}, while the back contact region is alloyed with gallium [10].

In this report, formation of $CuIn(Se_{1-y}S_y)_2$ alloy films is addressed with respect to formation of graded structures and providing a quantitative basis for characterizing the film formation process. The experimental approach consists of reacting $CuInSe_2$ films in flowing H_2S/Ar atmosphere at 450°C to 525°C to convert films completely to $CuInS_2$, or to produce graded

$CuIn(Se_{1-y}S_y)_2$ alloy films. A model of the reaction/diffusion conversion process was developed and a method to quantitatively analyze the process is presented that predicts the compositional distribution of the converted films. The methodology is similar to that recently reported for analyzing CdS/CdTe thin-film couples [11]. Finally, the reaction of sulfur with films of different starting composition has been characterized. This includes comparison of $CuInSe_2$ and $CuGaSe_2$ films and of Cu-rich and Cu-poor films.

2.3.1 Sulfur Reaction Experimental Procedures

The samples used for this study were 2 µm thick $CuInSe_2$ films deposited onto Mo coated soda lime glass by co-evaporation from elemental sources at a substrate temperature of 550°C. The composition of the films, determined by energy dispersive x-ray spectroscopy, was Cu = 25 at%, In = 25 at% and Se = 50 at%. A laminar flow thermal CVD reactor was used to react $CuInSe_2$ at atmospheric pressure. Samples were ramped to reaction temperature over a 10-minute interval in Ar atmosphere and held for 30 minutes before introducing H_2S. The gas composition was 2% H_2S in Ar and the total flow rate was 1320 sccm, giving a linear flow velocity of 76 cm/min. The samples were treated for a specified time and then pulled out of the hot zone. H_2S gas flow was simultaneously terminated and power was removed from the heating mantle. The system was then allowed to cool to room temperature under flowing argon and the substrate temperature dropped from 500°C to below 200°C within 2 minutes. In this way, $CuInSe_2$ samples were sulfurized at 450°C, 500°C and 525°C for 20, 40 and 60 minutes.

Film thickness and grain columnarity were analyzed by scanning electron microscopy (SEM) and transmission electron microscopy (TEM) of cross-sections. Film grain size and morphology was analyzed by surface atomic force microscopy (AFM) using a Digital Instruments model 3100 Nanoscope in tapping mode. Reacted $CuInSe_2$ films were etched to reveal grain boundaries using 1% Br_2 by mass in methanol at room temperature. The etch process removed approximately 0.25 µm from the surface of the films and revealed the grain boundaries. After etching, 10 x 10 µm areas were scanned in four random regions on each sample to provide a statistically significant sampling of > 400 grains on each sample. The features interpreted as grain boundaries were traced onto transparent film and the grains were categorized into discrete size bins, determined by averaging the major and minor axis of each grain. The resulting distributions were found to conform to a log normal distribution, expressed in this case in terms of the grain diameter *D*:

$$f_n(\ln D) = \frac{1}{\sigma(\ln D)\sqrt{2\pi}} \exp\left[-\frac{(\ln D - E(\ln D))^2}{2\sigma(\ln D)^2}\right] \quad (3)$$

where D^* is the mean grain diameter and σ is the standard deviation. This is the commonly observed distribution for films with *normal*, or continuous, grain growth [12]. A typical AFM image is shown in Figure 14. The binned grain sizes and fitted distribution are shown as the data points and line, respectively, in Figure 15. For this film, the mean grain diameter was 0.6 µm. The distributions of all films examined in this work conformed to a similar function; it is important to note that grain shape, distributions, and film orientation were preserved throughout the reaction process.

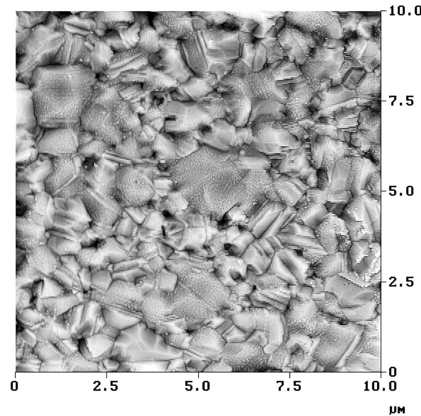

Figure 14. Atomic force micrograph of etched $CuInSe_2$ film.

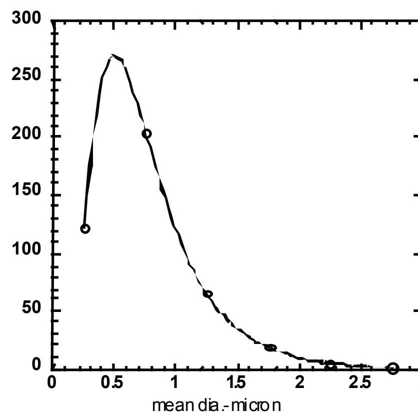

Figure 15. Grain size distribution of etched $CuInSe_2$ film.

XRD line profiles of the $CuIn(Se_{1-y}S_y)_2$ (112) reflection were measured using a Phillips/Norelco Bragg-Brentano focusing diffractometer with 35 kV Cu-kα radiation and a graphite crystal monochrometer. Line profiles were acquired by step scanning in 0.01° intervals from 26.0 to 28.5° in 2θ. The x-ray diffraction data was smoothed and the kα_2 component was stripped using the Rachinger correction. For comparison purposes, the backgrounds were removed, and the resulting profiles were normalized to equal area. Because the films were nominally the same thickness, had similar (112) texture, and since the (112) structure factor from $CuInSe_2$ to $CuInS_2$ varies by only ~15%, very little normalization was necessary.

2.3.2 Equilibrium Thermochemistry and Diffusion Model

The net chemical reaction of $CuInSe_2$ in H_2S gas is:

$$2H_2S(v) + CuInSe_2(s) \leftrightarrow 2H_2Se(v) + CuInS_2(s)\,, \qquad (4)$$

with free energy of reaction $\Delta G_{450°C} = +12.86$ kcal/mol, taking into account gas and solid phase mixing enthalpy [13]. Note that the minimum chemical energy is attained by formation of the

$CuIn(Se_{1-y}S_y)_2$ alloy, and the solid phase concentrations in Eq. 4 represent the molar fractions in the alloy. The equilibrium constant for the reaction is thus expressed:

$$k = \frac{[CuInS_2][H_2Se]^2}{[CuInSe_2][H_2S]^2} = \left(\frac{1-x}{x}\right)^2 \left(\frac{y}{1-y}\right), \text{ where} \quad (5)$$

$$x = \frac{[H_2S]}{[H_2S]+[H_2Se]} \text{ in the gas phase, and } y = \frac{S}{Se+S} \text{ in the film.} \quad (6)$$

Thus, annealing a $CuInSe_2$ film in a closed system with H_2S gas, the equilibrium state will consist of a $CuIn(Se_{1-y}S_y)_2$ in a H_2S + H_2Se atmosphere. The flowing reactor employed deviates from the closed system by constantly removing H_2Se while replenishing H_2S. The reaction rates to form $CuInS_2$ are assumed to be faster than solid state diffusion, resulting in formation of a $CuInS_2$-rich surface layer, which acts as a constant diffusion source in a couple with $CuInSe_2$. The process is modeled by assuming a pseudo-steady state with a surface reaction that continuously forms a $CuInS_2$ surface layer that provides a constant diffusion source. The $CuInS_2$-$CuInSe_2$ diffusion couple is assumed to follow Fick's Law with S and Se species diffusing into bulk crystallites and along grain boundaries. The sulfur concentration of the surface layer, c_o , depends on the kinetics of the surface reaction and the removal of Se from the gas phase. Thus, c_o was a function of the S/(S+Se) ratio in the surface layer and was used as a fitting parameter in the analysis. Although the diffusion mechanism is not yet known, the treatment of diffusion does not rely on a particular mechanism, but rather all operating mechanisms are lumped into a species-independent effect described by net bulk, D, and a grain boundary, D_b, diffusion coefficients.

A cylindrical representation of $CuInSe_yS_{1-y}$ grains was adopted to model bulk and grain boundary diffusion. The 2-dimensional analytical solution developed by Gilmer and Farrell for polycrystalline films was employed using a constant diffusant source, reflecting back surface, and isolated grain boundaries [14]. Using measured grain size distributions and grain boundary width, estimated from TEM analysis to be ~20Å, 3-dimensional $CuIn(Se_{1-y}S_y)_2$ alloy distributions were determined for individual grain sizes and integrated to generate compositionally broadened x-ray diffraction (112) line profiles. Line profiles were generated by convolution of the Pearson VII function with the volume fractional alloy distribution function obtained from the model and corrected for absorption [15]. The modeled x-ray diffraction line profiles were regressed with measured profiles, using the bulk and grain boundary diffusion coefficients and surface source layer composition as the fitting parameters. The diffusion coefficients were determined at fixed temperature for times ranging from 20 to 60 minutes. The precise value of the grain boundary width is not critical to this analysis. This is because the grain boundary width and the grain boundary diffusion coefficient have an approximately multiplicative relationship. Details of the model will be presented in a forthcoming paper.

2.3.3 Sulfur Reaction Results

Measured and modeled XRD (112) line profiles for $CuInSe_2$ films reacted at 500°C for 20, 40 and 60 minutes are shown in Figure 16. There is a time-progressive shift of the profile towards the expected location of pure $CuInS_2$, and after 60 minutes the film composition approaches uniform $CuInS_2$. Determining the precise solid state source composition *a priori* would require detailed knowledge of the solid-vapor steady state in each case. AES analysis of the near-surface

region of selected samples showed that the c_o values used to fit modeled to measured XRD line profiles were within 10% of measured surface S/S+Se composition [16]. For reaction at 500°C, all treatment times yielded the same net bulk and grain boundary diffusion coefficients: D = 3.0 x 10^{-12} cm^2/sec and D_b= 3.0 x 10^{-10} cm^2/sec, respectively. Fitted diffusion coefficients and surface source compositions for the time-progressive data at 500°C and for selected times at different temperatures are listed in Table 4. Data for reactions at different temperatures from Table 4 yields the following estimates of the activation energy for net bulk and grain boundary diffusion coefficients: E_D = 1.0 eV and E_{Db} = 0.4 eV, respectively.

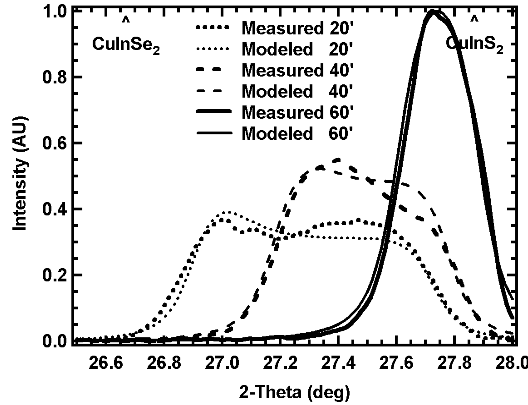

Figure 16. Measured and modeled time progressive x-ray diffraction (112) line profiles for $CuInSe_2$ films reacted in H_2S at 500°C.

Table 4. Diffusion coefficients and surface source compositions.

Temp (C)	Time (min)	D (cm^2/sec.)	D_b (cm^2/sec.)	c_o S/(Se+S)
500	20	$3.0x10^{-12}$	$3.0x10^{-10}$	0.88
500	40	$3.0x10^{-12}$	$3.0x10^{-10}$	0.92
500	60	$3.0x10^{-12}$	$3.0x10^{-10}$	1
450	60	$1.2x10^{-12}$	$2.5x10^{-10}$	1
525	20	$6.0x10^{-12}$	$5.0x10^{-10}$	0.88

In conclusion, a method for making thin film $CuIn(Se_{1-y}S_y)_2$ with uniform or graded compositions has been developed and quantitatively analyzed. Estimates of the bulk and grain boundary diffusion coefficients can be used to generate 3-dimension composition maps of the films. If a H_2S/H_2Se mixed gas composition is used during the annealing process, the S/Se composition of either a graded or uniform film can be controlled and used to tailor the bandgap of the material.

2.3.4 Sulfur Reaction Versus Film Composition

The above results were all obtained with $CuInSe_2$ films, which had Cu/In $\geq$ 1. The effect of Cu/In ratio on S reaction has also been characterized. In addition, the above approach for quantitatively characterizing the S reaction is being extended to the reaction $CuGaSe_2$ and

CuInGeSe$_2$ films in H_2S, with the eventual goal of producing Cu(InGa)(SeS)$_2$ with bandgap from 1.5 to1.8 eV.

CuInSe$_2$ and CuGaSe$_2$ films with Cu/In or Cu/Ga ≈ 1.3 and 0.8 were deposited by elemental evaporation onto Mo-covered SL glass substrates. In addition, the experiments included Cu-rich samples etched in KCN before S reaction to remove surface Cu_xSe_y phases, giving films with Cu/In ≈ 1.0. These were intended to determine the effect of the Cu_xSe_y on S-diffusion. All samples were reacted for 60 min at 580°C in 2% H_2S with an Ar balance. After the sulfur reaction, films were characterized by XRD since a reduction in lattice spacing caused by the introduction of S allows for monitoring of the S incorporation. XRD measurements were done under Cr radiation to give greater resolution. The <112> peak positions of the relevant phases in this case are listed in Table 5.

Table 5. Positions for the <112> peaks under Cu and Cr radiation.

material	d-spacing (Å)	<112> peak position (2θ)	
		Cu Kα radiation	Cr Kα radiation
CuInSe$_2$	3.344	26.64	40.04
CuInS$_2$	3.195	27.90	42.00
CuGaSe$_2$	3.221	27.67	41.64
CuGaS$_2$	3.068	29.08	43.82

XRD line profiles for the <112> peak are shown in Figure 17 and Figure 18 for the reacted CuInSe$_2$ and CuGaSe$_2$ films respectively. The XRD profiles for the CuInSe$_2$ films show that the S incorporation into the Cu-rich film is much greater than into the Cu-poor film. S incorporation into the KCN etched sample was greater than the Cu-poor sample but less than the un-etched Cu-rich sample, so that the differences between S-diffusion into the Cu-rich and Cu-poor samples cannot be simply explained by the presence of a Cu_xSe_y surface phase.

The XRD profiles for the CuGaSe$_2$ films after S-reaction show that the S incorporation into the CuGaSe$_2$ is much less than the CuInSe$_2$. There is almost no evidence of S incorporation into the Cu-poor film and, again, the line profile for the KCN etched film falls between those for the Cu-poor and Cu-rich samples.

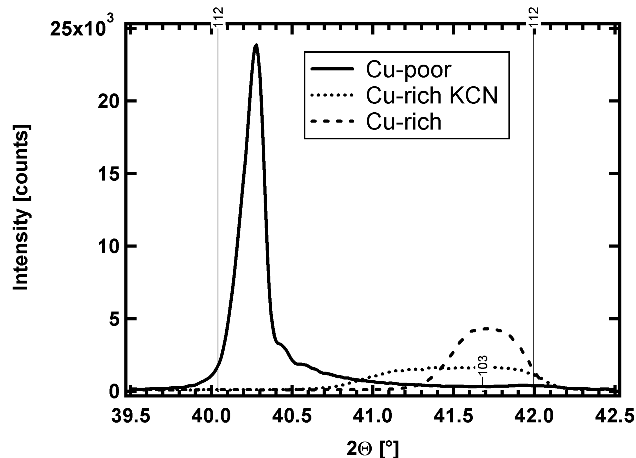

Figure 17. XRD profiles of the <112> peak of $CuInSe_2$ films reacted in H_2S. Measurements were done using Cr Kα radiation.

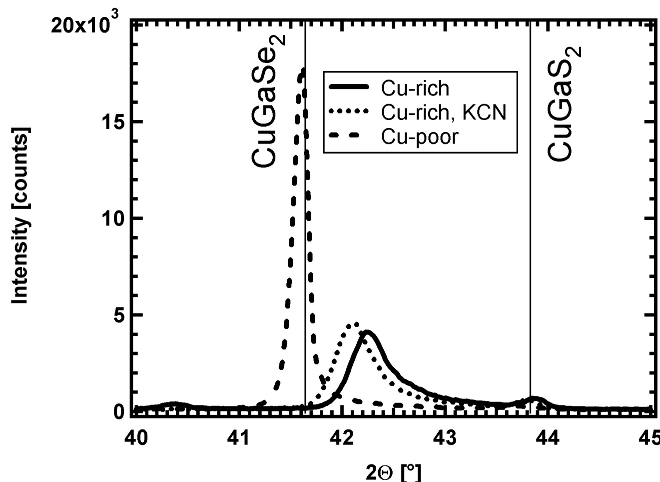

Figure 18. XRD profiles of the <112> peak of $CuGaSe_2$ films reacted in H_2S. Measurements were done using Cr Kα radiation.

In Figure 18, the scans all have a small peak at the position expected for $CuGaS_2$ which indicates a volume of the sample which has reacted completely with S. For the $CuInSe_2$ samples in Figure 17, the scans for the Cu-rich and etched samples extend fully to the $CuInS_2$ peak position. Close examination of the data for the Cu-poor $CuInSe_2$ films also reveals a peak near the position for fully reacted $CuInS_2$. This is seen when the vertical scale is expanded as shown in Figure 19. In this case, the peak could also be due to a $CuInSe_2$ <103> reflection.

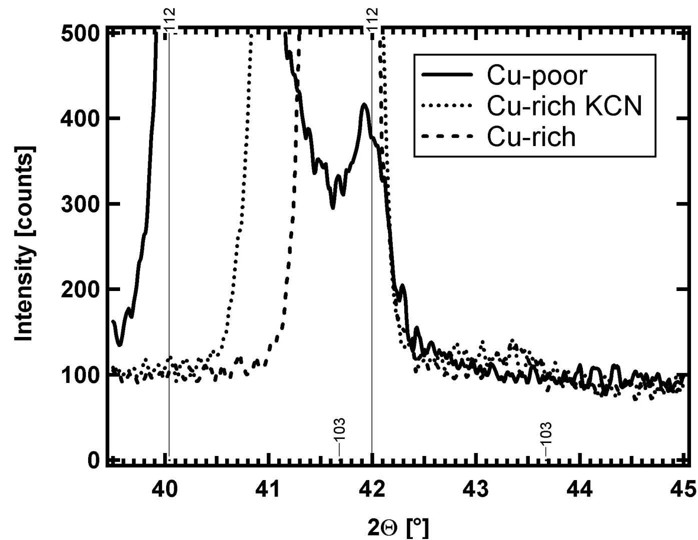

Figure 19. XRD profiles of the <112> peak of $CuInSe_2$ films, from Figure 17, with an expanded y-axis.

To further characterize the Cu-poor $CuInSe_2$ sample, glancing incidence XRD (GIXRD) measurements were done at different incident angles corresponding to different sampling depths. Measurements in this case were done using Cu Kα radiation. For the small incident angles used, the X-ray penetration depth into the samples is roughly proportional to the angle. The X-ray intensity is reduced by a fraction 1/e at a depth 110 nm into the film. At an incident angle of 2° the Mo signal is just barely visible. The measurement time was adjusted in order to achieve the same integrated signal intensity at all angles.

The GIXRD results are shown in Figure 20 for the <220>/<204> reflections. There are no additional peaks in this range to create ambiguity like the <103> peak does in the Figure 19. These scans show a peak at the position of $CuInS_2$ whose relative intensity increases at smaller angles. This indicates that there is a $CuInS_2$ layer at the sample surface.

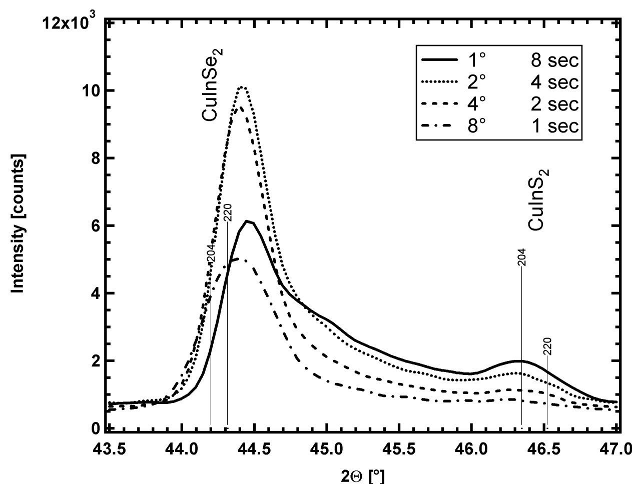

Figure 20. GIXRD scans of the <204>/<220> peak doublet for the Cu poor sample in Figure 17 and Figure 19. Measurements were done using Cu Kα radiation.

The $CuGaSe_2$ films have a stronger signal than the $CuInSe_2$ corresponding to the peak position of a fully reacted sulfide layer. Figure 21 shows the SEM cross-section of the Cu-poor $CuGaSe_2$ sample after sulfurization. Two distinct layers are clearly visible with a thin fine-grain surface layer that was not present before the S reaction. This surface layer could be the sample volume responsible for the $CuGaS_2$ signal.

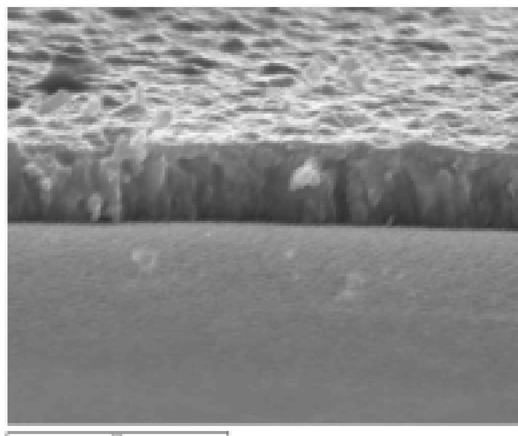

Figure 21. SEM (10,000 X) cross-section of a sulfurized Cu-poor sample showing a discrete surface layer. The line marker is 10μm.

In conclusion, a method for making thin film $CuIn(Se_{1-y}S_y)_2$ with uniform or graded compositions has been developed and quantitatively analyzed. Estimates of the bulk and grain boundary diffusion coefficients can be used to generate 3-dimension composition maps of the films. If a H_2S/H_2Se mixed gas composition is used during the annealing process, the S/Se composition of either a graded or uniform film can be controlled and used to tailor the bandgap of the material. The incorporation of sulfur into $CuInSe_2$ and $CuGaSe_2$ and into Cu-rich and Cu-deficient films has been shown to depend on the starting film composition. Under fixed reaction conditions, less S is incorporated into $CuGaSe_2$ than $CuInSe_2$ and the incorporation of S into Cu-deficient films, with Cu/In or Cu/Ga < 1, is less than films with Cu/In or Cu/Ga ≥ 1. Detailed XRD analysis indicates that a $CuInS_2$ or $CuGaS_2$ surface layer is formed on the Cu-poor films.

3 Si-BASED SOLAR CELLS

3.1 Microcrystalline Silicon Oxide p-layers

3.1.1 Introduction

There has been considerable effort focused on changing the structure of the p-layer from amorphous to "microcrystalline" (μc) in order to improve the performance of a-Si:H based p-i-n solar cells [17,18,19]. These μc layers are typically inhomogeneous with a mix of a-Si or a-Si:C with c-Si crystallites of several tens of nanometers. The grain size, fraction crystallinity, and conductivity depend strongly on extrinsic variables such as the thickness and substrate [20,21,22] and intrinsic variables such as dopant [23,24], H_2 dilution [24] and power [24].

In a previous [24] study we investigated the crystallinity of p-layers deposited from a SiH_4 / CH_4 mixture in a RF PECVD system and showed that c-Si can be obtained at low power density with controllable volume fraction. However, CH_4 tended to inhibit formation of Si crystallinity.

In the present work we investigate RF PECVD deposition and subsequent characterization of microcrystalline p-layers having CO_2 in the feed gas. The goal was to obtain two phase films of crystalline Si imbedded in a matrix of a-SiO_x:H:C [25]. The idea is that such films incorporated in p-i-n type devices could give high currents due to the transparency of the amorphous phase and high voltages due to the highly conductive crystalline phase with a smaller junction surface [19]. Also, the presence of CO_2 in the glow discharge would tend to decrease the reducing effects of the plasma on the thin conductive oxide used as the front contact in superstrate devices.

3.1.2 Experimental Approach

The p-layers were deposited on 7059 glass and on untextured SnO_2 coated soda lime glass substrates, and their crystallinity and deposition rates were determined by Raman spectroscopy [26] and by profilometry. In-plane conductivity and activation energy measurements were also performed on most of the films deposited on glass substrates.

The main experimental variables were the hydrogen dilution and CO_2 content in the feed gases. The secondary parameters were discharge power density and doping gas (B_2H_6) level. In designing experiments and interpreting results normalized flows rather than the actual gas flows were used. These normalized flows were defined as

$$o = f(CO_2) / [f(SiH_4) + f(CO_2)];$$
$$h = f(H_2) / [f(SiH_4) + f(CO_2)];$$
$$b = 2 \text{ x } f(B_2H_6) / [f(SiH_4) + f(CO_2)]$$

For all depositions substrate temperature was kept at 150°C. Except in a few cases, discharge pressure, SiH_4 partial pressure and residence times were also kept constant throughout the study by introducing He to the discharge as a buffer gas.

As a first step, we have performed a deposition under conditions that favor crystallinity in films with CH_4 for the purpose of evaluating crystallinity and carbon and oxygen incorporation into the film (Run #4847). The conditions chosen were: f(SiH_4) = 20 sccm; Power Density = 420 mW/cm^2; Pressure = 1 Torr; h = 154; o = 0.23; b = $1.5x10^{-3}$.

Raman spectra of the films (Figure 22) show the existence of a two-phase mixture consisting of c-Si and amorphous silicon phases. Also, the film deposited on glass seems to have higher amount of c-Si phase (45% vs. 35%).

SIMS depth profile of the films shown in Figure 23 indicate that:

- the composition of the films are independent of the substrate,
- oxygen and carbon content in the films are respectively 10^{22} and $7x10^{20}$.

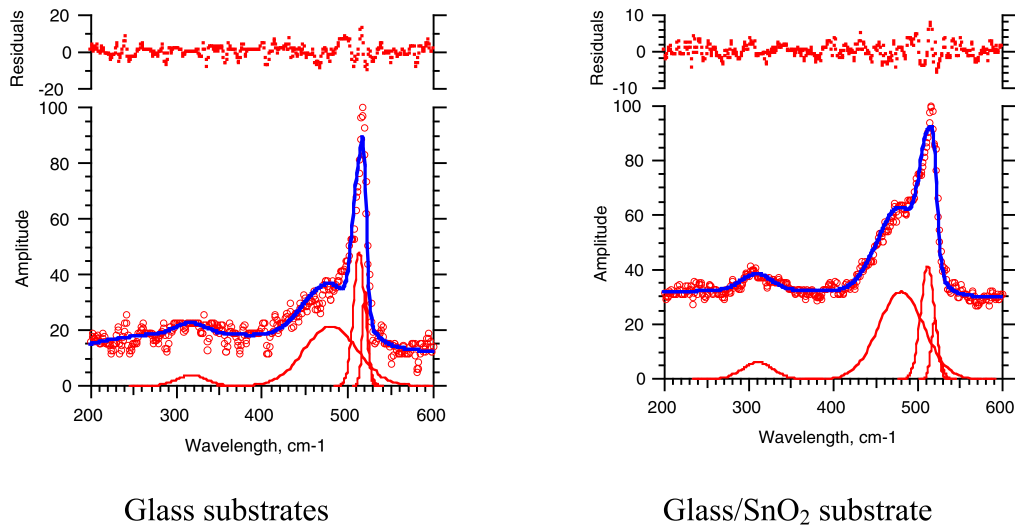

Glass substrates

Glass/SnO_2 substrate

Figure 22. Raman spectra of the films from run #4847.

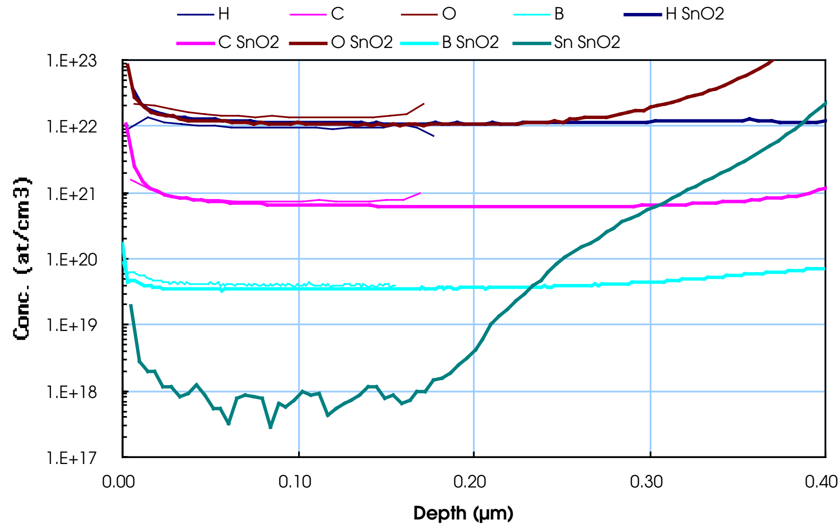

Figure 23. SIMS depth profiles of the films from run 4847. Thinner lines are the film on glass while thicker lines are the film on SnO_2.

It is important to note that since the films have a c-Si and an amorphous phase, the latter must contain almost all the hydrogen, carbon and oxygen observed in the SIMS analysis. Thus, it can be concluded that the amorphous phase is essentially hydrogenated silicon oxide containing small amounts of carbon and boron.

3.1.2.1 Effect of Diborane Level in Discharge

In the next step, films deposited at two different diborane dilutions "b" for a range of hydrogen dilution "h" were investigated for their crystallinity by Raman spectroscopy. The deposition rates were determined by profilometric measurements. Total pressure, silane partial pressure and discharge power density were, respectively, 5 mT, 1 Torr and 168 mW/cm^2. Table 6 summarizes deposition conditions and the measured film properties.

Table 6. Deposition conditions and measured characteristics of films deposited at two different diborane concentrations in the plasma for a range of hydrogen dilutions.

Gas Flows (sccm)							Glass Substrate				SnO_2 Substrate	
SiH_4 (90% H_2)	CO_2	B_2H_6 (99.8% H_2)	H_2	He	b	h	R (Å/s)	σ_d (S/cm)	E_a (eV)	c-Si (Vol%)	R (Å/s)	c-Si (Vol%)
20	0.6	10	0	370	$1.5x10^{-2}$	11	0.46	$3.8x10^{-08}$	0.54	1	0.63	0
20	0.6	10	75	295	$1.5x10^{-2}$	40	0.47	$4.7x10^{-08}$	0.54	5	0.63	0
20	0.6	10	145	225	$1.5x10^{-2}$	67	0.38	$1.3x10^{-04}$	0.15	13	0.63	0
20	0.6	10	232	138	$1.5x10^{-2}$	100	0.44	$1.2x10^{-03}$	0.10	13	0.49	0
20	0.6	10	368	0	$1.5x10^{-2}$	152	0.31	$1.7x10^{-01}$	0.06	42	0.47	16
20	0.6	1	0	380	$1.5x10^{-3}$	7	0.47	$5.0x10^{-11}$	0.70	0	0.76	0
20	0.6	1	40	338	$1.5x10^{-3}$	23	0.24	$1.8x10^{-05}$	0.23	10	0.49	0
20	0.6	1	72	305	$1.5x10^{-3}$	35	0.28	$7.2x10^{-03}$	0.11	36	0.44	0
20	0.6	1	110	270	$1.5x10^{-3}$	50	0.25	$1.3x10^{-01}$	0.07	58	0.42	22
20	0.6	1	150	230	$1.5x10^{-3}$	65	0.21	$1.5x10^{-01}$	0.07	62	0.33	25
20	0.6	1	190	187	$1.5x10^{-3}$	80	0.28	$1.4x10^{-01}$	0.07	67	0.35	43
20	0.6	1	240	138	$1.5x10^{-3}$	100	0.17	$3.1x10^{-01}$	0.06	74	0.28	47
20	0.6	1	381	0	$1.5x10^{-3}$	154	0.11	$2.3x10^{-01}$	0.07	71	0.22	50

First thing to note is that for the diborane concentration of b = 0.0015, the c-Si phase is observed at remarkably low hydrogen dilutions of h = 23 and 50, respectively, for 7059 glass and tin oxide substrates, even at such a low power density utilized here.

More generally, it is found that fraction of c-Si increases with increasing hydrogen dilution and decreases with increasing diborane levels. However, the degree of validity of this observation depends on the film deposition rates. This is because bonding rearrangement on the surface of the growing film that favors c-Si formation will be more extensive for low deposition rates. Consequently, dependence of crystallinity on hydrogen dilution is only clearly in the regions where deposition rates do not change appreciably. The deposition rate argument can also explain the difference in crystallinity between like substrates deposited at different diborane levels.

However, the difference in crystallinity between glass and tin oxide substrates for a given diborane level might also be controlled, in addition to deposition rate, by the possible difference in the initial nucleation rate of crystallites on glass and tin oxide surfaces.

The difference in deposition rates between glass and SnO_2 substrates is most probably due to the voltage difference between substrate and the plasma. In the case of a conductive substrate such as SnO_2 the surface is grounded and the potential difference between substrate and the plasma is the plasma potential. In the case of glass substrate, the potential difference is the floating potential which, in general, is substantially smaller than the plasma potential. Also affecting the deposition rate are hydrogen dilution and diborane levels in the discharge.

Increasing hydrogen dilution reduces deposition rate even though silane partial pressure and gas residence time stay the same. This observation supports hydrogen etching of the film during growth. Finally, the observed increase in deposition rate with gas phase diborane concentration is related to the known ability of diborane in cracking silane molecules.

As to the interpretation of the measured conductivities and activation energies, because of the two-phase nature of these films the in-plane measurements of these characteristics do not provide much useful information. However, it can be pointed out that measured activation energies of 0.07 eV are, within experimental errors, that of boron in silicon and, as such, confirm that in this respect silicon crystallites in the films behave like bulk silicon.

3.1.2.2 Effect of Hydrogen Dilution

A number of films were deposited at different levels of hydrogen dilution for four different CO_2 levels, with $b = 1.5x10^{-3}$. All other deposition parameters were the same as given in Table 6. The c-Si content in these films is given in Figure 24 for glass and SnO_2 substrates. The data show that while CO_2 levels in the discharge do not seem to have an effect on the c-Si content in the case of glass substrates, it does, however, control crystallinity of the films deposited on SnO_2 substrates. Also, as previously noted, increasing hydrogen dilution increases crystallinity and SnO_2 substrates give a lower c-Si fraction than glass substrates. The onset of crystallinity as a function of hydrogen dilution is also different for the two substrates, typically $h \leq 23$ for glass and $h \leq 50$ for SnO_2.

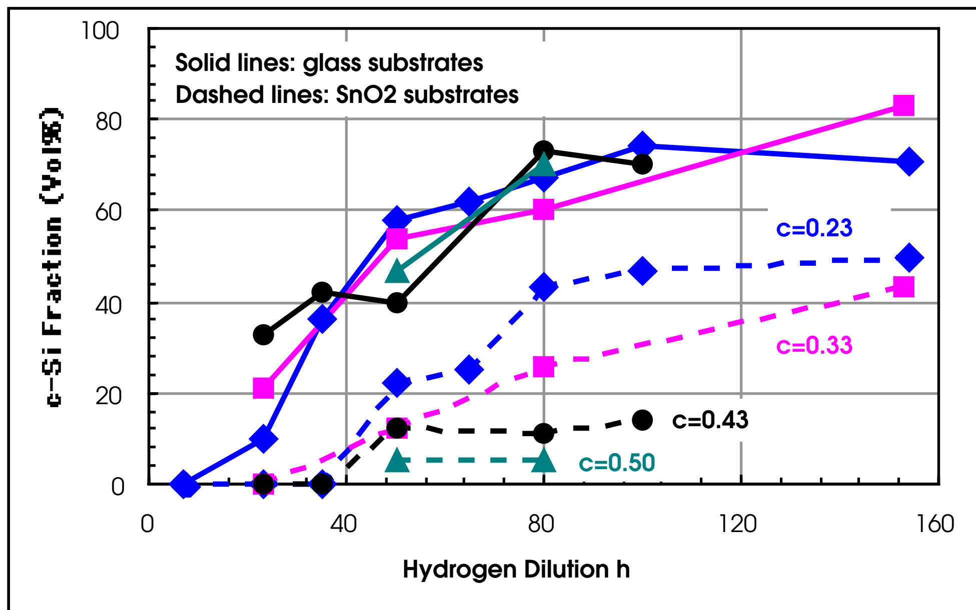

Figure 24. Volume fraction of c-Si as a function of hydrogen dilution for different levels of CO_2 in the discharge.

3.1.2.3 Crystallization in Ultra-thin Films

In order to characterize the structure of the films at thicknesses comparable to p-layer thicknesses in operational devices, we deposited 150 Å thick films and determined their crystallinity. In this case, two CO_2 levels of 0.33 and 0.5 were investigated with a hydrogen dilution of 50. Other deposition parameters were kept the same as before. Deposition times for these films were estimated from the deposition rates measured on thicker films on SnO_2 substrates prepared under

identical conditions. Raman analysis of the films showed that on SnO_2 coated substrates the films had all amorphous character.

On glass substrates, however, substantial crystalline fractions were observed for both CO_2 levels. Considering the fact that deposition rates on glass substrates are generally lower than on SnO_2, the data indicate that, on glass substrates, a c-Si phase forms at film thicknesses considerably less than 150Å. It can then be concluded that lack of crystallinity on SnO_2 coated substrates is not simply due to the small film thickness.

To substantiate this observation we deposited the same films on the same substrates but coated *in-situ* with a very thin (≈ 10 Å) SiO_x layer. Raman spectroscopic analysis of the films indicates the presence a c-Si phase in all cases. In the case of c = 0.43, numerical analysis of the data gives a c-Si volume fraction of 20% and 35%, respectively, for glass and SnO_2 substrates in c = 0.43. For c = 0.33, the analysis gives c-Si volume fractions of 44% and 34%, respectively, as shown in Figure 25. For both CO_2 dilutions we observed that deconvolution of the data gives smaller c-Si peak width for the films deposited on glass. This could possibly indicate that the SiO_x film thickness was thick enough to provide a base for c-Si nucleation but not thick enough to suppress totally the effect of the underlying substrate.

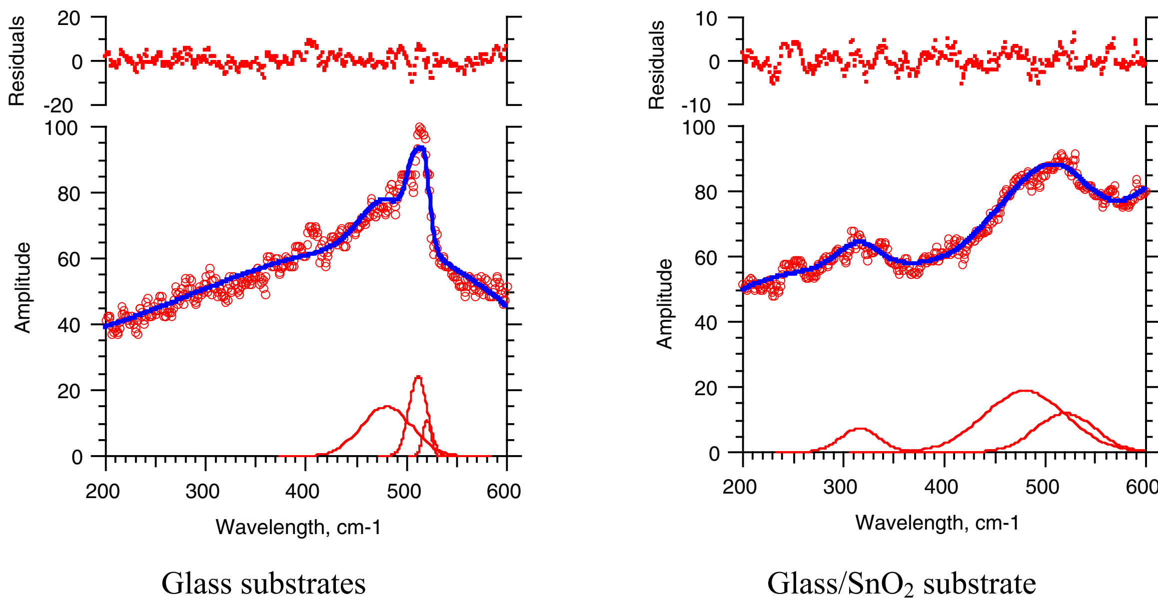

Glass substrates — Glass/SnO_2 substrate

Figure 25. Raman spectra of ultra-thin films (≈ 150Å) deposited on an interlayer of ≈ 10Å SiO_x.

3.1.3 Conclusion

In the present work we have demonstrated the deposition, by RF PECVD, of two phase films of B doped c-Si imbedded in a matrix of a-SiO_x:H:C for potential use as p-layers in a-Si:H based p-i-n solar cells. Structural and electrical properties of these films have been investigated as a function of SiH_4, CO_2 and B_2H_6 gas flows. Compositionally, the amorphous phase in the films

contains an order of magnitude more oxygen than carbon, insuring high transparency. Low power density used for the deposition coupled with presence of CO_2 and He buffer gas in the discharge lowers the risk of chemically reducing the conductive oxides, such as SnO_2, during the deposition. At low film thicknesses similar to the p-layers in the p-i-n devices, nucleation of c-Si phase requires ≈ 10Å thick SiO_x base layer which should be operationally benign in the solar cell.

3.2 Microcrystalline n-layers

The n-layers deposited from SiH_4, H_2 and CO_2 were investigated similar to the procedure described earlier for the p-layers, albeit less extensively. The dopant was PH_3 with the normalized flow given by $p = f(PH_3) / [f(SiH_4) + f(CO_2)]$. Substrate temperature was 175°C.

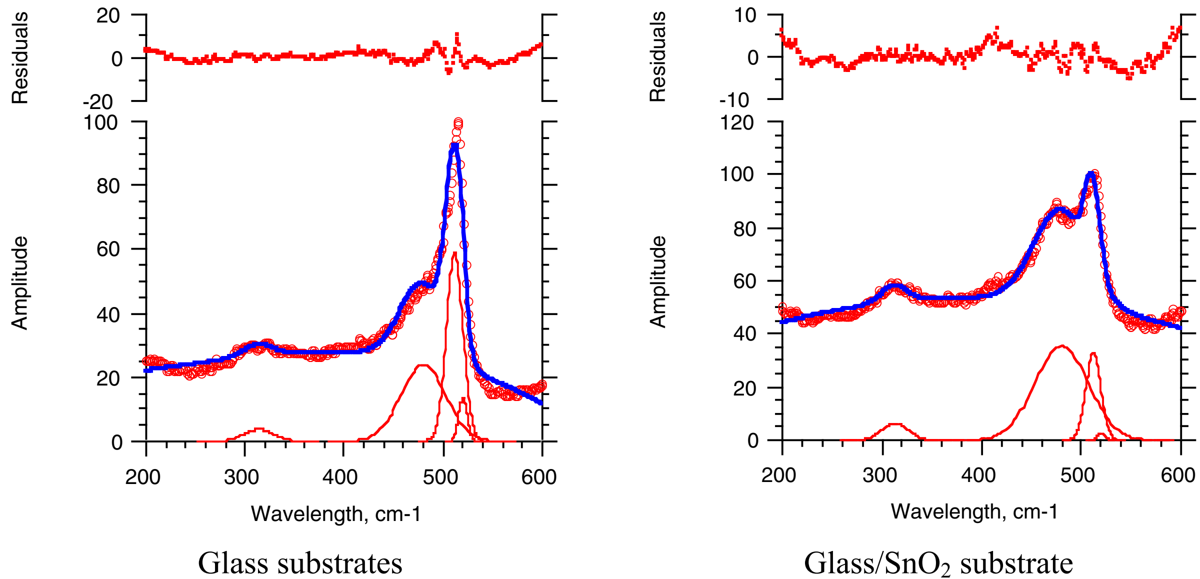

Glass substrates | Glass/SnO_2 substrate

Figure 26. Raman spectra of microcrystalline n-layers deposited from CO_2 containing discharge.

Raman spectra of Figure 26 illustrate the mixed crystalline/amorphous structure of the films deposited on glass and on SnO_2 coated glass for a deposition where the reduced parameters were: $f(SiH_4)$ = 2 sccm; Power Density = 420 mW/cm^2; Pressure = 1 Torr; h = 50; o = 0.43; $p = 10^{-2}$. The analysis gives c-Si volume fraction of 53% and 23% for glass and glass/SnO_2 substrates, respectively.

Characteristics of the films deposited at various CO_2 levels in the discharge for three different power densities are given below in Table 7. In these experiments total pressure, silane partial pressure, and hydrogen dilution were, respectively, 1 Torr, 9.9 mT and 50.

Table 7. Characteristics of the microcrystalline n-layer films deposited at various CO_2 levels in the discharge for three different power densities P_w.

Gas Flows (sccm)							P_w	Glass Substrate			SnO_2 Substrate	
SiH_4 (90%H_2)	CO_2	PH_3 (99.8% H_2)	H_2	He	p	c	(mW/cm^2)	R (Å/s)	σ_d (S/cm)	c-Si (Vol%)	R (Å/s)	c-Si (Vol%)
20	0	10	73	100	0.01	0	420	0.64	16	76	0.58	63
20	1	15	117	50	0.01	0.33	420	0.50	7	58	0.61	34
20	1.5	18	140	23	0.01	0.43	420	0.39	3	53	0.39	23
20	0	10	73	100	0.01	0	253	0.50	27	66	0.53	30
20	1	15	117	50	0.01	0.33	253	0.39	14	67	0.42	38
20	1.5	18	140	23	0.01	0.43	253	0.36	5	41	0.36	23
20	2	20	163	0	0.01	0.5	253	0.28	4	66	0.31	22
20	1	15	117	50	0.01	0.33	168	0.39	19	52	0.33	33
20	1.5	18	140	23	0.01	0.43	168	0.22	12	50	0.28	23
20	2	20	163	0	0.01	0.5	168	0.22	5	49	0.28	22

Comparing these results with the p-layer results, it is found that:

- the conductivities are significantly higher,
- c-Si volume fractions, both for glass and glass/SnO_2 substrates, are also higher,
- the differences in the deposition rates and in the c-Si volume fractions between glass and glass/SnO_2 substrates are smaller.

Higher discharge power densities favor the formation of the c-Si phase but the trend is not a strong one. For a given power, the c-Si volume fraction is weakly dependent on the CO_2 levels in the discharge.

The effect of the phosphine level in the discharge was estimated by comparing the film deposited at $P_w = 168$ mW/cm^2, c = 0.5, p = 0.01 to a film deposited under the same conditions but at p = 0.005. The film deposited at a lower phosphine level had similar properties except for the conductivity, which was measured to be 3 S/cm. It seems that, for this limited case, the effect of the phosphine in the discharge is limited to controlling the carrier concentration in the c-Si phase.

3.3 Characterization of the SnO_2/p and ZnO/p Contact Resistance and Junction Properties in a-Si p-i-n Solar Cells and Modules

This work was presented at the 28th IEEE Photovoltaic Specialists Conference (September 2000 in Anchorage, Alaska) and is contained in Appendix 1. A brief summary is given here.

A new method has been developed to characterize the TCO/p contact in a-Si p-i-n superstrate solar cells and modules. The method is applied to a series of devices fabricated at BP Solar on commercial SnO_2 and ZnO-coated SnO_2 having different p-layer recipes and pre-deposition treatments. Values of the contact resistance (R_C) of 1±0.5 Ω-cm^2 were found for a wide range of TCO and p-layer processing including ZnO. Temperature dependence of R_C gave barrier height of 40-55 meV. Analysis of devices with a thin ZnO layer on SnO_2 and with different

predeposition treatments indicates lower V_{oc} and FF observed with ZnO is not due to the contact but to changes in the p/i junction recombination. The solar cell performance is very sensitive to the ZnO surface treatment but R_C is not. No evidence was found for a blocking or high resistance ZnO/p contact.

3.4 Thin Si Films by HWCVD

This year, the focus of the project has shifted to the deposition of doped films. The goal as before is to determine the relationship between process parameters, particularly the dopant gas concentration, and the film properties. An initial target of 10 μm polycrystalline silicon films with a p-dopant (boron) content yielding a resistivity between 1-10 Ω-cm has been set. These target parameters correspond with film properties planned for subsequent devices. Because phosphorous presents a contamination problem due to adsorption and then persistent degassing of this species from the reactor surfaces, n-doping will be postponed for the time being. Preliminary experiments have yielded films with resistivities of 1-100 Ω-cm. More experiments are necessary to determine the quantitative relationship between the diborane to silane ratio and the film resistivity. However, since the film grain size continues to be 10-50 nm, it is uncertain if doped films of this nature could be suitable for device development.

Collaborations with Professor Ajeet Rohatgi at the Georgia Institute of Technology and Bhushan Sopori at NREL have been established to investigate various low temperature (<600 ^{o}C) techniques to enhance the grain size of thin silicon films. As previously reported, HWCVD films have a typical grain size of 10-50 nm. Such small grain size, compared to the film thickness required (~10 μm), leads inherently to a large number of grain boundaries and carrier recombination sites, thus limiting ultimate device performance. The general approach of both collaborations is to use metal induced crystallization to increase the grain size to 1-10 μm. However, the collaborators will use different techniques to crystallize or recrystallize the silicon films. Sopori, on the one hand, will use optically enhanced annealing to coalesce small grains in polycrystalline Si films; whereas, Rohatgi plans to recrystallize amorphous Si films by rapid thermal annealing. With this purpose, a series of intrinsic and boron-doped films were deposited by HWCVD on Al coated glass substrates. These samples were sent to the respective collaborators for subsequent post-treatment. The results of these experiments are expected in future reports.

We have also encountered a new issue related to deposition of relatively thick films (> 5 μm) on glass substrates. Polycrystalline Si films thicker than 5 μm appear to be under significant internal stress. This is evidenced by the formation of cracks and delamination of the films. This effect, however, is not observed on amorphous films of similar thickness. It is suspected that the stress may originate from the thermal expansion mismatch between the Si films and 7059 glass. Si films will be deposited on 1737 glass, which has thermal expansion properties closely matched to Si, to reduce the thermally induced stress in the films. Alternatively, roughening the surface of glass substrates by physical or chemical etching could help to disperse the film stress over many smaller areas.

Depositions in the HWCVD reactor were interrupted for a large portion of this year as a result of a series of equipment failures. At first, leaks developed in the bottom reactor flange and the load-lock chamber door. These problems were traced to the excessive thermal load to which these

seals are exposed. The reduction of unnecessary heating procedures and the use of air cooling has eliminated this problem. After this, the substrate plate magnetic transporter and, in turn, the reactor RGA became inoperative. In both cases, the failures resulted from silicon deposition over several years of operation. These units have been replaced and procedures have been adopted to minimize the exposure of these parts to silicon deposition.

Finally, the results of our work on the analysis and modeling of HWCVD are described in the manuscript of a poster presented at the 16th European Photovoltaic Solar Energy Conference and Exhibition, Glasgow, May 1-5, 2000. The paper, "Process Analysis and Modeling of Thin Silicon Film Deposition by Hot-Wire Chemical Vapor Deposition," is contained in Appendix 2.

4 CdTe-BASED SOLAR CELLS

4.1 Window Layer Development

4.1.1 Quantitative Model of CdTe/CdS Interdiffusion

In this section, a continuum method is presented for investigating the diffusion process for CdS into CdTe using measured x-ray diffraction line profiles, grain size distributions and grain boundary widths in CdTe/CdS couples. The approach, similar to that proposed by Houska [27], consists of determining sulfur distribution within geometrically simplified grains, partitioning the grains into discrete volume elements, and combining their volume fractional contributions to diffracted beam intensity, resulting in compositional broadening of the CdTe (511)/(333) line. The diffusion process was modeled for simultaneous diffusion from source into grain and grain boundary and volume diffusion from grain boundary into the grain. The two dimensional solution for parallel grain boundaries in a sample of finite thickness proposed by Gilmer and Farrell [28] for Type B kinetics was adopted. The critical characteristic of Type B kinetics is that the grain boundary spacing is sufficient to allow them to be treated as isolated from one another. Solutions were obtained for measured grain size distributions and initial estimates of bulk and grain boundary diffusion coefficients, and were transformed into three dimensions by using a cylindrical coordinate system.

Only diffusion of CdS into chemically pure CdTe, resulting in formation of a $CdTe_{1-x}S_x$ alloy, was considered. This is justified by the measured Te uptake in the CdS films, which is negligible when CdS is treated prior to CdTe deposition, or has large as-deposited grain size. The solubility limit in the CdTe-CdS alloy system was established from measured data for mixed $CdTe_{1-x}S_x$ films heat treated with $CdCl_2$:O_2:Ar vapor and was compiled into a provisional phase diagram over a wide range of temperatures. To model diffusion, $CdTe_{1-x}S_x$ alloy volume fractions, expressed as the molar composition, x, were calculated for incremental values of x within annular slabs of the model volume, or grain. The volume fractions at each discrete composition were summed and then transformed into an x-ray diffraction intensity line profile using the Pearson VII function with half-width at half-maximum and shape parameter values determined from annealed CdTe powder samples. The resulting profile was corrected for primary and diffracted beam extinction in overlying slabs. Unlike Auger or SIMS depth-profiling approaches, which consider average depth composition and are destructive to the sample, this approach considers discrete compositional elements and is non-destructive.

Modeled line profiles were refined by comparison with measured profiles, using only the bulk and grain boundary diffusion coefficients as fitting parameters. Measured profiles were obtained from CdS/CdTe/CuTe/Mo/glass structures, in which the grain size distribution remained constant over the entire treatment temperature and time range explored. Verification of the bulk coefficient was obtained by Auger depth profile analysis of treated CdS/CdTe couples using single crystal CdTe substrates.

4.1.1.1 Geometry

The surface morphology of physical vapor deposited films consists of densely packed hexagonal grains as shown in Figure 27. Cross-sectional analysis has shown that these grains extend continuously from the substrate to the surface. In modeling this grain configuration, we adopted a cylindrical coordinate system as depicted in Figure 28. Each grain is divided into annular and slab elements; in cylindrical coordinates, the ith volume element, V_i, is represented as an annulus within a slab having height, Δz:

$$V_i = \Delta z \pi \left[\left(\rho_i + \Delta \rho \right)^2 - \rho_i^2 \right], \text{ where } \rho \text{ is the radial coordinate.} \tag{7}$$

The volume fraction of the ith volume element, F_i, is:

$$F_i = \frac{V_i}{\Delta z \pi r^2}, \text{ where } r \text{ is the grain radius.} \tag{8}$$

In terms of the cylindrical geometry, this becomes:

$$F_i(\rho_i, \Delta\rho) = \frac{(\rho_i + \Delta\rho)^2 - \rho_i^2}{r^2}. \tag{9}$$

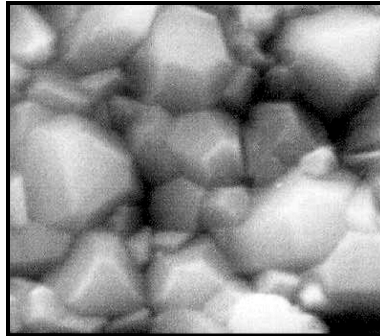

Figure 27. SEM of as-deposited evaporated CdTe film surface.

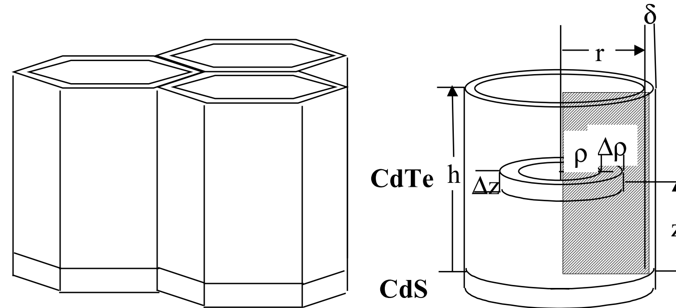

Figure 28. Hexagonal representation of grains and cylindrical geometry used to model diffusion.

4.1.1.2 Composition Due to Diffusion

For the nth slab, the composition of the ith radial element, $c_{i,n}$ is defined as the mid-point composition of the corresponding volume element:

$$c_{i,n}(\rho_i, z_n, t) \equiv c_g(\rho_i, z_n, t), \text{ where} \tag{10}$$

$$\rho_i \equiv \Delta\rho\left(i + \frac{1}{2}\right) \quad \text{and} \tag{11}$$

$$z_n \equiv \Delta z\left(n - \frac{1}{2}\right). \tag{12}$$

The three-dimensional model is based on the two-dimensional solution of the diffusion equation obtained by Gilmer and Farrell for a system in which the diffusing species has a limited solubility in the film and the diffusion coefficients are independent of concentration. The analytical solution found by Gilmer and Farrell applies to the following conditions: 1) isolated grain boundary; 2) constant diffusant source; 3) constant bulk and grain boundary diffusion coefficients, D and D_b; and 4) reflecting free surface. The two-dimensional solution was then transformed to three dimensions using the cylindrical symmetry.

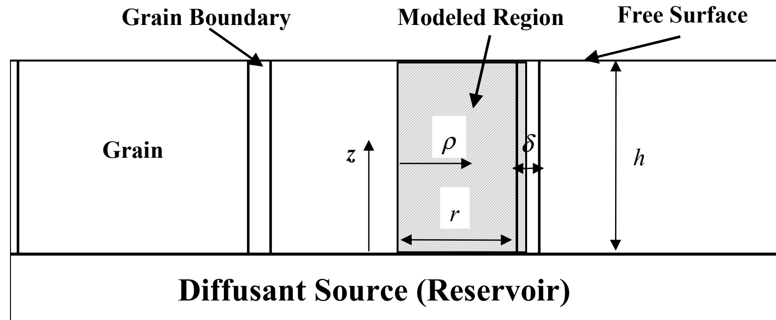

Figure 29. 2-D section through cylinder showing grain structure modeled by Gilmer and Farrell.

The two-dimensional coordinate system used by Gilmer and Farrell is shown in Figure 29. Within each grain, the concentration is assumed to obey the bulk diffusion equation:

$$D\nabla^2 c = \frac{\partial c}{\partial t}, 0 < \rho < (r - \delta/2). \tag{13}$$

The grain boundary concentration follows a similar equation, in the lateral dimension from $(r - \delta/2)$ to $(r + \delta/2)$. The concentration within the grain boundary was assumed to have a parabolic dependence in the ρ-direction. Subject to the constraints that the concentration in the film is zero at $t = 0$, Eq. 13 is satisfied by functions of the form:

$$F(\rho,z,t)=\sum_{n,m=1}^{\infty}A_{nm}Y_{nm}(\rho)Z_n(z)T_{nm}(t), \tag{14}$$

where Y_{nm} and Z_n are periodic functions in the r and z directions, respectively. The assumed parabolic dependence of concentration within the grain boundary leads to the boundary condition of the form:

$$(\Delta-1)\beta_n^2-\alpha_{nm}^2=\left(\frac{2\alpha_{nm}}{\delta}\right)\tan(\alpha_{nm}r),\text{ where} \tag{15}$$

$$\beta_n=\frac{\pi(2n-1)}{2h}\ , \tag{16}$$

$$\Delta=D_b/D, \tag{17}$$

where D and D_b are the bulk and grain boundary diffusion coefficients, respectively.

The parameter α_{nm} is solved by iteration of Eq. 15. The boundary condition needed to determine the function in Eq.14 is that which represents the physical situation at the surface of the film, at coordinate h in z. In the present case, we consider that the free surface "reflects" diffusant in the z-direction. In this case, the incremental composition, c_g at coordinate ρ,z and time, t, is thus:

$$c_g(\rho,z,t)=c_0\left[1-\sum_{n=1}^{\infty}\sum_{m=1}^{\infty}A_{nm}Y_{nm}(\rho)Z_n(z)T_{nm}(t)\right], \tag{18}$$

where Y_{nm}, Z_n , T_{nm} and A_{nm} are

$$Y_{nm}=\cos(\alpha_{nm}\rho) \tag{19}$$

$$Z_n=\sin(\beta_n z) \tag{20}$$

$$T_{nm}=\exp\left[-Dt\left(\alpha_{nm}^2+\beta_n^2\right)\right] \tag{21}$$

$$A_{nm}=\frac{\dfrac{8}{\alpha_{nm}r}\sin(\alpha_{nm}r)+\dfrac{4\delta}{r}\cos(\alpha_{nm}r)}{(2n-1)\pi\left(1+\dfrac{\sin(2\alpha_{nm}r)}{2\alpha_{nm}r}+\dfrac{\delta}{r}\cos^2(\alpha_{nm}r)\right)}. \tag{22}$$

4.1.1.3 Diffraction Profile from Spatial Composition Distribution

Within each slab, the incremental composition, c_i, of a particular volume element was transformed to Bragg angle, θ_i, for a given reflection, *(hkl)*, by the Vegard relation for the CdTe-CdS system [29]:

$$\theta_i = \arcsin\left[\frac{n\lambda\sqrt{h^2+k^2+l^2}}{2\left(6.481-\frac{c_i}{1.508}\right)}\right]. \tag{23}$$

This represents the compositional broadening of the *(hkl)* line in question. The differential power, dP_θ, diffracted from a volume element at the particular composition, or angle, in a thin homogeneous sample can be approximated in terms of the structure factor, F_{hkl}, and the differential volume, dV:

$$dP_\theta \propto F_{hkl}\frac{\left(1+\cos^2\theta_{hkl}\right)}{\sin\theta_{hkl}\cos\theta_{hkl}}dV. \tag{24}$$

The compositional broadening in 2θ due to formation of $CdTe_{1-x}S_x$ alloy in the temperature range considered is less than 1 degree. Thus, in modeling diffraction line profiles, the angular dependence of the structure factor was not considered. In this case, the differential power diffracted from a volume element is linearly proportional to its volume fraction. Within each nth slab, the volume fraction of the incremental composition, dP_θ, contributes to diffracted intensity, or composition function, $g_n(\theta_i)$:

$$g_n(\theta_i) = \sum dP_\theta. \tag{25}$$

A line profile, $h_n(\theta_i)$, is obtained through the convolution integral of the composition function, $g_n(\theta_i)$, and the instrument function, $f_n(\theta_i)$:

$$h_n(\theta_i) = \int_{\theta_1}^{\theta_2} g_n(\theta_i) f_n(\theta_i) d\theta, \tag{26}$$

A Pearson VII function was used to simulate the diffractometer instrument intensity function [30]:

$$f = f_b + f_0\left[1+\frac{\left(2^{\frac{1}{m}}-1\right)x^2}{H^2}\right]^{-m}, \tag{27}$$

where x is the angular deviation from the peak centrum, H is the half-width at half-maximum, and m is the shape parameter. In this function, $m = 1$ defines the Cauchy function while $m = \infty$ defines the Gaussian function. The (511)/(333) line profile of annealed CdTe powder with

nominally 100 to 500 μm particle size yielded a diffractometer instrument function with $m = 3$ and $H = 0.06°$.

The intensity function for a given slab was corrected for primary and diffracted beam extinction in the overlying layers according to:

$$h_n(\theta, z_n) = \exp[-2\mu_m z_n / \sin(\theta)] \int_{\theta_1}^{\theta_2} g_n(\theta) f_n(\theta) d\theta, \tag{28}$$

where μ_m is the x-ray mass absorption coefficient of the overlying medium at the measurement x-ray energy employed. In this treatment, the value of μ_m varies negligibly over the $CdTe_{1-x}S_x$ compositional range, so the value for CdTe at 8 keV was taken for Cu-kα x-rays:

$$\mu_{CdTe}(8keV) = 0.1587 \mu m^{-1}. \tag{29}$$

4.1.1.4 Solubility Limit Determination

Accurate modeling of the $CdTe_{1-x}S_x$ alloy line profiles at different temperatures requires the alloy system equilibrium solubility limits. The solubility limits of the CdTe-CdS system were established by x-ray diffraction determination of $CdTe_{1-x}S_x$ and $CdS_{1-y}Te_y$ alloy lattice parameters in *mixed* CdTe-CdS films after thermal treatment in $CdCl_2$:O_2:Ar vapor from 420°C to 625°C. The mixed films were evaporated from CdS and CdTe powders, forming meta-stable alloys with mid-range composition ~$CdTe_{0.5}S_{0.5}$. Heat treatment of these films in $CdCl_2$:O_2:Ar vapor resulted in phase segregation into two alloy components at each side of the CdTe-CdS equilibrium miscibility gap [31]. To ensure that end-point compositions were reached at each temperature, the treatment time was extended until the measured change in alloy compositions were less than the detection limit, which, for x and y, is ~0.0001. X-ray diffraction scans were taken over the 2θ range from 20° to 91°, sampling nine *(hkl)* reflections. The individual lattice parameters for each *(hkl)* were reduced to a precision lattice parameter, a_o, by extrapolation on a plot of a_o versus Nelson-Riley-Sinclair-Taylor function [32]. CdS weight fraction, x, in zincblende $CdTe_{1-x}S_x$ and CdTe weight fraction, y, in wurtzite $CdS_{1-y}Te_y$ were calculated from the precision lattice parameter using Eqs. 30 and 31.

$$x = 1.508(6.481 - a_o) \text{ and} \tag{30}$$

$$y = 1.508(a_o - 4.136). \tag{31}$$

The degree and rate of mixing in the CdTe-CdS binary couple are governed by thermodynamic equilibria and interdiffusion kinetics, respectively, of the CdTe-CdS system. While the endpoint compositions of interdiffusion depend on thermodynamic equilibrium, the kinetic processes of diffusion depend on the geometry and chemical state of the structure. We considered the thermodynamical aspects of the CdTe-CdS system, to establish the solubility limits and mixing energies of S in CdTe and Te in CdS in the temperature range normally used to fabricate high efficiency CdTe/CdS solar cells.

Previous works have established the *T-x* phase relations in CdTe-CdS mixed crystals at temperatures above 625°C, which exceeds the temperatures typically used to deposit and process thin-film CdTe/CdS structures [33,34]. For mixed crystal films formed at lower temperatures, from 120°C to 200°C, a continuous range of alloys can be obtained [31,33,35,36,37]. For the mixed films, heating above ~300°C induces phase segregation in accordance with the existence of the equilibrium miscibility gap found in mixed CdTe-CdS crystals at higher temperature, indicating that single phase films with composition lying within the miscibility gap are deposited in a metastable state. The segregated films exist in two crystallographic forms: zincblende (F-43m) structure on the Te-rich side and wurtzite ($P6_3mc$) structure on the S rich side [38].

The rate of transformation from metastable to equilibrium states is increased at low temperatures by treatment in vapor ambient containing $CdCl_2$ and O_2. The addition of these chemical species at relatively low levels does not measurably shift the solubility limits of the CdTe-CdS system in the 650°C to 700°C range. Thus, metastable mixed films having composition in the miscibility gap were used to determine the low temperature solubility limits.

Single phase $CdTe_{1-x}S_x$ films deposited at 250°C to 300°C with x ~ 0.4 were heat treated in $CdCl_2$ and O_2 containing vapor to induce phase segregation. X-ray diffraction was used to determine the composition of the segregated phases by measuring d-spacing of multiple lattice plane reflections, determining the lattice parameter, and determining composition by assuming a linear relation between composition and lattice parameter. Treatment was carried out until no detectable change in lattice parameter between consecutive treatments was found. The precision lattice parameters, $CdTe_{1-x}S_x$ and $CdS_{1-y}Te_y$ of the final compositions, were taken to represent the equilibrium compositions at the temperature used to treat the films. To simplify conventions, all alloys will be expressed in terms of x in $CdTe_{1-x}S_x$, so that x in Te-rich alloy is x_1 and x in S-rich alloy is x_2.

The CdTe-CdS system was modeled using solution thermodynamics – that is, using mixing free energies as opposed to reaction free energies. This is the typical approach used to model alloy systems, and the non-ideality of the system is expressed as excess enthalpy and excess entropy of mixing [39]. The excess enthalpy ($\Delta\underline{H}^{EX}$) and excess entropy ($\Delta\underline{S}^{EX}$) of mixing are regressed parameters that fit the model behavior to the experimentally determined solubility data.

$CdTe_{1-x}S_x$ film 2 microns thick were evaporated at 250°C on Corning code 7059 glass coated with 200 nm of indium-tin-oxide, In_2O_3:Sn (ITO). The ITO facilitated adhesion of the films and served as an internal standard for x-ray diffraction analysis. CdTe and CdS were co-evaporated from separate boron nitride effusion sources onto the radiatively heated substrates at a growth rate of ~8 Å/sec using 99.999% pure CdTe and CdS powders. Films with composition x from 0.4 to 0.5 were obtained by depositing the CdTe and CdS an effusion rate ratio, $r_{CdS}/r_{CdTe} = 1.5$, which was needed to overcome the lower sticking coefficient of CdS. For the source configuration used, this corresponded to source temperatures, T_{CdS} = 900°C and T_{CdTe} = 760°C.

Treatment of the $CdTe_{1-x}S_x$ films in $CdCl_2$:Ar:O_2 vapor was carried out in a reactor allowing independent control of treatment temperature and $CdCl_2$ and O_2 partial pressures. $CdCl_2$ vapor was generated from a sintered powder $CdCl_2$ source supported in graphite susceptors within a quartz reactor heated externally by FCM lamps in linear housings. A mica mask was used as both a separator and radiative/thermal insulator between the source susceptor and the thin film

sample. A second graphite susceptor rested on top of the thin film sample to provide independent heating control.

The independent temperature control was necessary to fix vapor ambient concentrations for different reaction temperatures. The $CdCl_2$ source was maintained at 400°C, which produces a $CdCl_2$ partial pressure of approximately 3 x 10^{-3} Torr, or concentration of 8 x 10^{-5} µmol/cm^3 at the film surface. Heating times were measured for samples and $CdCl_2$ susceptor. Using a CdTe/CdS/ITO/glass sample with an embedded microthermocouple, the time needed to heat the sample to 400°C was 40 seconds. The time to heat the $CdCl_2$ susceptor to 400°C was measured to be 20 seconds. The characteristic diffusion time for $CdCl_2$ vapor in this apparatus was estimated for $CdCl_2$ in Ar, treating the $CdCl_2$ as a polar diffusing species, yielding a time constant of ~2 sec at 400°C. Thus, the heat-up rate of the susceptors, not the characteristic diffusion times, controls the time to reach equilibrium in the reaction zone. Oxygen partial pressure was fixed at ~120 Torr by flow rate control. All treatments were conducted in flowing $Ar:O_2$ at a total flow rate of 0.94 l/m at atmospheric pressure. Prior to each treatment, the system was pumped to < 50 mTorr prior to back-filling with Ar and O_2. This procedure established a maximum residual H_2O partial pressure of < 5 mTorr. To maximize phase segregation rate, the sample and $CdCl_2$ sources were heated in unison. On cool down, $CdCl_2$ condensation on the $CdTe_{1-x}S_x$ films was prevented by cooling the $CdTe_{1-x}S_x$ films ~60 sec prior to cooling the $CdCl_2$.

The film compositions were analyzed by energy dispersive x-ray spectroscopy (EDS) and wide angle x-ray diffraction (XRD). EDS was carried out at 20 kV using an EDAX PV9800 system with an Amray 1810T scanning electron microscope. XRD was measured using a Philips/Norelco powder diffractometer with Cu-k_α radiation and Bragg-Brentano focusing geometry. The primary information obtained was lattice parameter, a_{hkl}, for each observed reflection, d_{hkl}, $a_{hkl} = d_{hkl}\sqrt{h^2 + k^2 + l^2}$, where *h*, *k*, and *l* are the Miller indices of a given reflection. The set of observed lattice parameters were reduced to a precision lattice parameter, a_f, by extrapolation on a plot of a_{hkl} versus the Nelson-Riley-Sinclair-Taylor function (NRST) to the function's zero point; $F_{NRST} = 0.5[(\cos^2\theta/\sin\theta)+(\cos^2\theta/\theta)]$, where θ is the Bragg angle of the peak centrum. The alloy composition, x, was determined using, $x = 1.508(a_o - a_f)$, where x = [CdS]/[CdS]+[CdTe] in $CdTe_{1-x}S_x$ and a_O = lattice parameter of pure CdTe = 6.481Å [ICDD Database]. Narrow-angle x-ray diffraction scans of high order (*hkl*) reflections such as (511/333) and (531) were made to verify that a single composition had been reached after treatment on the basis of symmetrical peak shape. All diffraction patterns and profiles were stripped of α_2 components using the Rachinger correction prior to analysis [40].

4.1.1.5 Results of Heat Treatment of $CdTe_{0.5}S_{0.5}$ Films

The x-ray diffraction pattern of a $CdTe_{0.6}S_{0.4}$ film on ITO/7059 glass before and $CdCl_2:Ar:O_2$ vapor treatment at 415°C is shown in Figure 30. Before treatment, the film exhibits strong preferential orientation, with few other peaks, making detailed XRD analysis inaccurate. Thus, for as-deposited alloy films, EDS was used to establish the composition, and XRD was used to confirm the single phase nature of that composition.

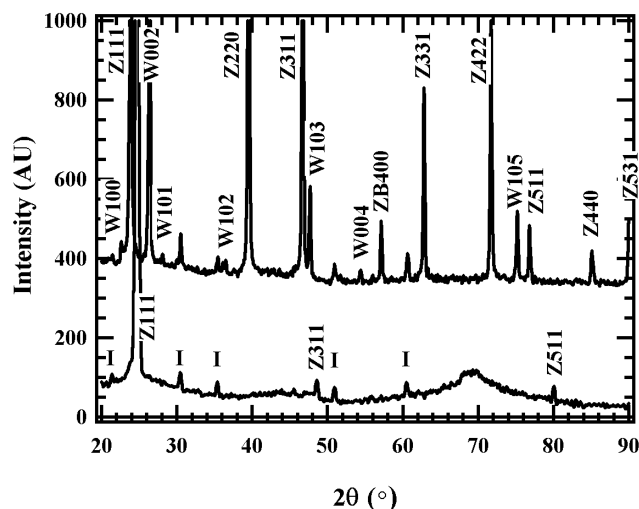

Figure 30. XRD patterns for $CdTe_{0.6}S_{0.4}$ as deposited (lower) and after treatment at 415°C in $CdCl_2$:Ar:O_2 for 60 minutes. ITO substrate is indicated by "I". Zincblende and wurtzite phases and corresponding (hkl) are indicated by "Z" and "W", respectively.

Upon heat treatment, two phases are detected, each exhibiting multiple (hkl) reflections, indicating randomization of grain orientation with respect to the substrate. The NRST plots for this film for the zincblende and wurtzite components are shown in Figure 31. For each phase, the lattice parameters derived from each reflection fell onto a straight line on the NRST plots, indicating that the treated films are free of any orientation-specific perturbations such as strain. Similar results were obtained at the higher temperatures.

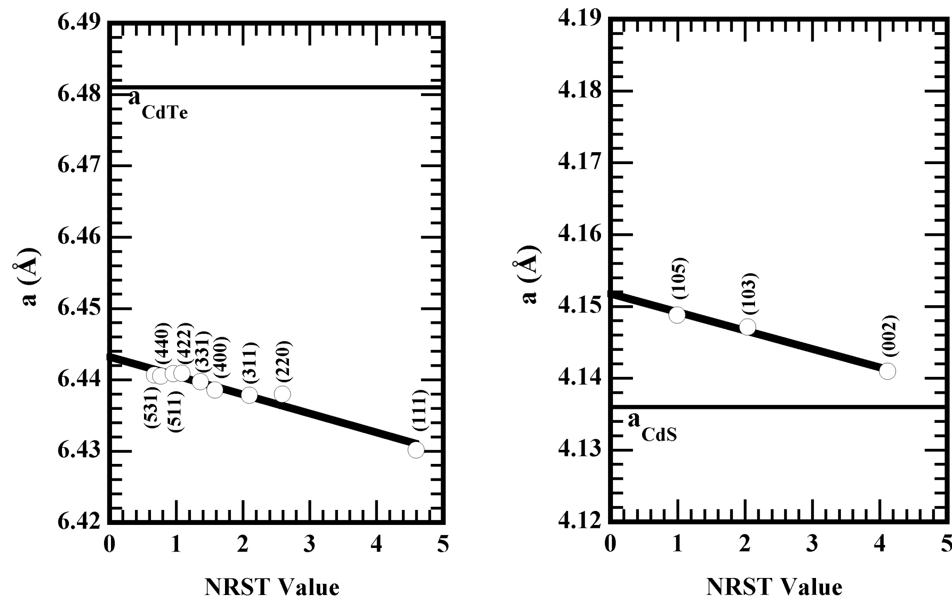

Figure 31. Lattice parameter versus NRST function value for zincblende and wurtzite phases of film shown in Figure 27 for $CdTe_{0.6}S_{0.4}$ after treatment. Horizontal lines indicate the lattice parameter values for pure CdTe and CdS.

The final compositions of zincblende and wurtzite phases for 415°C, 525°C and 625°C are shown in Table 8, including data for a sample treated at 625°C in argon ambient. In this case, the compositions are identical to those determined for the sample treated in $CdCl_2$:Ar:O_2 ambient, demonstrating the purely kinetic-enhancing role of the $CdCl_2$ and O_2 species. The data of Table 8 are graphically represented in a pseudobinary phase diagram (Figure 32), overlaid with published data points. The miscibility gap is bounded by asymmetrical solubility limit functions. The values obtained at 625°C coincide with those measured by Moon, et. al. [41] for the system without $CdCl_2$:O_2:Ar, indicating that these vapor species do not affect the end-point equilibrium compositions.

Table 8. Summary of final compositions for three treatment temperatures, and approximate time needed to reach equilibrium for fixed $CdCl_2$ and O_2 concentrations. Values of x and y correspond to $CdTe_{1-x}S_x$ and $CdS_{1-y}Te_y$, respectively.

T (°C)	Ambient	Time (min)	x ± 0.003	y ± 0.005
415	$CdCl_2$:Ar:O_2	60	0.058	0.03
525	$CdCl_2$:Ar:O_2	30	0.095	0.07
625	$CdCl_2$:Ar:O_2	10	0.140	0.10
625	Ar	40	0.140	0.10

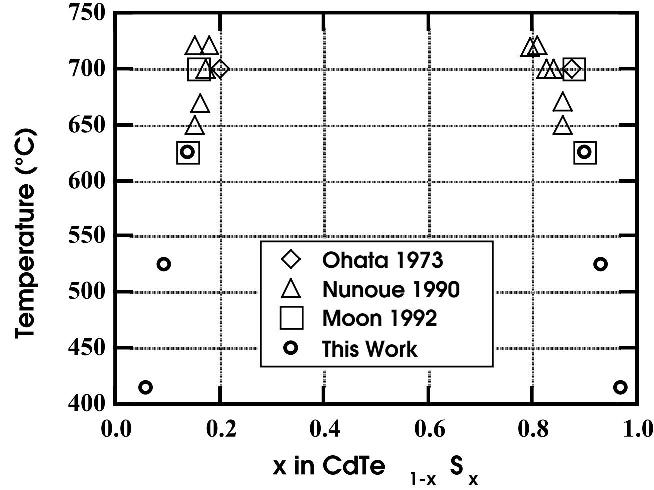

Figure 32. CdTe-CdS pseudobinary phase diagram with data of present work and others. Values at ~420ºC were established by Jensen, et al [47].

4.1.1.6 Miscibility Gap Modeling

The starting point in mixture analysis is the free energy of the system as a function of the molar quantities of it components. The derivative is then taken with respect to one of the components to determine how the free energy changes as the component is added to the mixture. This derivative is referred to as the partial molar free energy. The equilibrium condition is that the partial molar free energy of each component is equal in all phases. The total free energy for a phase containing two components is:

$$G^{mix} = N_1\underline{G}_1 + N_2\underline{G}_2 + RT\left[N_1 \ln x_1 + N_2 \ln x_2\right] + \left(N_1 + N_2\right)\Delta\underline{G}_{mix}^{EX} \qquad (32)$$

where an underbar denotes a molar free energy. The first two terms are the pure species free energies – that is, the independent free energies of the components before mixing. The second term is the standard entropy of mixing. This term is applicable to all mixtures, ideal and non-ideal. The last term quantifies the departure from ideality, and is called the excess free energy of mixing. All of the non-ideal behavior of the mixture is contained in this term, which can be a function of temperature and composition.

The molar excess free energy of mixing is typically expressed in the form:

$$\Delta\underline{G}_{mix}^{EX} = \Omega x_1 x_2 \qquad (33)$$

where

$$\Omega = \Delta\underline{H}^{EX} - T\Delta\underline{S}^{EX} \quad . \qquad (34)$$

The excess enthalpy ($\Delta\underline{H}^{EX}$) and excess entropy ($\Delta\underline{S}^{EX}$) of mixing are regressed parameters, which fit the model behavior to the experimental data. It is difficult to say whether these

parameters contain any sort of physical significance, though they are based on fundamental thermodynamic principles. The excess enthalpy and entropy can also be modeled as being composition dependent.

Determining the partial molar free energies from Eq. 32 first involves rewriting the x_i's as $N_i/(N_1 + N_2)$, then differentiating, with the result:

$$\underline{\mu}_1 = \frac{\partial G^{mix}}{\partial N_1} = \underline{G}_1 + RT \ln x_1 + \Omega x_2^{\,2} \ . \tag{35}$$

Then by symmetry,

$$\underline{\mu}_2 = \frac{\partial G^{mix}}{\partial N_2} = \underline{G}_2 + RT \ln x_2 + \Omega x_1^{\,2} \ . \tag{36}$$

The condition for 2-component, 2-phase equilibrium is:

$$\underline{\mu}_1^{\,I} = \underline{\mu}_1^{\,II} \tag{37}$$

$$\underline{\mu}_2^{\,I} = \underline{\mu}_2^{\,II} \tag{38}$$

where the phase is denoted by the Roman numeral superscript. For the CdS/CdTe system, Eq. 37 states that the partial molar free energy of CdS (1) in the CdS-rich phase (I) is equal to the partial molar free energy of CdS in the CdTe-rich phase (II).

Making Equations 29 and 30 phase-specific and substituting into Equations 31 and 32 yields:

$$RT \ln x_1^{\,I} + \Omega^I (x_2^{\,I})^2 = RT \ln x_1^{\,II} + \Omega^{II} (x_2^{\,II})^2 \tag{39}$$

$$RT \ln x_2^{\,I} + \Omega^I (x_1^{\,I})^2 = RT \ln x_2^{\,II} + \Omega^{II} (x_1^{\,II})^2 \tag{40}$$

These equations are linear with respect to Ω^I and Ω^{II}, and are simultaneously solved for Ω^I and Ω^{II} at each (x_1, x_2, T) data point. This then allows the 2-parameter regression of $\Delta\underline{H}^{EX}$ and $\Delta\underline{S}^{EX}$ from the experimental data. Examination of the equation indicates that Ω is much more sensitive to the concentration of the dilute species due to the logarithmic dependence of the numerator (the denominator is roughly unity). That is, a change in the dilute species from 1% to 0.1% has a much, much greater effect on Ω than a change of 99% to 99.9% of the predominant species.

4.1.1.7 Parameter Regression

The miscibility gap data in Table 9 were used to calculate Ω as a function of temperature and composition. Plots of Ω^I and Ω^{II} are shown in Figure 7. (**Note**: *T is evaluated in K, not ºC, for thermodynamic calculations, as always*.)

Table 9. CdS/CdTe solubility limits and calculated departure from ideal behavior.

Temperature, (ºC)	x_1^I	x_1^{II}	x_2^I	x_2^{II}	Ω^I, J/mol	Ω^{II}, J/mol
415	0.97	0.058	0.03	0.942	21024	18183
525	0.93	0.095	0.07	0.905	19831	18602
625	0.9	0.14	0.1	0.86	20298	19061
700	0.84	0.165	0.16	0.835	19702	19609

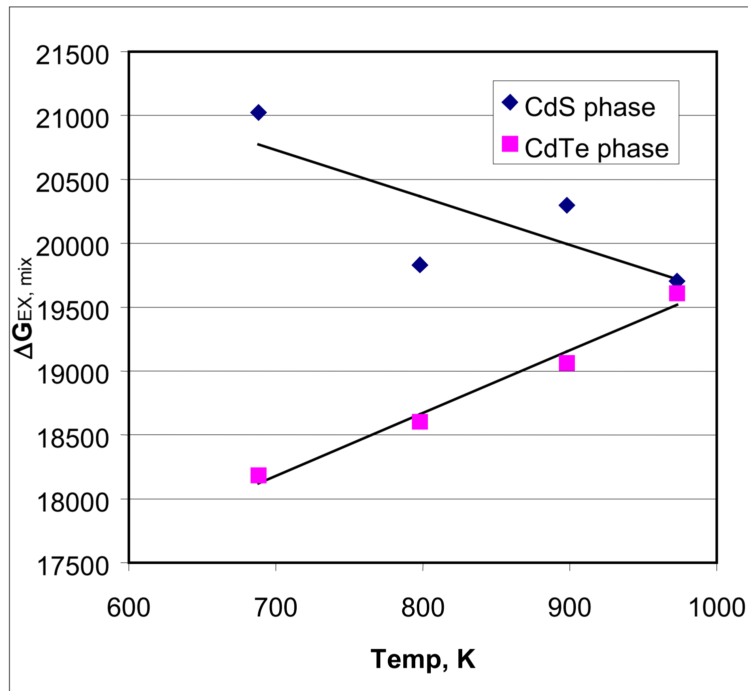

Figure 33. Excess free energies of mixing for CdS/CdTe system.

Recalling Eq. 34, it is apparent that a linear fit for Ω as a function of temperature would appear to work well for either Ω^I or Ω^{II}. Note that the stray point in Ω^I at 525ºC is likely due to experimental error – changing the data point from $x_2^I = 0.07$ to 0.06 brings it in line with the other three. This illustrates the high sensitivity to slight changes in the measured dilute-species concentration. The values obtained by the linear regression are:

$\Delta \underline{H}^{EX,I}$ 23325 J/mol

$\Delta \underline{H}^{EX,II}$ 14750 J/mol

$\Delta \underline{S}^{EX,I}$ 3.71 J/mol/K

$\Delta \underline{S}^{EX,II}$ -4.90 J/mol/K

The drawback to the above modeling approach is that a closed form solution for x_1^{II} and x_2^{I} is not possible. It is therefore not suitable as a correlation. For expediency, it is appropriate to fit a simple polynomial to the calculated curves. For CdS in CdTe, this is well approximated by a cubic fit:

$$x_1{}^{II} = (-0.01490) + (1.207e-4)T + (3.940e-8)T^2 + (2.393e-10)T^3 \quad (41)$$

$$x_2{}^{I} = (-1.490e-1) + (9.386e-4)T + (-1.940e-6)T^2 + (1.750e-9)T^3 \quad (42)$$

where T is in ºC. The regression was performed for the range 400-700 ºC. The data, model, and empirical fits are shown in Figure 34 and Figure 35. The empirical fit is in excellent agreement with the calculated solubility curves over the regression range.

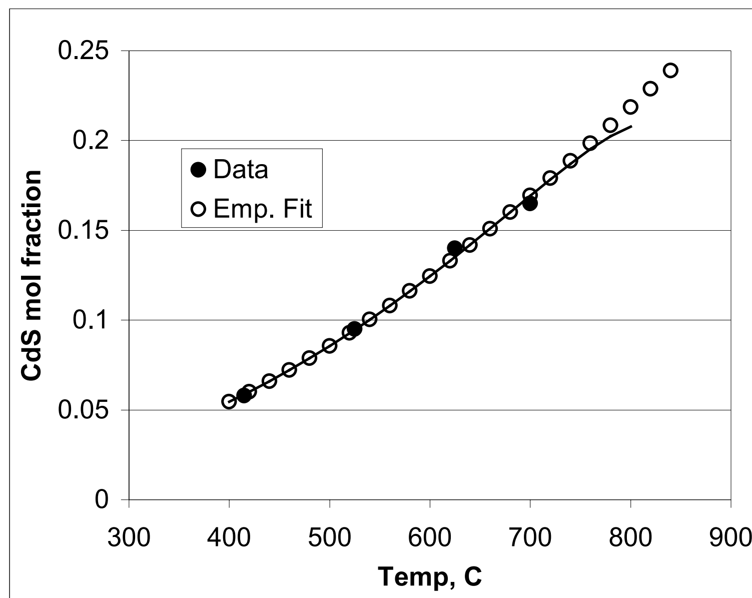

Figure 34. Solubility of CdS in CdTe-rich phase. Solid line is the thermodynamic model prediction.

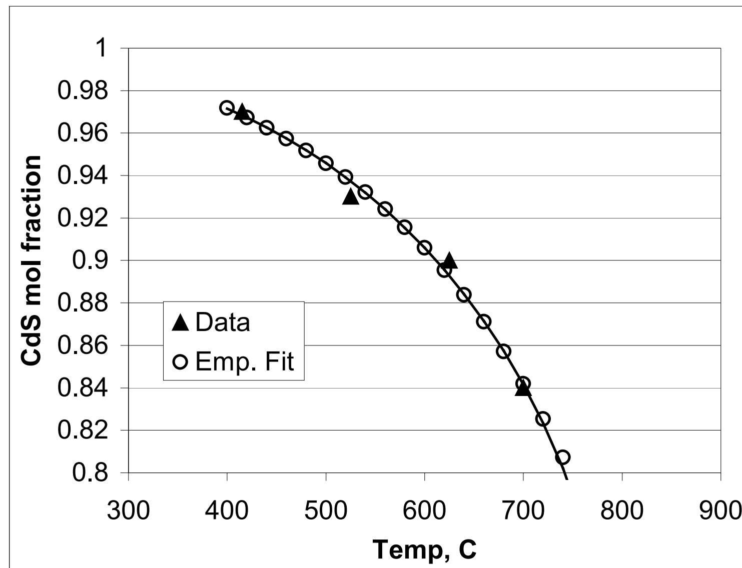

Figure 35. Solubility of CdTe in CdS-rich phase. Solid line is the thermodynamic model prediction. The values correspond to y = 1-x in Figure 32.

4.1.1.8 Sample Preparation for Diffusion Studies

Thin-film CdTe/CdS structures were fabricated in substrate configuration on Corning 7059 glass coated with a 1 μm thick film of molybdenum and a 100 nm thick film of CuTe. CdTe films 4.5 μm thick were deposited by thermal evaporation at 250°C onto the substrate at 3 nm/s from 99.999% purity CdTe powder. Undoped (111)-oriented CdTe single crystal wafers obtained from Keystone Crystal Corporation were also used as substrates, for Auger electron depth profile measurements of sulfur concentration after treatment. In all cases, CdS films from 200 nm to 220 nm thick were deposited at 220°C by thermal evaporation at 0.3 nm/s from 99.999% purity CdS powder. Superstrate thin-film CdTe/CdS structures were fabricated on Corning 7059 glass coated with 200 nm ITO under the same deposition conditions as above.

4.1.1.9 Vapor Treatment

All CdTe/CdS structures were vapor-treated in $CdCl_2$:O_2:Ar in a 6 cm diameter tubular reactor configured to deliver $CdCl_2$ vapor at a fixed concentration for different reaction temperatures, from 380°C to 480°C for 0.5 to 40 minutes [42]. Oxygen concentration was maintained at a partial pressure of ~130 Torr by adjusting volume flow rate with argon balance, maintaining a constant total flow of 1.0 l/m through the reaction zone. $CdCl_2$ vapor was generated from a sintered powder source contained in a graphite susceptor within 1 mm of the CdTe surface. $CdCl_2$ partial pressure was maintained at ~10 mTorr by controlling the $CdCl_2$ susceptor temperature at ~415°C. At a total pressure of 1 atmosphere, transport of $CdCl_2$ vapor to the sample surface is diffusion limited, with a time constant of ~0.2 seconds, which is sufficiently small with respect to treatment time to allow equilibrium to be maintained with respect to $CdCl_2$ vapor [42].

Prior to each treatment, the assembly containing the $CdCl_2$ source and CdTe/CdS structures was baked in vacuum at 250°C for 15 minutes to dehydrate the $CdCl_2$ and the surface of the CdTe. From this temperature, the treatment temperature at the substrate surface was attained in ~30 seconds. Cool-down rates of ~200°C per minute were achieved by shutting off power to the heating lamps.

4.1.1.10 Specimen Analysis

The film surfaces were examined by scanning electron microscopy (SEM) using an Amray 1810T microscope at 30 kV and by atomic force microscopy (AFM) using a Digital Instruments Dimension 3100 microscope in tapping mode. Grain radii, defined as the mean lateral half-dimension of clearly delineated grains, were determined from micrographs taken at three different positions on each film sample. Grain radii varied and were categorized in 0.5 μm intervals from 0 to 2 μm, sampling >300 grains. This data was used to generate a frequency distribution for each grain size interval. Grain boundary widths were estimated from cross-sectional transmission electron micrographs of CdTe/CdS thin-film structures deposited on Si single crystals.

X-ray diffraction (XRD) scans of the films were performed using a Philips/Norelco Bragg-Brentano focusing diffractometer with Cu-kα radiation at 35kV. Line profiles of the $CdTe_{1-x}S_x$ (511)/(333) reflection were acquired by step scanning in 0.02° intervals from 76.0 to77.0° in 2θ. An instrument function for pure CdTe was obtained using an annealed CdTe powder sample and yielded a half-width at half-maximum, H, of 0.06°. X-ray diffraction data was smoothed, and the $k\alpha_2$ component was stripped using the Rachinger correction. For quantitative comparison purposes, the background intensity was removed, and the resulting profiles were normalized to the area of the untreated (511)/(333) reflection.

Auger electron depth profiles of sulfur concentration were obtained from single crystal substrates at different temperatures to provide independent values of bulk diffusion coefficient for comparison with values obtained by the modeling of x-ray diffraction line profiles. The diffusion coefficient was calculated from the data using the solution for diffusion into an infinite medium with a constant surface concentration [43].

4.1.1.11 Grain Size Distribution

The grain size distribution used to model line profiles of substrate configuration films is shown in Figure 36. The measured distribution was converted to the volume fractional contribution in 10 grain size intervals. For each treatment time, the diffusion model was calculated for the corresponding volume fraction of each interval. These contributions to the compositional profiles were summed to produce the composite result. The functional form of the grain size distribution differs from a log-normal distribution for the mean grain size of this grain population. From volume fractional considerations, the peak in the grain size distribution does not represent the actual contribution of each grain size to diffracted intensity, which can lead to skewing of the final compositional profile. For the model, over-estimating the grain radius, r, reduces the grain boundary contribution and skews the compositional result toward lower sulfur concentration. Conversely, under-estimating grain radius amplifies the grain boundary diffusion contribution, skewing the compositional result toward high concentration.

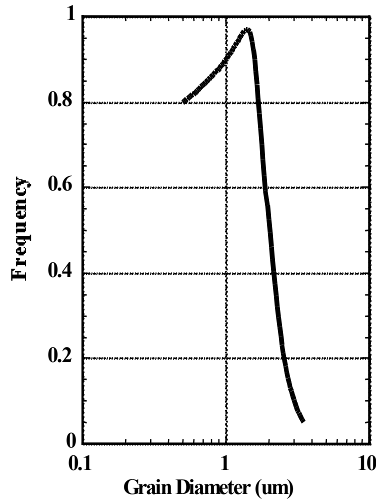

Figure 36. Grain size distribution to model diffusion of CdS into CdTe thin films.

4.1.1.12 Measured and Modeled XRD Line Profiles

The measured diffraction line profiles for substrate configuration films before treatment and for 10, 20 and 40 minutes' treatment at 440°C are shown in Figure 37. The profile evolution from 10 to 40 minutes is characterized by continuous transformation of pure CdTe into $CdTe_{1-x}S_x$ alloy. Within a small margin, the four profiles exhibited the same integrated area, which is consistent with the observation that the films had the same orientation, regardless of treatment.

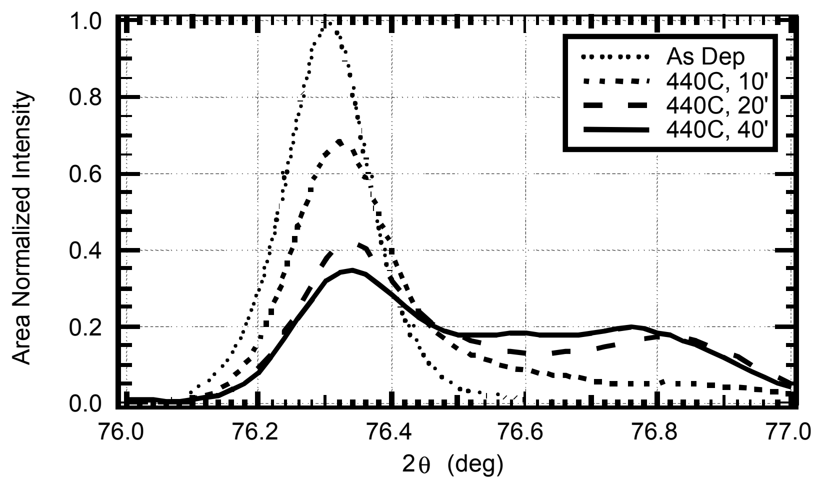

Figure 37. Measured x-ray diffraction (511)/(333) line profiles for as-deposited and time-progressively heat treated substrate configuration CdTe/CdS thin film couples. Heat treatment was carried out in $CdCl_2$:O_2:Ar vapor at 440ºC for the times shown.

Modeled diffraction line profiles for the times of Figure 37 are shown in Figure 38. The following input parameters were used to generate the line profiles of Figure 33: $D = 1.25 \times 10^{-13}$ cm^2/sec; $D_b = 1.50 \times 10^{-8}$ cm^2/sec ($\Delta = 1.2 \times 10^5$); $\delta = 2$ nm; and 10 values of grain radii with frequency of each grain size taken from Figure 36. Only a narrow range of diffusion coefficients, ± 20%, allowed the observed time-progressive profiles to be represented by the modeled time-progressive profiles.

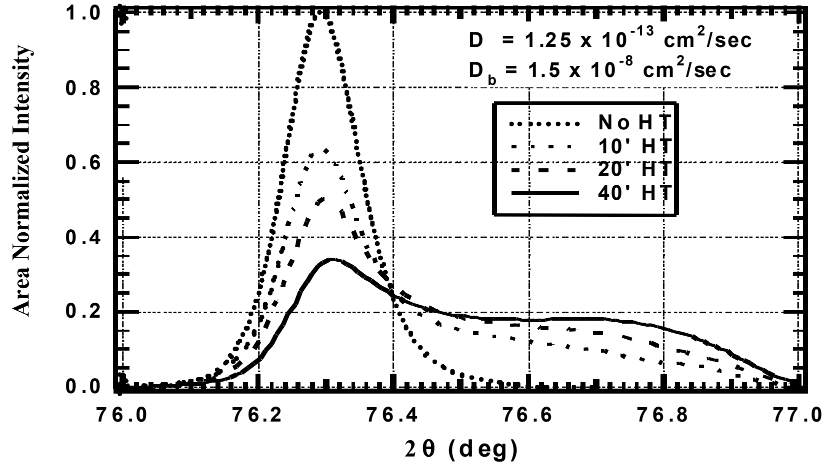

Figure 38. Modeled x-ray diffraction (511)/(333) line profiles for as-deposited and time-progressively heat treated substrate configuration CdTe/CdS thin film couples using the bulk (*D*) and grain boundary (D_b) diffusion coefficients and times shown.

For films in the superstrate configuration, evolution of the grain size distribution with treatment time must be taken into account to model the observed line profiles (Figure 39 and Figure 40). In this case, the modeled line profiles exhibit all of the dominating features of the measured profiles except for the low-angle, CdTe-rich tail.

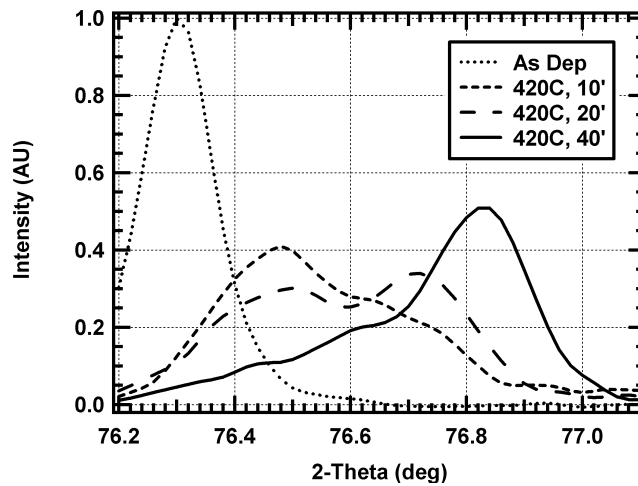

Figure 39. Measured x-ray diffraction (511)/(333) line profiles for as-deposited and time-progressively heat treated substrate configuration CdTe/CdS thin film couples. Heat treatment was carried out in $CdCl_2$:O_2:Ar vapor at 420ºC for the times shown.

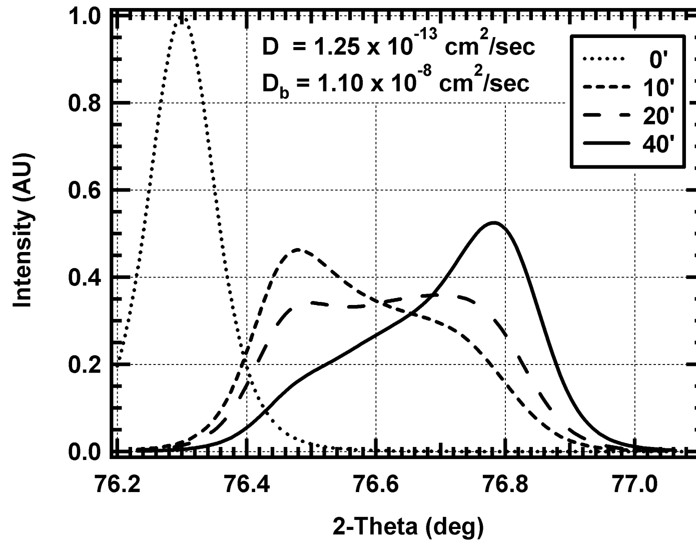

Figure 40. Modeled x-ray diffraction (511)/(333) line profiles for as-deposited and time-progressively heat treated substrate configuration CdTe/CdS thin film couples using the bulk (*D*) and grain boundary (D_b) diffusion coefficients and times shown.

4.1.1.13 Activation Energy of Diffusion

Measured diffraction line profiles were also modeled for results obtained at different treatment temperatures and fixed $CdCl_2$:O_2:Ar vapor concentration using the bulk and grain boundary diffusion coefficients shown in Table 10.

Table 10. Bulk and grain boundary diffusion coefficients used to model the measured x-ray diffraction line profiles of substrate configuration films at different treatment temperatures.

Temperature (°C)	*D* (cm^2/sec)	D_b (cm^2/sec)	Δ
400	8.00×10^{-15}	3.00×10^{-9}	3.7×10^{5}
440	1.25×10^{-13}	1.50×10^{-8}	1.2×10^{5}
475	1.80×10^{-12}	8.00×10^{-8}	4.4×10^{4}

Comparative values for the bulk diffusion coefficients over this temperature range were obtained by analysis of the Auger electron depth profiles of sulfur distribution in single crystals and are listed in Table 11. The combined bulk diffusion coefficient data for single crystal, substrate and superstrate film configurations is shown in Figure 41, giving an activation energy of 2.8 – 3.0 eV for bulk diffusion of CdS into CdTe. This activation energy is similar to that reported for the self diffusion of Cd in CdTe attributed to formation of singly-ionized Cd interstitials [44]. For substrate and superstrate configuration films, the grain boundary diffusion coefficient obtained at the three temperatures is shown in Figure 42, giving an activation energy of 2.0 eV.

Table 11. Bulk diffusion coefficient obtained from Auger depth profiles of sulfur distribution in CdTe single crystals after treatment.

Temperature (°C)	D (cm^2/sec)
390	5.0 x 10^{-15}
420	3.0 x 10^{-14}
450	1.5 x 10^{-13}

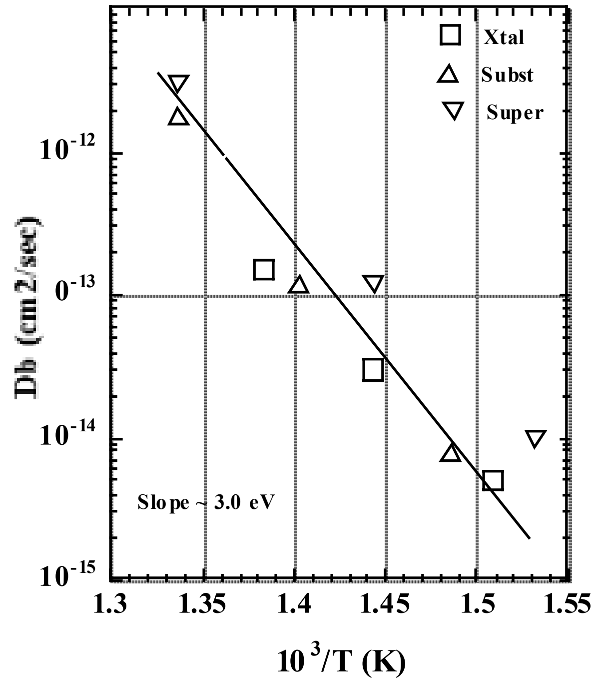

Figure 41. Bulk diffusion coefficients for single crystal CdTe, substrate, and superstrate film configurations.

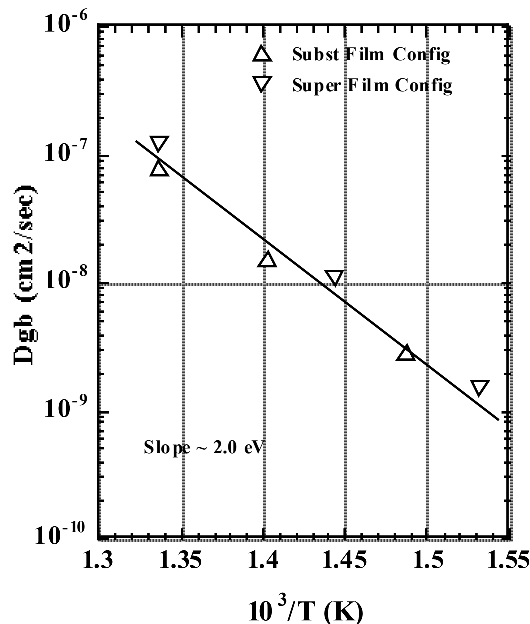

Figure 42. Grain boundary diffusion coefficients for substrate and superstrate film configurations.

The arrays used to generate the compositional distribution allow a 2- or 3-dimensional iso-composition map to be constructed. Figure 43 shows a 2-dimension isocompositional cross-section plot through grains of two different radii for a 40 minute solution with diffusion coefficients $D = 1.25 \times 10^{-13}$ cm^2/sec and $D_b = 1.50 \times 10^{-8}$ cm^2/sec.

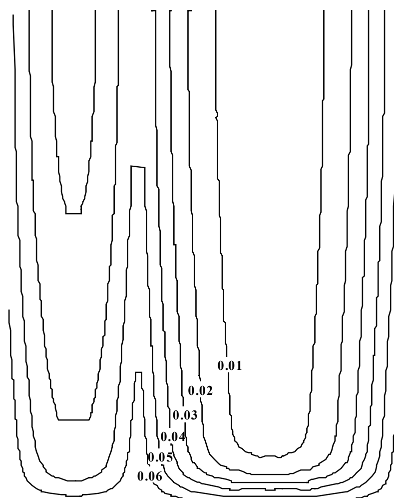

Figure 43. 2-dimensional isocompositional contour plot of sulfur distribution after diffusion for 40 minutes with $D = 1.25 \times 10^{-13}$ cm^2/sec and $D_b = 1.5 \times 10^{-8}$ cm^2/sec for grains of a 4.5 µm thick film with grain radii of 0.25 µm and 0.5 µm. Isocontours are incremented by x in $CdTe_{1-x}S_x$ in steps of 0.01.

4.1.1.14 Sensitivity to Ambient Species Concentration

Carrying out the above analysis on specimens treated in different ambient composition has allowed the effects of $CdCl_2$ and O_2 concentration to be separated with respect to bulk and grain boundary diffusion. Superstrate CdS/CdTe structures with d_{CdS} = 180 nm and d_{CdTe} = 2 µm were treated for different times at 430°C at various p($CdCl_2$) with fixed p(O_2) and at various p(O_2) with fixed p($CdCl_2$). Cadmium chloride partial pressure was established from the equilibrium vapor pressure data at each temperature employed, from 375°C to 450°C. X-ray diffraction (511)/(333) line profiles for samples treated in varying p($CdCl_2$) at 430°C for 20 minutes and fixed p(O_2) = 150 Torr are shown in Figure 44. The progression of alloy-broadened and shifted profiles clearly demonstrates the effect of $CdCl_2$ vapor concentration on the degree of sulfur diffusion. To quantify this effect, multiple treatment times were employed for selected p($CdCl_2$) and p(O_2) cases, grain size distributions were measured, and the measured profiles were modeled as above using bulk and grain boundary diffusion coefficients as the only fitting parameters.

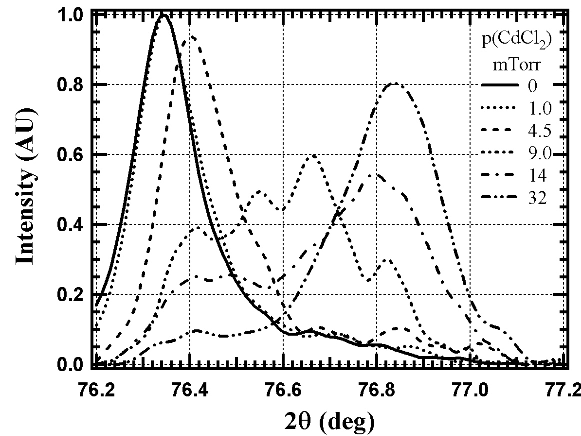

Figure 44. X-ray diffraction (511)/(333) line profiles for samples treated in varying p($CdCl_2$) at 430ºC for 20 minutes and fixed p(O_2) = 150 Torr. The profiles are shown normalized to the same area.

The resulting diffusion coefficients are shown in Figure 45 and Figure 46. For treatment at 430°C and p(O_2) = 150 Torr, p($CdCl_2$) has a significantly more pronounced effect on the grain boundary diffusion coefficient and appears to saturate above 30 mTorr. A similar trend is seen for the effect of p(O_2), with saturation occurring above 500 Torr. From this data, the bulk diffusion coefficient appears to be more sensitive to p($CdCl_2$) than to p(O_2), suggesting that oxygen primarily affects surfaces, while cadmium chloride has multiple roles involving surface and bulk properties.

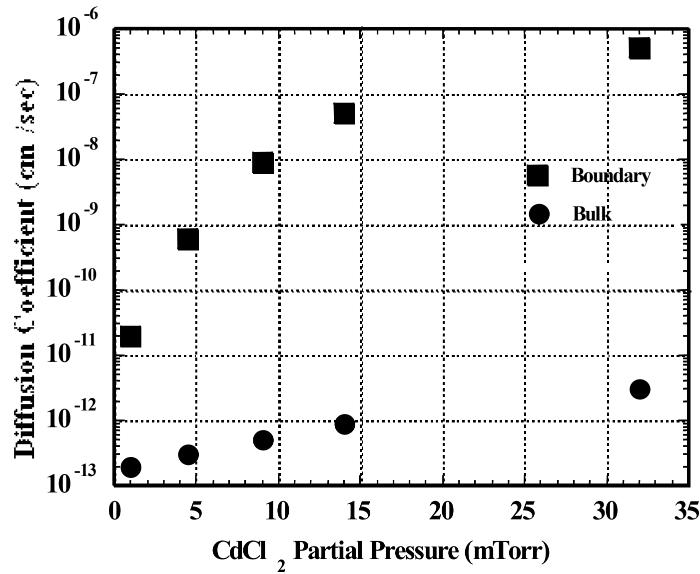

Figure 45. Bulk and grain boundary diffusion coefficient versus p($CdCl_2$) for treatment at 430°C in $CdCl_2/O_2/Ar$ at p(O_2) = 150 Torr.

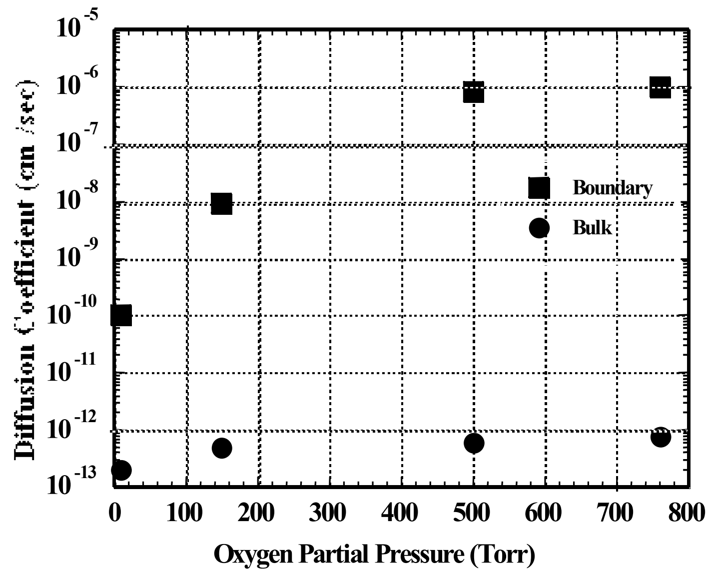

Figure 46. Bulk and grain boundary diffusion coefficient versus p(O_2) for treatment at 430°C in $ClCl_2/O_2/Ar$ at p($CdCl_2$) = 9 mTorr.

4.1.1.15 Conclusions

The diffusion of CdS into CdTe polycrystalline thin films that occurs during heat treatment in $CdCl_2$:O_2:Ar vapor is represented by a three dimensional model that accounts for bulk and grain boundary diffusion and grain size distribution. Matching modeled x-ray diffraction line profiles to measured profiles for thin-film samples time-progressively treated yielded values for the bulk

and grain boundary diffusion coefficients and their activation energies. Auger depth profiles of sulfur distribution in CdTe single crystals after similar treatment yielded comparable values of bulk diffusion coefficient. The model is applicable to either superstrate or substrate device configurations and can be used to investigate other polycrystalline thin film systems such as $CuInSe_2$-$CuInS_2$. This formalism was used to investigate the effects of treatment ambient composition on bulk and grain boundary diffusion, leading to the result that both $CdCl_2$ and O_2 concentration during treatment have a significant effect on grain boundary diffusion of S and a minimal effect on bulk diffusion. Chemical enhancement of the grain boundary diffusion process is related to the surface chemistry detailed in last year's annual report for this contract.

4.1.2 Processing Sequences to Control CdS Consumption

For CdTe/CdS/ITO (or SnO_2)/glass devices, optical absorption in the CdS layer is the predominant photocurrent loss, making it necessary to minimize the CdS film thickness in the device. Maintaining junction quality in superstrate structures with $d_{CdS} < 100$ nm depends on maintaining a uniform interface throughout the processing to avoid formation of parallel junctions between CdTe and the TCO.

X-ray diffraction and opto-electronic measurements of the interfacial region in high efficiency cells consistently show that the interface consists of $CdTe_{1-x}S_x$/$CdS_{1-y}Te_y$, where the interfacial values of x and y correspond to the solubility limits in the CdTe-CdS system at the device processing temperature. The $CdTe_{1-x}S_x$ and $CdS_{1-y}Te_y$ alloys form via diffusion across the interface during CdTe deposition and post-deposition treatments and affect photocurrent and junction behavior. Formation of the $CdS_{1-y}Te_y$ alloy on the S-rich side of the junction reduces the bandgap and increases absorption, reducing photocurrent in the 500 to 600 nm range [45]. Formation of the $CdTe_{1-x}S_x$ alloy on the Te-rich side of the junction reduces the absorber layer bandgap, due to the optical bowing parameter of the CdTe-CdS alloy system [31]. The increase in long wavelength spectral response increases photocurrent by ~ 0.5 mA/cm^2, which is nearly offset by small reduction in V_{oc} ~ 25 mV.

Other significant effects of this alloy formation include spatially non-uniform consumption of the CdS layer, penetration of CdS into the CdTe film grain boundaries, and relaxation of lattice strain between CdTe and CdS. Non-uniform consumption of CdS leads to parallel junctions between $CdTe_{1-x}S_x$/ $CdS_{1-y}Te_y$ and $CdTe_{1-x}S_x$/ ITO (or SnO_2), resulting in a net increase in J_o, which reduces V_{oc} [46]. Penetration of S-rich species into the CdTe grain boundaries can produce a three-dimensional junction, which increases the actual junction area, also reducing V_{oc}. The grain boundary penetration of CdS in CdTe is accelerated by $CdCl_2$ and O_2 chemical activity during the post-deposition treatment [11] and is extremely sensitive to the physical and chemical state of the CdTe film prior to the treatment. Evidence is mounting that suggests grain boundaries play a dominant role in controlling dark diode current, photocurrent collection, and stability, and processing techniques which control grain boundary properties should aid controlling film properties over the large areas required for module manufacturing.

4.1.2.1 Film Deposition and Treatments and Cell Fabrication

All structures were fabricated on Corning 7059 glass. Indium-tin oxide (ITO) transparent conductive oxide (TCO) films 200 nm thick were sputtered from an In_2O_3:Sn target in Ar/O_2

ambient at room temperature. The ITO/glass structures were treated in H_2/Ar at 450°C for 15 minutes to recrystallize the films and fix the electronic properties, giving sheet resistance of 15 Ohm/sq and optical transmission exceeding 80% at 400 nm. Tin oxide films with sheet resistance of 10 Ohm/sq were deposited by APCVD at 550°C. High resistance In_2O_3 and SnO_2 transparent (HRT) buffer layers were formed by oxidation of electron beam-deposited In and Sn films on the specular ITO and SnO_2 films, respectively.

CdS films were deposited by vacuum evaporation (< 80 nm) at 220°C and chemical bath deposition (CBD) at 75-80°C. Planar chemical bath deposition (PCBD) consisted of flowing aqueous solution containing cadmium sulfate, thiourea, and ammonia onto preheated superstrates. The net deposition rate was ~10 nm/min and utilization of Cd species was > 90%.

All CdS films were vapor treated in $CdCl_2$:Ar:O_2 at 400°C for 10 minutes to increase grain size and reduce formation of S-rich CdS_yTe_{1-y} alloys in the CdS film. After treatment, all CdS films were overcoated with 20 nm of PCBD CdS to allow unambiguous comparison between "baseline" thickness, $d_f > 100$ nm evaporated CdS, and all-PCBD CdS films, with $d_f < 100$ nm. CdTe films were deposited by vacuum evaporation at 300 to 350°C and growth rate of 3 nm/sec at a base pressure of 2×10^{-6} Torr . Uniform CdTe films having thickness from 0.6 μm to 5.5 μm were obtained by varying deposition time. Different post-deposition treatments were employed to control CdS diffusion into CdTe. Prior to treatment in $CdCl_2$:Ar:O_2 vapor, the CdTe/CdS/TCO/glass structures were annealed, either in air at 450°C, or argon at 580°C. The requisite treatment in $CdCl_2$:Ar:O_2 was carried out at 420°C at p($CdCl_2$) from 5 to 9 mTorr and p(O_2) from 10 to 150 Torr. Contact to CdTe was obtained by vapor treatment of the CdTe surface at ~100°C to remove oxides and to produce Te excess. Cuprous telluride was formed by electron beam evaporation of copper metal followed by heat treatment at 200°C. Acheson carbon ink was used to form the current-carrying conducting back contact pad, and devices were electrically isolated by scribing through the C/Cu_2Te/CdTe.

Film morphology and structure were characterized by tapping atomic force microscopy (AFM) and symmetric x-ray diffraction (XRD). In some cases, surface phases were identified using glancing incidence x-ray diffraction (GIXRD). Optical transmission and reflection were used to determine the transmittance of oxide layers, CdS thickness, and CdTe absorption. Current-voltage and quantum efficiency-wavelength measurements were used to characterize device operation and determine final CdS thickness.

4.1.2.2 Controlling CdS Diffusion

$CdTe_{1-x}S_x$ alloys in the absorber layer can have both beneficial and deleterious effects on device operation depending on how the alloys are formed, their composition and their compositional distribution. When the alloys form solely by diffusion of S and Cd species from the CdS film during $CdCl_2$:O_2:Ar vapor treatment, S concentration will be greatest at the interface and along grain boundaries, and the CdS film may be non-uniformly consumed. In this case, CdS consumption can be limited by reducing grain boundary diffusion, $CdCl_2$ and O_2 vapor concentrations and treatment temperature. A viable processing route already established for minimizing CdS consumption is utilizing uniform $CdTe_{1-x}S_x$ alloy absorber layers in place of pure CdTe [47].

However, for devices deposited with chemically pure CdTe, free of sulfur or oxygen species, minimizing grain boundary diffusion in CdTe/CdS structures can be accomplished by either depositing large grain CdTe films or by modifying small-grain CdTe films prior to the $CdCl_2$:O_2:Ar vapor treatment. Typically, large-grain CdTe films are deposited at high temperature, from 400°C to 600°C. Small-grain CdTe films can be modified by a high temperature anneal at 550°C to 650°C to recrystallize the film [48]. Another approach is to perform a moderate-temperature treatment at 400°C to 450°C in oxygen-containing atmosphere to form penetrating native oxides in the CdTe film prior to the $CdCl_2$ treatment. These oxides, detected using GIXRD, consist primarily of $CdTeO_3$, are relatively stable during subsequent $CdCl_2$:O_2:Ar vapor treatment and retard grain boundary diffusion of CdS as seen by the near elimination of the $CdTe_{1-x}S_x$ alloy tail in x-ray diffraction line profiles. GIXRD analysis at different incident beam angles suggests that the $CdTeO_3$ phase resides at the back surface and penetrates the CdTe film, suggesting oxide formation along grain boundaries. TEM analysis could be employed in the future to investigate the occurrence of oxides along grain boundaries for CdTe films subjected to air heat treatment. Al-Jassim, et al. [49] have shown that oxides in films deposited in oxygen-containing atmospheres exhibit retarded S diffusion during $CdCl_2$ treatment. During $CdCl_2$ treatment, CdO is also formed as a result of chemical interaction between the CdTe and the treatment ambient. Controlling the degree of oxide formation and interdiffusion with thin CdTe layers depends on optimizing the pre-anneal steps, the vapor composition and reaction temperature used during the $CdCl_2$ treatment.

Figure 47 and Figure 48 compare the $CdTe_{1-x}S_x$ XRD (511/333) line profiles after treatment in $CdCl_2$:O_2:Ar vapor for different pre-treatments of 1.3 micron thick CdTe/CdS. The line profiles have been normalized to the same area and contain quantitative information of the S content and distribution in the absorber layer. In Figure 41, a sample with argon pre-anneal at 580°C for 5 minutes exhibits significantly less $CdTe_{1-x}S_x$ alloy, hence CdS consumption, than the sample with no pre-anneal; the pre-annealed sample contains an equivalent CdS thickness of 13 nm, compared to 53 nm for the non-annealed sample. In Figure 48, 450°C air pre-anneal is shown to retard CdS diffusion, resulting in equivalent CdS consumption of 45 nm for 10 minutes and 35 nm for 20 minute pre-anneal treatment. For the $CdCl_2$ treatment temperature used, at T = 420°C, the limiting $CdTe_{1-x}S_x$ alloy composition is given by the empirical expression,

$$x = -0.0149 + (1.207\text{x}10^{-4})T + (3.940\text{x}10^{-8})T^2 + (2.393\text{x}10^{-10})T^3 \quad (43)$$

for T in Celsius and occurs at x = 0.06, corresponding to 2θ = 76.83° from,

$$2\theta = 2\sin^{-1}\left[\left(\frac{\lambda}{2}\sqrt{h^2+k^2+l^2}\right)\left(\frac{1.508}{9.7734-x}\right)\right] \quad (44)$$

where x is the alloy composition, λ is the diffracting x-ray wavelength and h, k and l are the Miller indices of the diffracting plane.

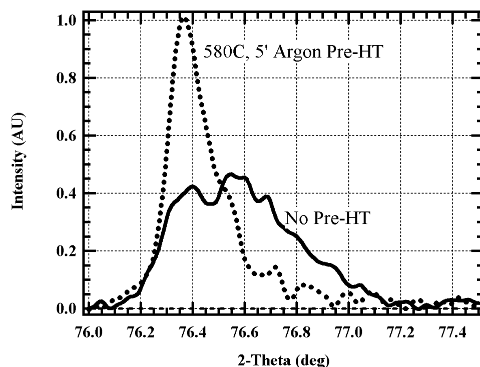

Figure 47. X-ray diffraction line profiles of $CdTe_{1-x}S_x$ (611/333) of CdTe/CdS films treated at 420°C in$CdCl_2$:O_2:Ar vapor with and without argon pre-anneal (pre-HT) step.

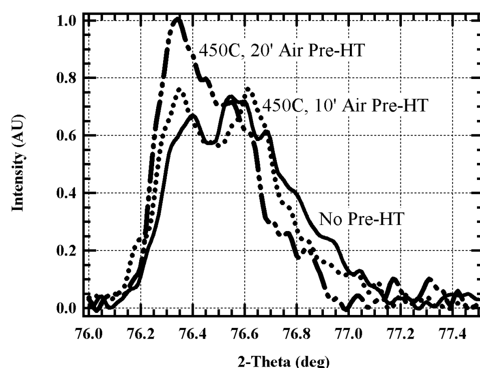

Figure 48. X-ray diffraction line profiles of $CdTe_{1-x}S_x$ (511/333) of CdTe/CdS films treated at 420°C in $CdCl_2$:O_2:Ar vapor with and without air pre-anneal (Pre-HT) step.

In summary, the diffusion of CdS into CdTe in thin-film structures occurs via Fickian diffusion from CdTe-CdS interface and grain boundaries into 'bulk' crystallites. For chemically pure CdTe films deposited in vacuum and treated in $CdCl_2$:O_2:Ar vapor, the bulk diffusion coefficient is consistent with that measured in CdTe single crystals subjected to the same treatment. The activation energy for the bulk diffusion process, 2.0 eV, is consistent with formation of ionized Cd interstitials, suggesting that CdS diffusion into CdTe is limited by the redistribution of Cd species. Grain boundary diffusion in the films is significantly enhanced during post-deposition thermal treatment with increasing $CdCl_2$ and O_2 vapor concentration. By heat treating in air prior to $CdCl_2$ exposure or deposited in oxygen-containing atmosphere, the grain boundary diffusion can be substantially reduced, utilizing native oxides to retard sulfur transport within grain boundaries.

4.1.3 CdS, CdZnS, and High Resistance Transparent Buffer Layers

In last year's report, a method for depositing CdS films by a planar chemical bath method (PCBD) was described. The PCBD method is superior to conventional beaker-type CBD methods due to these features: 1) enhanced heterogeneous nucleation, with reduced adherent homogeneously-formed particulates, 2) > 90% utilization of cadmium species; and 3) uniformly

thick deposits obtained with no externally applied mechanical agitation. As with evaporated CdS films, the PCBD film properties for devices benefit from a brief, 10 minute, treatment in $CdCl_2$:O_2 ambient at 400°C prior to CdTe deposition. This treatment reduces formation of $CdS_{1-y}Te_y$ alloy from diffusion of Te into the S-rich side of the junction by increasing grain size and forming oxides, which reside on grain surfaces and penetrate grain boundaries. The oxide-producing reaction between $CdCl_2$ vapor and O_2 vapor and CdS is:

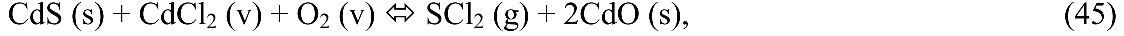

$$CdS\ (s) + CdCl_2\ (v) + O_2\ (v) \Leftrightarrow SCl_2\ (g) + 2CdO\ (s), \qquad (45)$$

with free energy of reaction at 400°C of -12.5 kcal/mol. An analogous reaction occurs between CdTe in $CdCl_2$:O_2 ambient. Confirmation of this chemistry was obtained by detection of cadmium oxide phase in heat treated powder mixtures and films, using glancing incidence x-ray diffraction. As the stable equilibrium reaction product for the halide-air ambient, CdO is expected to behave as a barrier to subsequent reaction and diffusion of Te and Cd species from the CdTe layer into the window layer material. As an insulating oxide, CdO may also electrically passivate grain boundaries and surfaces. In addition, the thermal treatment sharpens the optical transmission edge as found for evaporated CdS films. This sharp optical cutoff is retained in the quantum efficiency of devices, signifying the low uptake of Te by the CdS film.

The PCBD deposition method was adapted for deposition of $Cd_{1-x}Zn_xS$ window layers by addition of $ZnCl_2$ to the deposition mixture. Alloying CdS films with ZnS can widen the device optimization window by relaxing the thickness required to obtain a specified photocurrent. As Table shows, for a specified photocurrent, e.g., ~25 mA/cm^2, using $Cd_{1-x}Zn_xS$ alloy with x ~ 0.3 would enable the thickness to be increased from 25 nm to 60 nm. For fixed window film thickness, e.g., 100 nm, nearly 2 mA/cm^2 can be gained by using $Cd_{1-x}Zn_xS$ alloy with x ~ 0.3 instead of pure CdS. Recent calculations showing an increase in valence band offsets in Zn-VI semiconductors suggest that addition of Zn to the interface may translate to higher V_{oc} [50]. Devices made with 50 nm thick $Cd_{0.95}Zn_{0.05}S$ films deposited by chemical bath deposition exhibited demonstrably higher V_{oc} and FF than those with 50 nm or more of pure CdS with no buffer layer between the TCO and CdS (Table 13).

Table 12. Photocurrent estimates for different window layer thickness with 7059/ITO absorption and 10% panchromatic reflection loss.

d(CdS) (nm)	Photocurrent (mA/cm^2)		
	CdS	$Cd_{0.7}Zn_{0.3}S$	$Cd_{0.5}Zn_{0.5}S$
0	25.6	25.6	25.6
25	24.5	25.1	25.4
50	23.6	24.7	25.3
75	22.9	24.3	25.1
100	22.4	24.0	25.0

Cross-film conductivity measurements were made of 40 nm thick PCBD CdS and $Cd_{0.95}Zn_{0.05}S$ films deposited onto ITO/7059 glass structures with a 175 µm wide gap. Table 12 shows dark and light, ~80 mW/cm^2 ELH, conductivity results for films before and after treatment in

$CdCl_2:O_2$ vapor at 400°C for 10 minutes. The dark measurement was made prior to the light since the films were found to exhibit higher (2X) dark conductivity after exposure to the light. The original dark conductivity was obtained after relaxation on the order of 30 minutes. All the films exhibit photoconductivity. For CdS films, the dark and light conductivity increased after the treatment, but the photoconductivity decreased. For the $Cd_{0.95}Zn_{0.05}S$ films, treatment increased dark and light conductivity proportionally.

Table 12. Dark and light (~80 mW/cm^2 ELH) conductivity of 40 nm thick CdS and $Cd_{0.95}Zn_{0.05}S$ films deposited by PCBD before and after treatment in $CdCl_2:O_2$ vapor at 400°C for 10 minutes.

Sample	Treatment	σ_d (S/cm)	σ_l (S/cm)	σ_l/σ_d
CdS	as-deposited	1×10^{-5}	9×10^{-4}	90
CdS	$CdCl_2$ HT	3×10^{-4}	7×10^{-3}	23
$Cd_{0.95}Zn_{0.05}S$	as-deposited	4×10^{-4}	3×10^{-2}	75
$Cd_{0.95}Zn_{0.05}S$	$CdCl_2$ HT	7×10^{-4}	5×10^{-2}	71

Table 13. AM1.5 J-V results (28°C) for devices with 7059/ITO, 7059/ITO/50nm $Cd_{0.95}Zn_{0.05}S$, 7059/ITO/In_2O_3/CdS, and 7059/SnO_2/SnO_2/CdS window layers and evaporated CdTe. All processed with 580°C, 5 min pre-anneal and 420°C, 15 min $CdCl_2:Ar:O_2$ treatment.

TCO	HRT nm/ type	d_f(CdS) nm	V_{oc} mV	J_{sc} mA/ cm^2	FF %	Eff %
ITO	None	0	440	25.0	47	5.0
ITO	None	50	590	23.9	47	6.6
ITO	None	110	790	20.3	70	11.3
ITO	None	30 CdZnS	750	23.2	62	10.8
ITO	20 In_2O_3	30	652	23.9	52	8.1
ITO	50 In_2O_3	< 20	754	26.2	60	11.9
ITO	50 In_2O_3	100	790	21.8	70	12.0
SnO_2	None	0	440	18.0	46	3.5
SnO_2	None	90	753	22.8	63	10.8
SnO_2	50 SnO_2	< 20	790	26.0	68	13.8

Devices were also fabricated with high resistance oxide buffer layers between the TCO and CdS film, demonstrating retention of junction quality for devices with CdS < 100 nm (Table 13). Incorporating a high resistance SnO_2 buffer layer on SnO_2/7059 has resulted in devices with conversion efficiencies near 14% for evaporated CdTe with PCBD CdS. This beneficial interlayer may be due to improved CdS morphology since the chemical bath CdS film is

conformal to the larger grain size obtained with oxidized metal films. Figure 49 shows AFM images of the surface morphology of as-deposited conventional CBD CdS films on ITO/7059 and PCBD CdS films on ITO/7059 and In_2O_3/ITO/7059 superstrates.

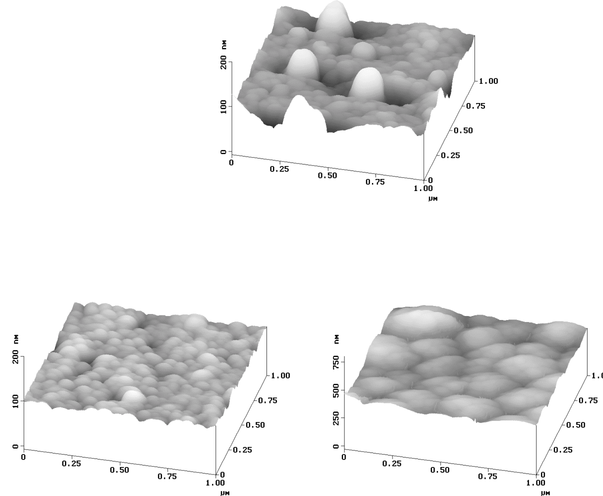

Figure 49. Tapping atomic force microscope images of CBD (top) and PCBD (lower, left and right) CdS films. The CBD and left PCBD films are on specular ITO/7059 glass. The right PCBD film is on In_2O_3/ITO/7059.

4.2 Contact Processing and Stress-Induced Degradation in CdS/CdTe Solar Cells

4.2.1 Effect of Stressing on Junction and Contact

4.2.1.1 Background

CdTe/CdS modules in field testing scenarios are reported to be stable [51,52]. However, no clear correlation has been found between processing parameters and either these stable existence-proof cases or those that changed in field testing. Recent work to accelerate these processes at the laboratory scale (stress testing) have shown that typically the V_{oc} and FF degrades, particularly for devices held at moderate forward or reverse bias [53,54]. Also, there are reports of improvements that occur after relatively short periods [51,54]. The back contact process is strongly implicated in the stress-induced degradation [54,55], especially with respect to the presence of Cu and its compounds, which are sensitive to small, localized fields, in both electrochemical and electromigration processes [56]. A review of CdTe solar cell stability and the role of Cu has recently been published [57]. A difficulty in evaluating changes in device behavior is sample-to-sample variability in both CdS/CdTe films and post-deposition treatment and contacting processes. To minimize these variations, CdS/CdTe films from a single source were employed. In this paper, an analysis is presented of stress-degraded behavior, for devices made with 3 different back contact processes and stressed at different electrical bias points.

4.2.1.2 Experiment: Sample Fabrication and Stress Conditions

Devices were fabricated using glass/SnO_2/CdS/CdTe layers supplied by First Solar LLC and back contact processes developed at (IEC). The "wet" process involves a bromine/dichrol/hydrazine etch, leaving a ~30 nm Te layer [58]. The "dry" process uses a Te vapor treatment to deposit a 10 nm Te layer [59]. Device contacting was finished with an evaporated Cu layer (8-15 nm for the wet process and 2-6 nm for the dry process), followed by an application of Acheson 505SS carbon ink conductor. The initial efficiency of devices processed with Cu was 10 to 12%. Since Cu acts as both a p-type dopant and forms a Cu_2Te contact layer and can thus influence device operation in several ways, it was necessary to fabricate devices without Cu. In this case, the dry process was used to form the Te layer on which the carbon ink was applied. These devices exhibited lower V_{oc} and FF, blocking contact behavior, and initial efficiencies of 7 to 9%. It is important to note that, given the strong influence of contact processing on initial cell performance and stress-induced changes [54,55,60], the results on devices reported here are not representative of First Solar product using their contact.

IEC has constructed a system for stressing of CdS/CdTe solar cells by exposure to thermal, atmospheric, electrical, and illumination bias. Unique aspects of the equipment are: 1) controlled ambient conditions (dry bottled air, Ar, H_2/Ar or vacuum); 2) a wide range of active electrical bias; 3) T from 28-120°C; and 4) monitoring device performance *in-situ* during stress. No clear dependence on stress ambient was identified, so all devices reported here were stressed in dry air. Standard pumping and purging procedures were used to reduce gas phase contamination such as water vapor from the stress chamber before beginning the stress treatment. Electrical bias points used included reverse bias (RB) of –0.5V, short circuit (SC), maximum power (MP), open circuit (OC), and forward bias (FB) well beyond OC. Stress experiments were carried out for 10 days at 60° in dark or 100°C under ~1.2 suns.

4.2.1.3 Effect of Stress: Partially Completed Devices

CdS/CdTe structures stressed at OC at 100°C without any contact layer (no Cu or C) yielded comparable performance (V_{oc}~0.80 V) to unstressed films once the contact was applied. CdS/CdTe structures were stressed at OC with a 6 nm Cu layer but no C contact at 100°C. After applying the C paste back contact, the completed devices had V_{oc} ~ 0.65V but no blocking contact. Upon further stressing, there was no further loss in V_{oc} but curvature developed in forward bias beyond V_{oc} This indicates that the CdS/CdTe junction is intrinsically stable, that the presence of Cu during stress is correlated with junction (V_{oc}) degradation, and the blocking contact is formed only when stressed with the C contact.

4.2.1.4 Separating Contact and Junction Behavior

A CdS/CdTe solar cell having an initial efficiency of 11.8% and V_{oc} of 0.82V was stressed at OC at 100°C for 6 weeks in air at 2 suns at Colorado State University. This reduced the efficiency to 7.2% and V_{oc} to 0.73V (Figure 50). J_o increased by 30X, from 3E-8 to 8E-7 mA/cm^2, but there was no change in A-factor (~1.6), suggesting that the magnitude of recombination changes but not the mechanism (bulk recombination). This was confirmed with V_{oc} -T measurements.

Figure 50 also shows that curvature develops after stress in both light and dark JV curves at forward bias, most likely due to a blocking contact. After stressing, the original carbon contact was removed, the CdTe surface was re-etched in weak bromine-methanol, and a new C contact was applied. The efficiency increased to 9.1% with no change in V_{oc}, J_0 and A. The blocking contact disappeared and the FF increased significantly. This clearly demonstrates that the curvature in forward bias is associated with the back contact. A contact barrier height of 0.3 eV has been determined after stressing [61].

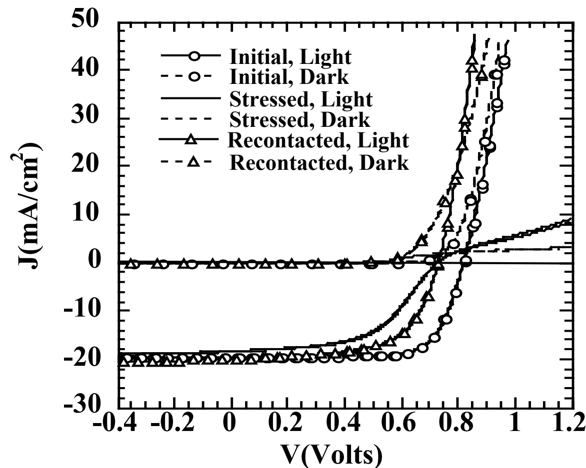

Figure 50. Light and dark JV curves for CdS/CdTe solar cell: initial; 6 week stress at 100°C at OC; and following re-contacting.

4.2.1.5 Effect of Electrical Bias and Cu

Figure 51 shows the relative change in efficiency after stress as the ratio of efficiency after stress/before stress, for devices stressed at RB, SC, MP or OC for 10 days at 100°C in dry air. Devices with wet or dry contacts show similar changes with bias. Stress at SC always shows the least degradation in performance while stress at OC has the greatest degradation. Similar bias dependence has been found for cells with Cu that are stressed in H_2/Ar or Ar atmospheres, stressed at lower temperature (75°C) or have different Te layer processing. This non-monotonic behavior with bias suggests two different degradation processes for devices with Cu, whose combined impact has a minimum at SC bias stress. The error bars for the dry contact are based on a large number of samples and stress experiments. The variability in results is attributable to the interaction of process complexity with multiple degradation mechanisms. Devices without Cu degrade nearly independent of bias, and they have much less degradation at forward bias compared to devices with Cu. JV curves for devices biased at RB and SC behave similarly, while those at MP and OC have a different but common degradation mode. We simplify our discussion by considering two bias points, OC and SC. Figure 52 shows light and dark JV for devices stressed at OC and SC.

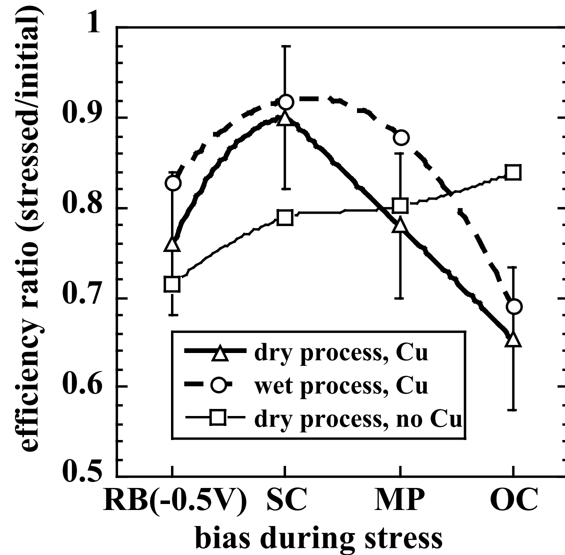

Figure 51. Relative change in efficiency for devices with different contacts after stressing at bias shown in light for 10 days at 100ºC.

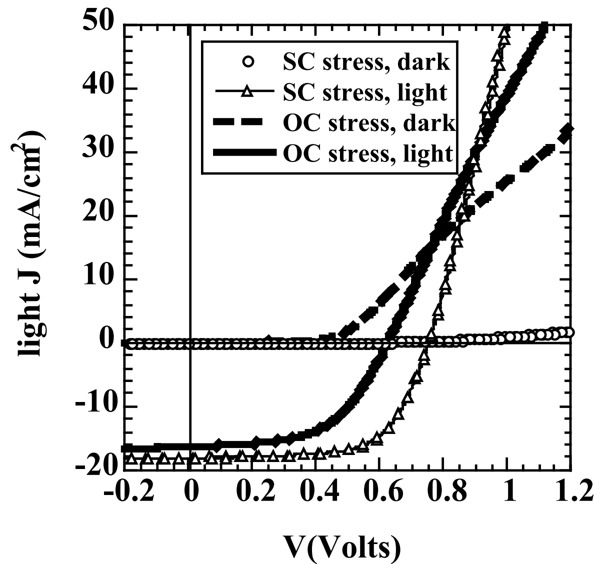

Figure 52. Light and dark JV curves after SC and OC stress for 10 days at 100ºC. Dark curve for SC stress is nearly horizontal.

Devices stressed at SC have a smaller loss in V_{oc} (~50 mV) and FF (~5%) than those stressed at OC but develop a large cross-over between the light and dark curves, indicating a large photoconductivity effect. This has been attributed to formation of photoconductive Cu-doped CdS [57], although photoconductivity in CdTe cannot be excluded solely based on our measurements. Note that the formation of the blocking contact in Figure 52 was much weaker than in Figure 50, which is typical of cell-to-cell variability.

Since degradation was larger at OC than at SC, we extended the range of forward bias stress to 2.5 V. In this study, devices were in the dark to eliminate current flow at 0V. Figure 53 shows FF and V_{oc} for devices with and without Cu for stress in the dark for 10 days at bias from 0 to +2.5V at 60°C. There was negligible degradation for stress from 0 to 1V but significant change occurs for bias greater than 1V. V_{oc} and FF at 0V stress bias are essentially the same as the initial values. Devices with Cu show a strong bias dependence, with V_{oc} and FF decreasing similarly under forward bias. In contrast, devices without Cu degraded very little at any bias under these conditions. Note that the current density for devices with Cu was ~300 mA/cm^2 under +2.5V but ~100 mA/cm^2 for devices without Cu due to their current-limiting blocking contact.

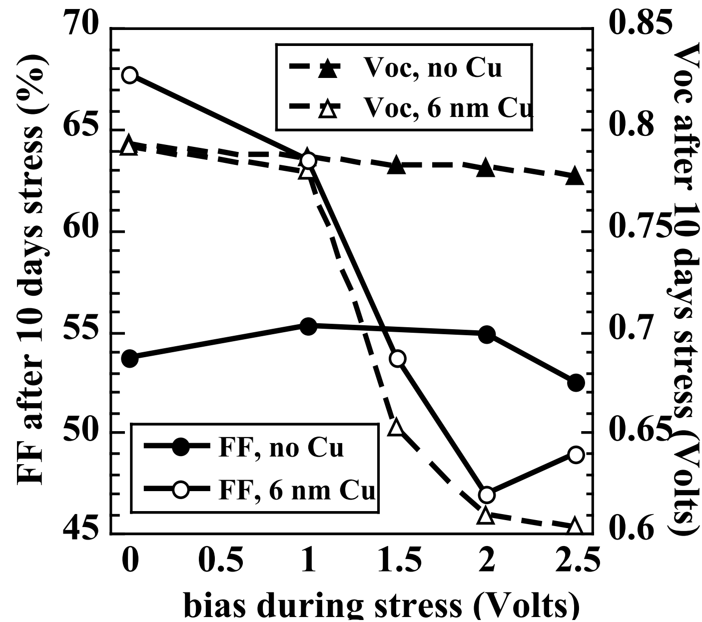

Figure 53. FF and V_{oc} for devices with 0 or 6 nm Cu for stress under FB in the dark at 60°C for 10 days.

4.2.1.6 Bias and Temperature Dependence

The data in Figure 53 shows final performance after 10 days of stress at 60°C in the dark. In order to separate the effects of temperature, time and bias, the devices with Cu were initially stressed for one day at 28°C, then stressed for 1 day at 60°C, and then finally for the full 10 days. Then the device was recontacted as described above. The dark JV data has been analyzed by plotting dV/dJ vs 1/J as shown in Figure 54 for the device with +2V bias. The slope is AkT/q, the intercept is the series resistance R_S, and any curvature at large values of J at +2V bias, a significant blocking contact has developed which remained unchanged with further stress. Then, after 1 day at +2V at 60°C, the A factor and R_S increased, then remain unchanged for the next 9 days. After recontacting, Figure 54 shows that the blocking contact has completely disappeared but the increased A-factor and resistance remain unaffected (same as in Figure 50). This data indicates that degradation at forward bias occurs rapidly, even at 28°C, and the blocking contact is triggered by forward bias while the increase in junction recombination and resistance requires

elevated temperatures. These recontacting results from a device with a dry contact are in good agreement with the device of Figure 50, which had a wet contact and was stressed for longer times at a higher temperature at OC. The similarity in results with stress and recontacting strengthens the conclusions discussed below. Figure 55 shows analysis of devices stressed at zero Volts, which were on the same substrate as the device shown in Figure 54. At zero bias, there was no change in R_s or A with stress or recontacting, and only a small amount of curvature developed. Together, Figure 54 and Figure 55 show conclusively that forward bias and elevated temperature triggers degradation in junction, contact and resistance properties. Recontacting only eliminates the blocking contact, not the junction degradation or high resistance.

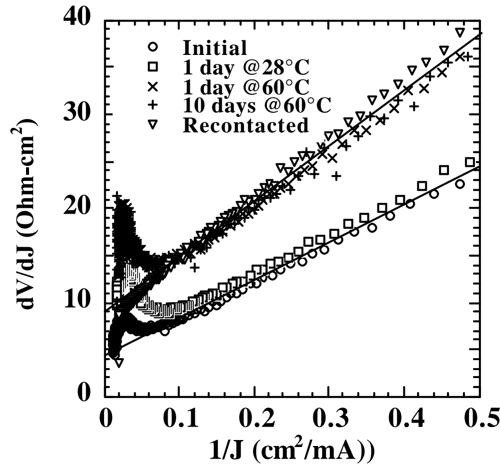

Figure 54. Analysis of dark JV curve as dV/dJ for device stressed at +2V bias at different times and temperatures including after recontacting. The slope is AkT/q and the intercept is R_s, and curvature at large J indicates a blocking contact. (a) has A = 1.6, R_s = 4Ω-cm²; (b) A = 2.2, R_s = 9Ω-cm².

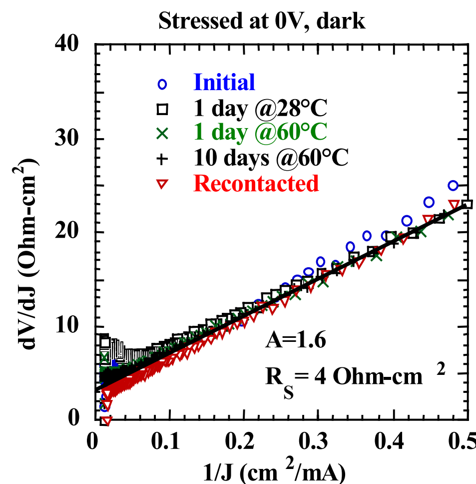

Figure 55. Analysis of dark JV curve as dV/dJ for device stressed at 0V bias at different times and temperatures, including after recontacting. All curves are consistent with A = 1.6, R_s = 4Ω-cm².

4.2.1.7 Spectral Response (SR) and Capacitance-Voltage (CV) Measurements

In order to gain further insight into how the junction, bulk, and contact change with stress, we have begun to monitor SR and CV before and after stress.

Capacitance has been measured in the light and dark at10 kHz from –2V to +0.5. Care must be taken to obtain the correct bias across the device in forward bias or under light since the forward current flow causes large voltage losses in the instrumentation. Capacitance values in the dark are always smaller than in the light, indicating that trapping of light generated carriers narrows the space charge width. To first order, there is little difference in the light or dark CV between devices stressed at OC or SC, despite their having large differences in dark JV characteristic. After stress, depletion widths at 0V bias are on the order of 1 μm in the light and 2 μm in the dark. At 0.5V bias, the depletion widths have decreased to about half those values. It is surprising that there is not a bigger difference in capacitance or depletion width between light and dark after stress, given the large difference in JV curves, especially for devices stressed at 0V (Figure 52). This might suggest that carriers responsible for changing the resistance or junction properties are trapped too deep in energy to respond at 10 kHz at room temperature, or approximately deeper than 0.5 eV.

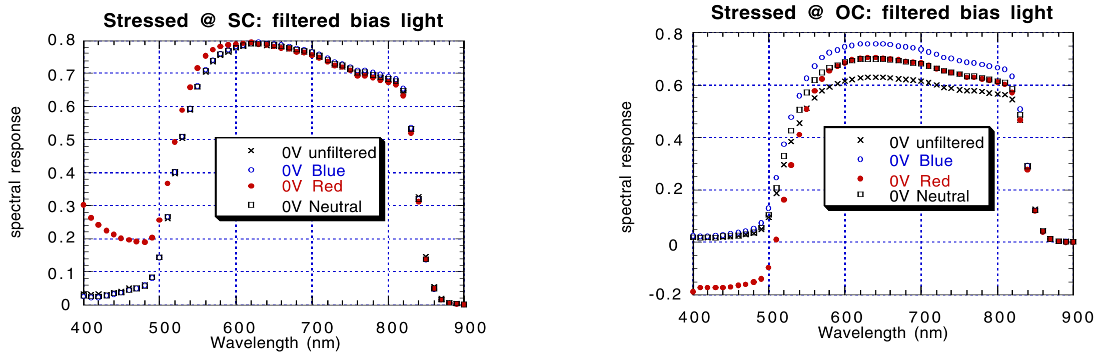

Figure 56 (a) and (b). Spectral response for devices stressed at SC and OC, respectively, at 0V bias with different bias filters; unfiltered = ELH bias light; blue = ELH <600 nm; red = ELH >700 nm; neutral = ELH with 30% ND filter (~same intensity as other 2 filters).

SR data has been measured under different bias light spectra at 0 and –1V. Figure 56(a) and Figure 56(b) show the SR measured at 0V with different bias light filters. The devices were stressed at SC and OC bias, respectively. Before stress, the QE was independent of bias light spectrum or intensity, or bias (0 or –1V). After stress, interesting differences show up in the region between 400 and 550 nm for measurements with red bias light (>700 nm). The SR between 400 and 550 nm increases for the device stressed at SC and actually decreases below 0 for the device stressed at OC. We have seen this behavior on several but not all devices stressed under these bias conditions. There was no evidence of a blocking junction or sign reversal in V_{oc} for JV or CV characteristics measured with the blue or red filters, so we do not suspect a opposing junction is formed at the front contact. Instead, we interpret this change in SR at short

wavelengths as due to photoconductive response in either the CdS or the CdTe (or $CdTe_xS_{1-x}$) near-junction region. The chopped ac signal can modulate the trapped charge and field profile as is well known from studies on $CdS/CuInSe_2$ and a-Si. Both cases require a region of high resistance in the dark whose resistivity is modulated by the chopped light. These results are significant because they indicate distinct changes in the device junction region, which are dependent on the bias during stress. This result may relate to the presence of Cu in the CdS or junction region, which is well known to increase the photoconductivity of CdS. Cu has been identified by SIMS and PL to be present in the front junction region and in the CdS.

4.2.1.8 Partial Recovery from OC Degradation Using SC Bias

It has been commonly observed in our stress studies that OC is the least stable and SC is the most stable bias point, as shown in Figure 51. We have observed that V_{oc} of devices stressed at OC were partially recovered when their bias was switched to SC at 100°C. These previous studies were for 10 days in air. We decided to more fully investigate, for much longer times, the recovery at J_{sc} of cells degraded at V_{oc} and vice versa, including the effect of atmosphere.

Two identical pieces of First Solar Cds/CdTe received standard dry contact processing (~50 Å Cu followed by C paste). They were stressed at 100°C, at 1.2 suns, in either air or H_2/Ar for 900 hours. Initially, one cell was at SC but was switched to OC after 580 hours. The other 3 were at OC but were switched to SC after 1, 20 and 580 hours. V_{oc} was monitored in-situ during the stress. Figure 57(a) and Figure 57(b) show the time dependence of V_{oc} on linear and logarithmic time scale for two of the bias sequences, for devices in air or H_2/Ar. All devices started with V_{oc} (25°C) of 790-810 mV and V_{oc} (100°C) = 670-680 mV.

First, note that there was no difference in degradation or recovery between devices in air or H_2/Ar, so we make no further distinctions. The device initially at SC lost ~30 mV in the first 30 hours, then remained stable until 580 hours, when it was switched to OC. A very rapid decrease is then observed, losing 100 mV in the next 100 hours. The device stressed initially at OC loses 150 mV in 20 hours. At that time, it is switched to SC bias. Interestingly, the V_{oc} shows an additional rapid decay of 50 mV within the next few hours, then begins a steady increase. Recovery saturated around 300 hrs. Although not shown in Figure 57(a) and Figure 57(b), the device biased at OC for just one hour, then switched to SC, never recovers fully and degrades steadily at longer times. Thus, even 1 hour stress at OC bias has permanent nonrecoverable degradation. The device biased at OC for 580 hours before switching to SC had no recovery in the next 300 hours. Comparing devices which were at OC for 1, 20 and 580 hours before being switched to SC, we conclude that the longer the device is stressed at V_{oc}, the lower the value of the maximum V_{oc} it can recover to. Figure 56(b) shows that the degradation rate is at least 10 times faster than recovery, and degradation and recovery are independent of atmosphere. Taken together, these results suggest a very rapid and progressively less reversible degradation mechanism for V_{oc}, which is strongly bias dependent but atmosphere independent.

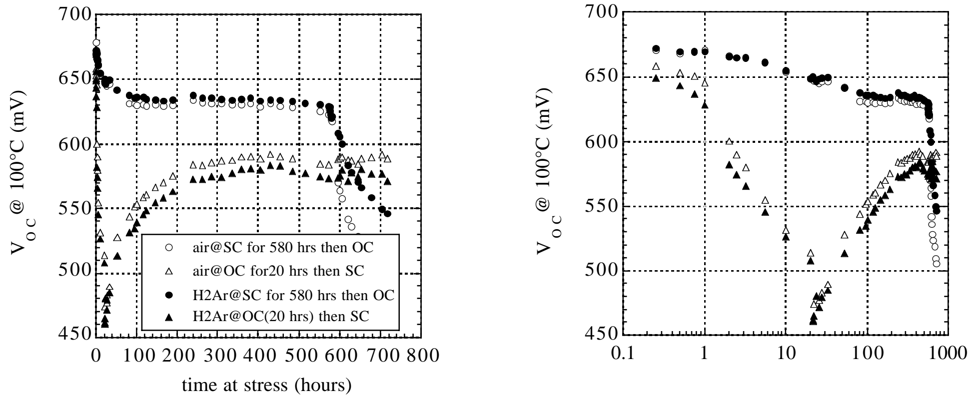

Figure 57 (a) and (b). Degradation and recovery of V_{oc} at 100ºC in air or H_2/Ar on linear (8(a)) and log scale (8(b)). In each atmosphere, one cell was at SC for 580 hours, then switched to OC. The other was at OC for 20 hours, then switched to SC. Open symbols for stress in air, solid symbols for H_2/Ar.

4.2.2 Mechanisms for Degradation

We propose a model consistent with some, but not all, of the above results: devices with Cu under OC or forward bias degrade much more than under SC or 0V bias; degradation in V_{oc} or junction properties occurs rapidly (<24 hrs) even at 28°C; and a blocking contact forms to the CdTe. Using glancing incident x-ray diffraction at low incident beam angles to detect thin phases on CdTe surfaces before and after stressing, with contact removed, we have observed that the cuprous telluride present initially [61] is converted to cupric telluride after stressing. The Cu species liberated by this process are unaccounted for in our measurements. This relatively rapid change, together with the very small change at 0V, suggests that positive Cu ions could be generated and moved by field-driven diffusion along grain boundaries, or electromigration. This mechanism is discussed in detail in [57]. Positively charged Cu^{++} is available under bias by the weakly favored reaction:

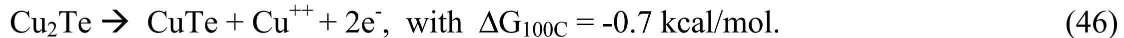

$$Cu_2Te \rightarrow CuTe + Cu^{++} + 2e^-, \text{ with } \Delta G_{100C} = -0.7 \text{ kcal/mol.} \quad (46)$$

Note that while Cu_2Te is a highly conductive p-type material and makes a good ohmic contact to CdTe, CuTe is a poor conductor and could be responsible for the blocking contact.

However, there are several observations, which are inconsistent with the electromigration of Cu along grain boundaries. It fails to explain why Cu-free devices degrade, why degradation isn't monotonic with bias (SC is most stable bias), or why large photoconductivity develops for stress at SC or RB. Also, the back contact barrier opposes that of the main junction, leading to Cu ions drifting in the opposite direction at the back compared to the CdS junction at a given bias. Thus, while electromigration of Cu along grain boundaries is a plausible mechanism, it is certainly not the only one responsible.

4.2.3 Phenomenological Model and Conclusions

We have shown that there are at least 3 mechanisms operative in CdS/CdTe devices under thermal and bias stress. One, which occurs at forward bias, is Cu-related, field-driven, occurs in ~hours, greatly increases the recombination, and is partially reversible with field [57,62]. A second mechanism leads to formation of a blocking contact, which also occurs rapidly and is likely related to loss of Cu, but is not reversible with field. It is eliminated by replacing the contact without additional Cu. The third mechanism, which occurs under reverse bias, is much slower, may not be Cu related, and changes the photoconductivity of either the CdS or CdTe. We propose that Cu^{++} is liberated from the Cu_2Te layer and moves along grain boundaries under forward bias. The concentration-gradient driven diffusion lengths (using D values from [63]) for Cu in bulk CdTe and along grain boundaries have been calculated for 1 hour at 100°C. Cu would move 0.3 μm in the bulk and 30 μm along grain boundaries. Clearly, grain boundaries are important channels for Cu motion.

5 ABSTRACT

This report describes results achieved during phase I of a three-phase subcontract to develop and understand thin film solar cell technology associated to $CuInSe_2$ and related alloys, a-Si and its alloys and CdTe. Modules based on all these thin films are promising candidates to meet DOE long-range efficiency, reliability and manufacturing cost goals. The critical issues being addressed under this program are intended to provide the science and engineering basis for the development of viable commercial processes and to improve module performance. The generic research issues addressed are: 1) quantitative analysis of processing steps to provide information for efficient commercial scale equipment design and operation; 2) device characterization relating the device performance to materials properties and process conditions; 3) development of alloy materials with different bandgaps to allow improved device structures for stability and compatibility with module design; 4) development of improved window/heterojunction layers and contacts to improve device performance and reliability; and 5) evaluation of cell stability with respect to illumination, temperature and ambient and with respect to device structure and module encapsulation.

6 REFERENCES

1. E. Niemi, J. Hedström, T. Martinsson, K. Granath, L. Stolt, J. Skarp, D. Hariskos, M. Ruckh and H. W. Schock, *Proc. 25th IEEE PVSC* (1996), p. 801.
2. M. Powalla, G. Voorwinden, and B. Dimmler, *Proc. 14th European PVSEC* (1997), p. 1270.
3. T. Negami, S. Nishiwaki, Y. Hashimoto, N. Kohara and T. Wada, *Proc. 2nd WCPEC* (1998), p. 1181.
4. R. E. Rocheleau, Ph. D. Dissertation, University of Delaware (1981).
5. P. Clausing, *Z. Phys*. **66**, 471 (1930).
6. L. Valyi, *Atom and Ion Sources*, John Wiley & Sons, London, 86 (1977).
7. W. N. Shafarman and J. Zhu, *Thin Solid Films* **361-362**, 473 (2000).
8. K. Kurzydlowski and B. Ralph, CRC Press, Boca Raton, FL, CRC Series in *Mat. Sci. & Tech*., 1995.
9. W. N. Shafarman, R. Klenk and B. E. McCandless, *J. Appl. Phys*. **79**(9), 7324 (1996).
10. E. Tarrant, J. Bauer, R. Dearmore, M. E. Dietrich, G. T. Fernandez, O. D. Frausto, C. V. Fredric, C. L. Jensen, A. R. Ramos, J. A. Schmitzberger, R. Ed. Wieting, D. Willett and R. R. Gay, NREL/SNL PV Program Review, *AIP Conf. Proc*. **394** (1996), p. 143.
11. B. E. McCandless and R. W. Birkmire, presented at 16th European PVSEC, Glasgow, Scotland, May 1-5, 2000.
12. Vladimir Novikov, *Grain Growth and Control of Microstructure and Texture in Polycrystalline Materials*, CRC Press (1997).
13. R. W. Birkmire and M. G. Engelmann, *Proc. 15th NCPV Review* **462** (1998), p. 23.
14. G. Gilmer and H. Farrell, *J. Appl. Phys.,* **47**(10), 4373 (1976).
15. R. A. Young and D. B. Wiles, *J. Appl. Cryst.* **15,** 430 (1982).
16. Amy Swartzlander, NREL, AES measurements, private communication.
17. S. Guha, J. Yang, P. Nath and M. Hack, *Appl. Phys. Lett.* **49**, 218 (1986).
18. J. Rath, C. van der Werf, F. Rubinelli and R. Schropp, *Proc. 25th IEEE PVSC* (1996), p. 1101.
19. S. Hamma, P. Stahel, P. Roca and I Cabaroccas, *Proc. 2nd World Conf. PCSEC* (1998), p. 853.
20. M. Kondo, Y. Toyoshima, A. Matsuda and K. Ikuta, *J. Appl. Phys.* **80**, 6061 (1996).
21. J. Rath, J. Wallinga and R. Schropp, *Matl. Res. Soc. Symp. Proc*. **420** (1996), p. 271.
22. B. Goldstein, C. Dickson, I. Campbell and P. Fauchet, *Appl. Phys. Lett*. **53**, 2672 (1988).
23. J. Koh, H. Fujiwara, R. Koval, C. Wronski and R. Collins, *J. Appl. Phys*. **85**, 4141 (1999).
24. E. Eser, S. Hegedus and W. Buchanan, NCPV Review, *AIP Conf Proc*. **462** (1999), p. 254.
25. P. Sichanugrist, T. Sasaki, A. Asano, Y. Ichikawa and H. Sakai, *Sol. Energy Matl. and Sol. Cells* **34**, 415 (1994).
26. T. Okada, T. Iwaki, H. Kasahara and K. Yamamoto, *J. Vac. Sci.* Tech **A15**, 21 (1997).
27. C. R. Houska, *J. Appl. Phys*. **41** (1), 69 (1970).
28. G. Gilmer and H. H. Farrell, *J. Appl. Phys*. **47**, (10), 4378 (1976).
29. B.E. McCandless, L. V. Moulton and R. W. Birkmire, *Progress in Photovoltaics* **5**, 249 (1997).
30. R. A. Young and D. B. Wiles, *J. Appl. Cryst*. **15**, 430 (1982).
31. D. G. Jensen, B. E. McCandless and R. W. Birkmire, *Proc. MRS Symposium* **426** (1996), p. 325.
32. C. Barrett and T. B. Massalski, *Structure of Metals*, 3rd Edition, Pergamon Press, Oxford, (1980) p. 144.

33. K. Ohata, J. Saraie and T. Tanaka, *Jpn. J. Appl. Phys*. **12**, 1198 (1973).
34. S.- Y. Nunoue, T. Hemmi and E. Kato, *J. Electrochem. Soc. 137*, **4**, 1248 (1990).
35. D. Bonnet, *Phys. Stat. Sol. (a)* **3**, 913 (1970).
36. R. Hill and D. Richardson, *Thin Solid Films* **18**, 25 (1973).
37. K. Wei, F. Pollak, D. Shvydka and A. D. Compaan, *J. Appl. Phys. 85*, **10**, 7418 (1999).
38. D. G. Jensen, Doctoral Dissertation, Stanford University (1997).
39. Robert T. Dehoff, *Thermodynamics in Materials Science*, McGraw-Hill, Inc., (1993) p. 275.
40. W. A. Rachinger, *J. Sci. Inst*. **25**, 254 (1948).
41. D. G. Moon and H. B. Im, *Powder Metallurgy*, **35**(1), 53 (1992).
42. B. E. McCandless, H. Hichri, G. Hanket and R. W. Birkmire, *Proc 25th IEEE PVSC*. (1996), p. 781.
43. P. G. Shewmon, *Diffusion in Solids*, McGraw-Hill Book Co., New York (1963), p. 14.
44. J. H. Crawford and L. M. Slifkin (Eds), *Point Defects in Solids*, Plenum Press, New York, (1975), p. 227.
45. B. E. McCandless and S. S. Hegedus, *Proc. 22nd IEEE PVSC* (1991), p. 967.
46. B. E. McCandless and R. W. Birkmire, *Proc. NCPV Photovoltaics Program Review* (1999), p. 182.
47. D.G. Jensen, B.E. McCandless and R.W. Birkmire, *Proc. 25th IEEE PVSC* (1996), p. 773.
48. B. E. McCandless, I. Youm and R. W. Birkmire, *Progress in Photovoltaics* **7**, 21 (1999).
49. M. Al-Jassim, National CdTe R&D Team Meeting, Golden, CO, January 2000.
50. S.-H. Wei, S. B. Zhang and A. Zunger, *J. Appl. Phys.,* **87**(3), 1304 (2000).
51. R. A. Sasala, R.C. Powell, G.L. Dorer and N. Reiter*, AIP Conf. Proc.* **394** (1997), p. 171.
52. J. del Cueto, *Prog. In Photovoltaics* **6**, 433 (1999).
53. P.V. Meyers and J. Phillips, *25th IEEE PVSC* (1996), p. 789.
54. J.F. Hiltner and J.R. Sites, *AIP Conf. Proc*. **462** (1999), p. 170.
55. D. Morgan, J. Tang, V. Kaydanov, T. Ohno and J. Trefny, *AIP Conf. Proc.* **462** (1999), p. 200.
56. H. Rickert, H.-D. Wienhofer and R. Wagner, *Proc. 4th European PVSEC* (1982), p. 827.
57. K. Dobson, I. Visoly Fisher, G. Hodes and D. Cahen, *Sol. Energy Mat. Sol. Cells* **62**, 295 (2000).
58. R.W. Birkmire, B.E. McCandless and S.S. Hegedus, *Int. J. Solar Energy* **12**, 145 (1992).
59. IEC Annual Report to NREL, Phase I, Subcontract #ZAK-8-17619-33, August 1998-August 1999.
60. B. McCandless, Y. Qu and R. Birkmire, *Proc. 1st WCPEC* (1994), p. 107.
61. B. McCandless and J. Phillips, *2nd WCPEC*. (1998), p. 448.
62. D. Grecu and A. Compaan, *Appl. Phys. Lett.* **75**, 361 (1999).
63. H. H. Woodbury and M. Aven, *J. Appl. Physics* **39**(12), 5485 (1968).

REPORT DOCUMENTATION PAGE	Form Approved OMB NO. 0704-0188

Public reporting burden for this collection of information is estimated to average 1 hour per response, including the time for reviewing instructions, searching existing data sources, gathering and maintaining the data needed, and completing and reviewing the collection of information. Send comments regarding this burden estimate or any other aspect of this collection of information, including suggestions for reducing this burden, to Washington Headquarters Services, Directorate for Information Operations and Reports, 1215 Jefferson Davis Highway, Suite 1204, Arlington, VA 22202-4302, and to the Office of Management and Budget, Paperwork Reduction Project (0704-0188), Washington, DC 20503.

1. AGENCY USE ONLY (Leave blank)	2. REPORT DATE September 2001	3. REPORT TYPE AND DATES COVERED Annual Subcontract Report 24 August 1999 – 23 August 2000

4. TITLE AND SUBTITLE Optimization of Processing and Modeling Issues for Thin Film Solar Cell Devices Including Concepts for the Development of Polycrystalline Multijunctions Annual Subcontract Report, 24 August 1999 – 23 August 2000 6. AUTHOR(S) R.W. Birkmire, J.E. Phillips, W.N. Shafarman, E. Eser, S.S. Hegedus, B.E. McCandless	5. FUNDING NUMBERS CF: ZAK-8-17619-33 PVP15001
PERFORMING ORGANIZATION NAME(S) AND ADDRESS(ES) Institute of Energy Conversion University of Delaware Newark, Delaware 19716-3820	8. PERFORMING ORGANIZATION REPORT NUMBER
9. SPONSORING/MONITORING AGENCY NAME(S) AND ADDRESS(ES) National Renewable Energy Laboratory 1617 Cole Blvd. Golden, CO 80401-3393	10.SPONSORING/MONITORING AGENCY REPORT NUMBER NREL/SR-520-30922

11.SUPPLEMENTARY NOTES

NREL Technical Monitor: Bolko von Roedern

12a. DISTRIBUTION/AVAILABILITY STATEMENT National Technical Information Service U.S. Department of Commerce 5285 Port Royal Road Springfield, VA 22161	12b. DISTRIBUTION CODE

13.ABSTRACT *(Maximum 200 words)* This report describes the results achieved during Phase I of a three-phase subcontract to develop and understand thin-film solar cell technology associated with $CuInSe_2$ and related alloys, a-Si and its alloys, and CdTe. Modules based on all these thin films are promising candidates to meet DOE long-range efficiency, reliability, and manufacturing cost goals. The critical issues being addressed under this program are intended to provide the science and engineering basis for developing viable commercial processes and to improve module performance. The generic research issues addressed are: 1) quantitative analysis of processing steps to provide information for efficient commercial-scale equipment design and operation; 2) device characterization relating the device performance to materials properties and process conditions; 3) development of alloy materials with different bandgaps to allow improved device structures for stability and compatibility with module design; 4) development of improved window/heterojunction layers and contacts to improve device performance and reliability; and 5) evaluation of cell stability with respect to illumination, temperature, and ambient, and with respect to device structure and module encapsulation.

14.SUBJECT TERMS: PV ; thin film solar cell ; scale equipment design and operation ; effusion analysis ; X-ray diffraction ; sequential evaporation ; polycrystalline multijunctions ;	15.NUMBER OF PAGES
	16.PRICE CODE

17.SECURITY CLASSIFICATION OF REPORT	18.SECURITY CLASSIFICATION OF THIS PAGE	19.SECURITY CLASSIFICATION OF ABSTRACT	20.LIMITATION OF ABSTRACT
Unclassified	Unclassified	Unclassified	UL